Multifield Inflation: Predictivity and Initial Conditions

Layne C. Price

A thesis submitted in fulfilment of the
requirements for the degree of
Doctor of Philosophy in Physics,
The University of Auckland, 2015.

Abstract

With more than one light scalar field contributing to cosmological perturbations, multifield inflation models are distinguishable from scenarios with only one field. We address here two issues that affect multifield inflation models' ability to make predictions about the homogeneity of the universe and the statistics of the primordial spectrum of curvature perturbations.

We first consider the sensitivity of the prototypical hybrid inflation model to its initial conditions. We argue that physically comparable initial conditions must be constrained so that a bijective mapping can be made between allowed initial conditions and solutions to the equations of motion. Using this criterion, hybrid inflation retains characteristics of strong nonlinearity, such as chaotic dynamics, and that previous results for the robustness of the inflationary attractor can be applied to the system's solution space. We then extend this analysis to include primordial inhomogeneity by using numerical lattice PDE techniques. We find that the strong nonlinearity of hybrid inflation can result in a significantly different final state for inhomogeneous universes as compared to homogeneous initial conditions. A homogeneous universe that is unable to inflate sufficiently may instead become viable with a small amount of subhorizon inhomogeneity, in contrast to the conventional analysis for single-field inflation models.

We also consider how a multifield inflation model's predictions for the primordial power spectrum depend on its initial state, given that many multifield models have an infinite number of inflationary solutions. We develop an open-source Fortran program for Monte Carlo exploration of multifield inflation and

demonstrate numerically that N_f-quadratic inflation is not sensitively dependent on the prior probability chosen for the fields' initial conditions. Finally, we calculate a generic prediction for the inflationary consistency relation n_t/r at the end of inflation for a wide class of phenomenologically viable multifield inflation models. Although the models have significant complexity, the central limit theorem reduces the dimensionality of the probability distributions for observables, resulting in emergent simplicity for realistic multifield models.

Acknowledgments

I sincerely thank Richard Easther for his enthusiasm and honest critiques throughout my time in Auckland. I am especially grateful for his emphasis on the careful phrasing of research problems, so that the result is more likely to be rewarding and the process enjoyable. The freedom I had in setting my own research goals was made significantly less intimidating due to the open and energetic environment he fostered.

I owe a considerable debt to my co-authors, R. Easther, J. Frazer, H. Peiris, J. Rasero, and J. Xu. In particular, I thank Hiranya Peiris for hosting me in London and providing guidance during an extremely productive collaboration, as well as Jonny Frazer for countless enlightening discussions. I appreciate correspondence with S. Clesse, K. Malik, C. Ringeval, and J. White on the connection of this thesis to their work. Grigor Aslanyan has provided valuable criticism and has been an engaging and effective collaborator.

My work has been facilitated by the Royal Society International Exchanges Scheme and the University of Auckland Doctoral Scholarship. I acknowledge the use of the NeSI computing facilities and technical advice from the Centre for eResearch. This manuscript was proofread by R. Easther and G. Aslanyan, while the published papers were edited by their respective co-authors.

I would like to give a special thanks to the huge list of people who have adopted me as an "honorary mathematician" and my office mates Ricardo Gutierrez, Arne Grimsmo, and Simon Whalen for lasting friendships and endless fun over the past three years.

I will be forever grateful to my parents for encouraging higher education,

while repeatedly sacrificing to ensure I had every opportunity to succeed. Most importantly, my burden has been made immeasurably lighter and my life infinitely brighter by Terri and Ayla.

Use of Copyrighted Material

JCAP.— The following copyright information is pertinent for Chapters 2, 3, and 4 of this thesis, which were published in the Journal of Cosmology and Astroparticle Physics (JCAP).

> *3. Author Rights*
>
> *3.1 IOP and SISSA Medialab Srl grant the Named Authors the rights specified in 3.2 and 3.3. . . .*
>
> *3.2 The rights are: . . .*
>
> *3.2.2 To include the Article (all or part) in a research thesis or dissertation; . . .*
>
> *3.3 The additional rights are to:*
>
> *3.3.1 Use the Article (all or part) without modification in personal compilations or publications of a Named Author's own works (provided not created by third party publisher); . . .*
>
> *3.3.3 Include the Article (all or part) on web sites of the Institution (including its repository) where a Named Author worked when research for the Article was carried out;*

PRL.— The following copyright information is pertinent for Chapters 5 and 6 of this thesis, which were published in Physical Review Letters (PRL).

> *The author has the right to use the article or a portion of the article in a thesis or dissertation without requesting permission from APS, provided the bibliographic citation and the APS copyright credit line are given on the appropriate pages.*

Contents

THE UNIVERSITY OF AUCKLAND
SCHOOL OF GRADUATE STUDIES

Co-Authorship Form

ClockTower – East Wing
22 Princes Street, Auckland
Phone: +64 9 373 7599 ext 81321
Fax: +64 9 373 7610
Email: postgraduate@auckland.ac.nz
www.postgrad.auckland.ac.nz

This form is to accompany the submission of any PhD that contains research reported in published or unpublished co-authored work. **Please include one copy of this form for each co-authored work.** Completed forms should be included in all copies of your thesis submitted for examination and library deposit (including digital deposit), following your thesis Acknowledgements.

Please indicate the chapter/section/pages of this thesis that are extracted from a co-authored work and give the title and publication details or details of submission of the co-authored work. Thesis Chapter 2, published as: L. C. Price, J. Frazer, J. Xu, H. V. Peiris, and R. Easther, "MultiModeCode: An efficient numerical solver for multifield inflation", JCAP 03 (2015) 005	
Nature of contribution by PhD candidate	Lead author. Wrote majority of text, including an extensive first draft. Performed all calculations, made all figures. Wrote vast majority of final code product. Developed and executed initial idea for scientific results.
Extent of contribution by PhD candidate (%)	85%

CO-AUTHORS

Name	Nature of Contribution
Jonathan Frazer	Contributing author. Wrote bundle width section of text (not included in thesis). Contributed expertise to final code product.
Jiajun Xu	Contributing author. Minor contribution to text. Wrote small amount of final code product.
Hiranya Peiris	Contributing author. Minor contribution to text. Minor contribution to analysis of scientific results. Proposed initial need for this computer program in cosmology community.
Richard Easther	Contributing author. Minor contribution to text. Minor contribution to analysis of scientific results. Proposed initial need for this computer program in cosmology community.

Certification by Co-Authors

The undersigned hereby certify that:

- the above statement correctly reflects the nature and extent of the PhD candidate's contribution to this work, and the nature of the contribution of each of the co-authors; and
- in cases where the PhD candidate was the lead author of the work that the candidate wrote the text.

Name	Signature	Date
Jonathan Frazer	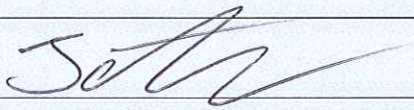	27/03/2015

THE UNIVERSITY OF AUCKLAND
SCHOOL OF GRADUATE STUDIES

Co-Authorship Form

This form is to accompany the submission of any PhD that contains research reported in published or unpublished co-authored work. **Please include one copy of this form for each co-authored work.** Completed forms should be included in all copies of your thesis submitted for examination and library deposit (including digital deposit), following your thesis Acknowledgements.

Please indicate the chapter/section/pages of this thesis that are extracted from a co-authored work and give the title and publication details or details of submission of the co-authored work. Thesis Chapter 2, published as: L. C. Price, J. Frazer, J. Xu, H. V. Peiris, and R. Easther, "MultiModeCode: An efficient numerical solver for multifield inflation", JCAP 03 (2015) 005	
Nature of contribution by PhD candidate	Lead author. Wrote majority of text, including an extensive first draft. Performed all calculations, made all figures. Wrote vast majority of final code product. Developed and executed initial idea for scientific results.
Extent of contribution by PhD candidate (%)	85%

CO-AUTHORS

Name	Nature of Contribution
Jonathan Frazer	Contributing author. Wrote bundle width section of text (not included in thesis). Contributed expertise to final code product.
Jiajun Xu	Contributing author. Minor contribution to text. Wrote small amount of final code product.
Hiranya Peiris	Contributing author. Minor contribution to text. Minor contribution to analysis of scientific results. Proposed initial need for this computer program in cosmology community.
Richard Easther	Contributing author. Minor contribution to text. Minor contribution to analysis of scientific results. Proposed initial need for this computer program in cosmology community.

Certification by Co-Authors

The undersigned hereby certify that:

- the above statement correctly reflects the nature and extent of the PhD candidate's contribution to this work, and the nature of the contribution of each of the co-authors; and
- in cases where the PhD candidate was the lead author of the work that the candidate wrote the text.

Name	Signature	Date
R EASTHER		14/5/15
Hiranya Peiris		25/03/2015

THE UNIVERSITY OF AUCKLAND
SCHOOL OF GRADUATE STUDIES

Co-Authorship Form

This form is to accompany the submission of any PhD that contains research reported in published or unpublished co-authored work. **Please include one copy of this form for each co-authored work.** Completed forms should be included in all copies of your thesis submitted for examination and library deposit (including digital deposit), following your thesis Acknowledgements.

Please indicate the chapter/section/pages of this thesis that are extracted from a co-authored work and give the title and publication details or details of submission of the co-authored work. Thesis Chapter 2, published as: L. C. Price, J. Frazer, J. Xu, H. V. Peiris, and R. Easther, "MultiModeCode: An efficient numerical solver for multifield inflation", JCAP 03 (2015) 005	
Nature of contribution by PhD candidate	Lead author. Wrote majority of text, including an extensive first draft. Performed all calculations, made all figures. Wrote vast majority of final code product. Developed and executed initial idea for scientific results.
Extent of contribution by PhD candidate (%)	85%

CO-AUTHORS

Name	Nature of Contribution
Jonathan Frazer	Contributing author. Wrote bundle width section of text (not included in thesis). Contributed expertise to final code product.
Jiajun Xu	Contributing author. Minor contribution to text. Wrote small amount of final code product.
Hiranya Peiris	Contributing author. Minor contribution to text. Minor contribution to analysis of scientific results. Proposed initial need for this computer program in cosmology community.
Richard Easther	Contributing author. Minor contribution to text. Minor contribution to analysis of scientific results. Proposed initial need for this computer program in cosmology community.

Certification by Co-Authors

The undersigned hereby certify that:

- the above statement correctly reflects the nature and extent of the PhD candidate's contribution to this work, and the nature of the contribution of each of the co-authors; and
- in cases where the PhD candidate was the lead author of the work that the candidate wrote the text.

Name	Signature	Date
JIAJUN XU	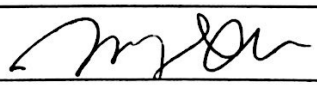	4/17/2015

Last updated: 25 March 2013

THE UNIVERSITY OF AUCKLAND
SCHOOL OF GRADUATE STUDIES

Co-Authorship Form

This form is to accompany the submission of any PhD that contains research reported in published or unpublished co-authored work. **Please include one copy of this form for each co-authored work.** Completed forms should be included in all copies of your thesis submitted for examination and library deposit (including digital deposit), following your thesis Acknowledgements.

Please indicate the chapter/section/pages of this thesis that are extracted from a co-authored work and give the title and publication details or details of submission of the co-authored work. Thesis Chapter 3, published as: R. Easther and L. C. Price, Initial conditions and sampling for multifield inflation, JCAP 1307 (2013) 027	
Nature of contribution by PhD candidate	Lead author. Wrote majority of text, including an extensive first draft. Performed all calculations, made all figures, analyzed all data. Wrote computer analysis programs. Contributed significantly to idea development.
Extent of contribution by PhD candidate (%)	85%

CO-AUTHORS

Name	Nature of Contribution
Richard Easther	Contributing author. Developed initial idea. Minor contribution to the text.

Certification by Co-Authors

The undersigned hereby certify that:

- the above statement correctly reflects the nature and extent of the PhD candidate's contribution to this work, and the nature of the contribution of each of the co-authors; and
- in cases where the PhD candidate was the lead author of the work that the candidate wrote the text.

Name	Signature	Date
R EASTHER		14/5/15

THE UNIVERSITY OF AUCKLAND
SCHOOL OF GRADUATE STUDIES

Co-Authorship Form

This form is to accompany the submission of any PhD that contains research reported in published or unpublished co-authored work. **Please include one copy of this form for each co-authored work.** Completed forms should be included in all copies of your thesis submitted for examination and library deposit (including digital deposit), following your thesis Acknowledgements.

Please indicate the chapter/section/pages of this thesis that are extracted from a co-authored work and give the title and publication details or details of submission of the co-authored work. Thesis Chapter 4, published as: R. Easther, L. C. Price, and J. Rasero, Inflating an Inhomogeneous Universe, JCAP 1408 (2014) 041	
Nature of contribution by PhD candidate	Lead author. Wrote majority of text, including an extensive first draft. Performed all calculations, made all figures, analyzed all data.
Extent of contribution by PhD candidate (%)	80%

CO-AUTHORS

Name	Nature of Contribution
Richard Easther	Contributing author. Minor contribution to text. Proposed using lattice PDE solvers for this type of problem.
Javier Rasero	Contributing author. Adapted subroutines in pre-existing code (LatticeEasy) to apply to this problem.

Certification by Co-Authors

The undersigned hereby certify that:

- the above statement correctly reflects the nature and extent of the PhD candidate's contribution to this work, and the nature of the contribution of each of the co-authors; and
- in cases where the PhD candidate was the lead author of the work that the candidate wrote the text.

Name	Signature	Date
R EASTHER.	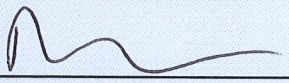	14/5/14

THE UNIVERSITY OF AUCKLAND
SCHOOL OF GRADUATE STUDIES

Co-Authorship Form

Graduate Centre
ClockTower – East Wing
22 Princes Street, Auckland
Phone: +64 9 373 7599 ext 81321
Fax: +64 9 373 7610
Email: postgraduate@auckland.ac.nz
www.postgrad.auckland.ac.nz

This form is to accompany the submission of any PhD that contains research reported in published or unpublished co-authored work. **Please include one copy of this form for each co-authored work**. Completed forms should be included in all copies of your thesis submitted for examination and library deposit (including digital deposit), following your thesis Acknowledgements.

Please indicate the chapter/section/pages of this thesis that are extracted from a co-authored work and give the title and publication details or details of submission of the co-authored work. Thesis Chapter 4, published as: R. Easther, L. C. Price, and J. Rasero, Inflating an Inhomogeneous Universe, JCAP 1408 (2014) 041	
Nature of contribution by PhD candidate	Lead author. Wrote majority of text, including an extensive first draft. Performed all calculations, made all figures, analyzed all data.
Extent of contribution by PhD candidate (%)	80%

CO-AUTHORS

Name	Nature of Contribution
Richard Easther	Contributing author. Minor contribution to text. Proposed using lattice PDE solvers for this type of problem.
Javier Rasero	Contributing author. Adapted subroutines in pre-existing code (LatticeEasy) to apply to this problem.

Certification by Co-Authors

The undersigned hereby certify that:

- the above statement correctly reflects the nature and extent of the PhD candidate's contribution to this work, and the nature of the contribution of each of the co-authors; and
- in cases where the PhD candidate was the lead author of the work that the candidate wrote the text.

Name	Signature	Date
Javier Rasero	Javier Rasero	2015/3/17

THE UNIVERSITY OF AUCKLAND
SCHOOL OF GRADUATE STUDIES

Co-Authorship Form

This form is to accompany the submission of any PhD that contains research reported in published or unpublished co-authored work. **Please include one copy of this form for each co-authored work.** Completed forms should be included in all copies of your thesis submitted for examination and library deposit (including digital deposit), following your thesis Acknowledgements.

Please indicate the chapter/section/pages of this thesis that are extracted from a co-authored work and give the title and publication details or details of submission of the co-authored work. Thesis Chapter 5, published as: R. Easther, J. Frazer, H. V. Peiris, and L. C. Price, Simple predictions from multifield inflationary models, Phys.Rev.Lett. 112 (2014) 161302	
Nature of contribution by PhD candidate	Lead author. Wrote majority of text, including an extensive first draft. Performed all calculations, made all figures, analyzed all data. Wrote MultiModeCode, the computer program used for analysis. Developed initial project idea in conjunction with J. Frazer.
Extent of contribution by PhD candidate (%)	65%

CO-AUTHORS

Name	Nature of Contribution
Richard Easther	Contributing author. Minor contribution to text. Proposed initial need for MultiModeCode program.
Jonathan Frazer	Contributing author. Minor contribution to text. Developed initial project idea in conjunction with L. Price. Contributed to analysis of results.
Hiranya Peiris	Contributing author. Minor contribution to text. Proposed initial need for MultiModeCode program.

Certification by Co-Authors

The undersigned hereby certify that:

- the above statement correctly reflects the nature and extent of the PhD candidate's contribution to this work, and the nature of the contribution of each of the co-authors; and
- in cases where the PhD candidate was the lead author of the work that the candidate wrote the text.

Name	Signature	Date
Hiranya Peiris		25/03/2015
R EASTHER		14/3/15

THE UNIVERSITY OF AUCKLAND
SCHOOL OF GRADUATE STUDIES

Co-Authorship Form

ClockTower – East Wing
22 Princes Street, Auckland
Phone: +64 9 373 7599 ext 81321
Fax: +64 9 373 7610
Email: postgraduate@auckland.ac.nz
www.postgrad.auckland.ac.nz

This form is to accompany the submission of any PhD that contains research reported in published or unpublished co-authored work. **Please include one copy of this form for each co-authored work.** Completed forms should be included in all copies of your thesis submitted for examination and library deposit (including digital deposit), following your thesis Acknowledgements.

Please indicate the chapter/section/pages of this thesis that are extracted from a co-authored work and give the title and publication details or details of submission of the co-authored work. Thesis Chapter 5, published as: R. Easther, J. Frazer, H. V. Peiris, and L. C. Price, Simple predictions from multifield inflationary models, Phys.Rev.Lett. 112 (2014) 161302	
Nature of contribution by PhD candidate	Lead author. Wrote majority of text, including an extensive first draft. Performed all calculations, made all figures, analyzed all data. Wrote MultiModeCode, the computer program used for analysis. Developed initial project idea in conjunction with J. Frazer.
Extent of contribution by PhD candidate (%)	65%

CO-AUTHORS

Name	Nature of Contribution
Richard Easther	Contributing author. Minor contribution to text. Proposed initial need for MultiModeCode program.
Jonathan Frazer	Contributing author. Minor contribution to text. Developed initial project idea in conjunction with L. Price. Contributed to analysis of results.
Hiranya Peiris	Contributing author. Minor contribution to text. Proposed initial need for MultiModeCode program.

Certification by Co-Authors

The undersigned hereby certify that:

- the above statement correctly reflects the nature and extent of the PhD candidate's contribution to this work, and the nature of the contribution of each of the co-authors; and
- in cases where the PhD candidate was the lead author of the work that the candidate wrote the text.

Name	Signature	Date
Jonathan Frazer	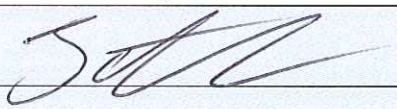	27/03/2015

THE UNIVERSITY OF AUCKLAND
SCHOOL OF GRADUATE STUDIES

Co-Authorship Form

This form is to accompany the submission of any PhD that contains research reported in published or unpublished co-authored work. **Please include one copy of this form for each co-authored work.** Completed forms should be included in all copies of your thesis submitted for examination and library deposit (including digital deposit), following your thesis Acknowledgements.

Please indicate the chapter/section/pages of this thesis that are extracted from a co-authored work and give the title and publication details or details of submission of the co-authored work. Thesis Chapter 6, published as: L. C. Price, H. V. Peiris, J. Frazer, and R. Easther, Gravitational wave consistency relations for multifield inflation, Phys.Rev.Lett. 114 (2014) 031301	
Nature of contribution by PhD candidate	Lead author. Wrote majority of text, including an extensive first draft. Performed all calculations, made all figures. Developed initial idea.
Extent of contribution by PhD candidate (%)	85%

CO-AUTHORS

Name	Nature of Contribution
Hiranya Peiris	Contributing author. Minor contribution to text. Proposed working on this topic. Contributed to interpretation of scientific results.
Jonathan Frazer	Contributing author. Minor contribution to text.
Richard Easther	Contributing author. Minor contribution to text.

Certification by Co-Authors

The undersigned hereby certify that:

- the above statement correctly reflects the nature and extent of the PhD candidate's contribution to this work, and the nature of the contribution of each of the co-authors; and
- in cases where the PhD candidate was the lead author of the work that the candidate wrote the text.

Name	Signature	Date
Hiranya Peiris	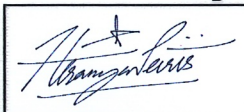	25/03/2015
R EASTHER	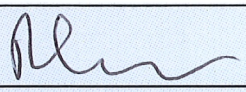	14/5/2015.

THE UNIVERSITY OF AUCKLAND
SCHOOL OF GRADUATE STUDIES

Co-Authorship Form

ClockTower – East Wing
22 Princes Street, Auckland
Phone: +64 9 373 7599 ext 81321
Fax: +64 9 373 7610
Email: postgraduate@auckland.ac.nz
www.postgrad.auckland.ac.nz

This form is to accompany the submission of any PhD that contains research reported in published or unpublished co-authored work. **Please include one copy of this form for each co-authored work.** Completed forms should be included in all copies of your thesis submitted for examination and library deposit (including digital deposit), following your thesis Acknowledgements.

Please indicate the chapter/section/pages of this thesis that are extracted from a co-authored work and give the title and publication details or details of submission of the co-authored work. Thesis Chapter 6, published as: L. C. Price, H. V. Peiris, J. Frazer, and R. Easther, Gravitational wave consistency relations for multifield inflation, Phys.Rev.Lett. 114 (2014) 031301	
Nature of contribution by PhD candidate	Lead author. Wrote majority of text, including an extensive first draft. Performed all calculations, made all figures. Developed initial idea.
Extent of contribution by PhD candidate (%)	85%

CO-AUTHORS

Name	Nature of Contribution
Hiranya Peiris	Contributing author. Minor contribution to text. Proposed working on this topic. Contributed to interpretation of scientific results.
Jonathan Frazer	Contributing author. Minor contribution to text.
Richard Easther	Contributing author. Minor contribution to text.

Certification by Co-Authors

The undersigned hereby certify that:

- the above statement correctly reflects the nature and extent of the PhD candidate's contribution to this work, and the nature of the contribution of each of the co-authors; and
- in cases where the PhD candidate was the lead author of the work that the candidate wrote the text.

Name	Signature	Date
Jonathan Frazer		27/03/2015

PART I

An Overview of Inflation

Chapter 1

Beyond the Simplest Picture

1.1 Introduction

The amount of data available to cosmologists has undergone a radical expansion in the early portion of the 21$^{\text{st}}$ century, ushering us into the era of "Precision Cosmology." The recent improvement in the observations of the cosmic microwave background (CMB) with the WMAP and *Planck* space-based telescopes has drastically increased our ability to test for a primordial epoch of inflation. Inflation is an early period of accelerated expansion of the universe, which is invoked at the level of the classical background to create a flat and approximately homogeneous universe. This basic picture was put forward in a series of papers in the 1980s [1–4], which revolutionized our ideas of the early universe. Importantly, inflation also generates random, classical perturbations on an otherwise smooth and flat universe with a characteristic spectrum that depends, typically, on the functional form of the potential energy density for a scalar field. The statistics of these perturbations are distinguishable in the present-day signal from the CMB and large-scale structure, allowing us to constrain the model space of inflation.

In particular, with the WMAP9 dataset [5] the standard ΛCDM cosmology acquired the parameter n_s, which measures the deviation of the primordial power spectrum from the featureless Harrison-Zel'dovich spectrum, at greater than 5σ significance. A non-unity n_s is one of the strongest predictions for

inflation, although the exact value can differ depending on the specifics of the inflationary model and other early universe scenarios may also yield $n_s \neq 1$.

In this chapter we will discuss the role that the basic inflationary mechanism plays in the standard picture of cosmology. We will introduce the semi-classical picture of inflationary perturbations, the power spectrum, and the main subject of this thesis, multifield models of inflation, and how their predictions may differ from the simple single-field models. Finally, we will discuss the role of Bayesian statistics in understanding and reporting theoretical uncertainty in models.

1.2 The need for inflation

The simple picture.— There are some major problems for the initial conditions of the classical universe. Since curvature and inhomogeneities grow on sub-horizon scales, the observed flatness and approximate homogeneity of the modern universe on super-horizon scales would otherwise require an exceptional initial state that must have been many orders of magnitude flatter and more homogeneous than today. An especially important problem for this thesis is that the CMB is isotropic to first-order for regions of the sky that were never in causal contact, the so-called *horizon* or *homogeneity problem*.

An early period of accelerated expansion provides a physical mechanism to solve these problems by shrinking the size of the Hubble radius in comoving coordinates during a phase of accelerated expansion, which has the scale factor a evolving like $\ddot{a} > 0$, with overdots indicating derivatives with respect to cosmic time t. In physical coordinates, the Hubble radius is H^{-1}, which gives a comoving Hubble radius $r_{\rm cmv} = (aH)^{-1}$ that shrinks as

$$\frac{d}{dt}\left[\frac{1}{a\,H}\right] = -\frac{\ddot{a}}{(\dot{a})^2} < 0. \tag{1.1}$$

Any gradients in the matter fields with comoving length R are then expanded outside of the Hubble horizon during inflation, yielding an arbitrarily homogeneous universe locally. This makes the physically-relevant neighborhood around a given point in space-time decrease with time, so that the entire present-day universe could have existed inside a causally connected region prior to inflation; the typical size for homogeneous patches today would then exceed the distance to the surface of last scattering.

The problem of initial conditions.– However, even at the level of the classical background, this simple picture is not entirely adequate. Importantly, one of the main assumptions hidden above is that inflation must start on a super-H comoving region of the universe, despite there being no causal reason for this [6, 7]. Consequently, the horizon problem is only solved by this mechanism if the initial conditions of the Universe satisfied the necessary conditions for inflation in adjacent, but causally disconnected regions. We will address this problem in Chapter 4.

1.3 Cosmological perturbation theory

The most important aspect of cosmological inflation is that classical curvature perturbations larger than the comoving horizon are generated in a nearly scale-invariant and stochastic fashion from quantum perturbations on sub-horizon scales. The statistics of the classical perturbations have now been constrained to a fine degree from CMB data. This enables us to put serious pressure on some of the simplest inflationary models, significantly restricting the allowed parameter space and changing our opinion on the types of models that yield observationally viable universes. In this section we will discuss how quantum perturbations lead to classical perturbations and how we calculate the statistics

of the primordial perturbations.

1.3.1 Perturbed FLRW

To describe the basic mechanism we will start with a perturbed Friedmann-Lemaître-Robertson-Walker (FLRW) metric:

$$g_{\mu\nu} = \bar{g}_{\mu\nu} + h_{\mu\nu}, \tag{1.2}$$

where

$$\bar{g}_{\mu\nu}(\tau) = a(\tau)\,\eta_{\mu\nu} \tag{1.3}$$

for scale factor a, when the time variable is conformal time $d\tau \equiv dt/a$, and $\eta_{\mu\nu}$ is the Minkowski metric with signature $(-,+,+,+)$. Throughout this thesis we will use the convention where Greek indices run from $\mu = 0,\ldots,3$ and Latin indices from $i = 1,2,3$. The perturbations are defined as

$$h_{00} = -2a^2\Psi \tag{1.4}$$

$$h_{0i} = 2a^2 B_i \tag{1.5}$$

$$h_{ij} = a^2\left[(1-2\Phi) + 2E_{ij}\right], \tag{1.6}$$

where Ψ and Φ are scalars, but not Lorentz scalars; B_i is a 3-vector, *i.e.*, is invariant under spatial rotations; and E_{ij} is a symmetric and trace-free ($E^i_{\ i} \equiv 0$) 3-tensor. All of the functions in Eqs (1.4)–(1.6) depend on x^μ and the number of independent components of $h_{\mu\nu}$ are matched by the number of degrees of freedom in Ψ, Φ, B_i, and E_{ij}.

Using the results of Ref. [8] we uniquely decompose B_i and E_{ij} into scalar, vector, and tensor components:

$$B_i \equiv \partial_i B + \hat{B}_i \tag{1.7}$$

and

$$E_{ij} \equiv \partial_{\langle i}\partial_{j\rangle}E + \partial_{(i}\hat{E}_{j)} + \hat{E}_{ij}, \tag{1.8}$$

where the hat indicates that the object is transverse, symmetric, and trace-free. The round and angled brackets in Eq. (1.8) imply symmetrization and anti-symmetrization, respectively, so that

$$\partial_{\langle i}\partial_{j\rangle}E = \partial_i\partial_j E - \frac{1}{3}\nabla^2 E. \tag{1.9}$$

At linear order in $h_{\mu\nu}$, the perturbative Einstein equations for the scalar, vector, and tensor components above are decoupled, making this a valuable decomposition for the metric perturbations.

1.3.2 Gauge invariance & diffeomorphism

General Relativity describes physics through the definition of a manifold M with an associated set of fields, such as the metric g, a scalar ϕ, or the Maxwell tensor F. If manifold N is diffeomorphic to M with $\varphi : M \to N$, then M and N have identical manifold structures, *i.e.*, the manifold M is associated with objects such as the metric g and connection ∇ that are mapped to structures in N that have identical properties. To make General Relativity a sensible model, it is therefore obvious that we must identify diffeomorphic manifolds as being physically equivalent.

If we have a diffeomorphism $\varphi : M \to N$, then tensors on M are mapped bijectively to tensors on N through the function φ_*, which is called the *push-forward*, and from N to M via the *pull-back* φ^*, which is the inverse of the push-forward.[1] The components of the transformed tensors are given in the

[1] Note that the push-forward and pull-back can be defined independently of the existence of any diffeomorphism, but are inverses of each other for this special case.

usual fashion for change-of-basis with a tensor T changing as

$$T^{\mu}{}_{\nu} \to (\phi_* \circ T)^{\mu}{}_{\nu} = \frac{\partial y^{\mu}}{\partial x^{\rho}} \frac{\partial x^{\sigma}}{\partial y^{\nu}} T^{\rho}{}_{\sigma}, \tag{1.10}$$

where the coordinate bases x^{μ} and y^{ρ} on M and N, respectively, are related by the diffeomorphism. This can be expressed in a coordinate basis as

$$x^{\mu} \xrightarrow{\varphi_*} y^{\mu} = x^{\mu} + \xi^{\mu}(x^{\nu}) \tag{1.11}$$

for a vector field ξ^{μ}.

The Einstein-Hilbert action

$$S_{\mathrm{EH}} = \frac{1}{16\pi G} \int d^4x \sqrt{-g}\, \mathscr{R}, \tag{1.12}$$

where $\mathscr{R}$ is the Ricci scalar, is manifestly invariant with respect to the push-forward of the metric, since $\mathscr{R}$ is a curvature invariant. In the rest of this thesis we will use units where $M_{\mathrm{Pl}}^{-2} \equiv 8\pi G \equiv 1$. The contracted Bianchi identity

$$\nabla^{\mu} T_{\mu\nu} = 0, \tag{1.13}$$

where $T_{\mu\nu}$ is the energy-momentum tensor, ensures that this is also true for the action for the matter sector, yielding equivalent equations of motion on manifolds M and N.[2] For each diffeomorphism, obtained through the definition of ξ^{μ}, we then have a set of identical physical situations. This diffeomorphism, or gauge, invariance implies that four degrees of freedom in the system are redundant and can be removed by fixing a gauge, *i.e.*, uniquely choosing ξ^{μ}.

To understand the role that gauge freedom plays in cosmological perturbation theory, we will follow Ref. [9] and identify the relationship in Eq. (1.2) as resulting from a diffeomorphism φ that takes points in the neighborhood

[2] By not treating M and N as the same manifold, we are using the "active" view of diffeomorphisms. If we instead interpret the right-hand side of Eq. (1.11) as defining another coordinate system y^{μ} on M, then this is the equivalent "passive" interpretation.

of a point p in a manifold M_{phys} and maps them to another manifold M_{ptb} as $p \xrightarrow{\varphi} p'$, with a resulting change in the metric and stress-energy tensors as

$$g_{\mu\nu} \xrightarrow{\varphi_*} \bar{g}_{\mu\nu} + h_{\mu\nu} \tag{1.14}$$

and

$$T_{\mu\nu} \xrightarrow{\varphi_*} \bar{T}_{\mu\nu} + t_{\mu\nu}. \tag{1.15}$$

In the above equations, the barred quantities are arbitrary reference tensors and $h_{\mu\nu}$ and $t_{\mu\nu}$ are not yet required to be small. Since the pull-back is the inverse of the push-forward, we can see that

$$h_{\mu\nu} = (\varphi_* \circ g)_{\mu\nu} - \bar{g}_{\mu\nu}. \tag{1.16}$$

and similarly for $t_{\mu\nu}$. Consequently, $h_{\mu\nu}$ is small in the neighborhood of $p' \in M_{\text{ptb}}$ for the family of diffeomorphisms φ that satisfy $(\varphi_* \circ g)_{\mu\nu} \approx \bar{g}_{\mu\nu}$ for a given background metric $\bar{g}_{\mu\nu}$ and stress-energy tensor $T_{\mu\nu}$ that $g_{\mu\nu}$ and $T_{\mu\nu}$ are locally diffeomorphic to, respectively.

However, the freedom to choose both $h_{\mu\nu}$ to be small and the target metric $\bar{g}_{\mu\nu}$ independently will apply only locally near $p' \in M_{\text{ptb}}$; points close to $p \in M_{\text{phys}}$ may have an arbitrarily large deviation from the desired behavior. For instance, the diffeomorphism φ could induce a local normal coordinate chart near $p' \in M_{\text{ptb}}$ where $\bar{g}_{\mu\nu}$ is the Minkowski metric and $h_{\mu\nu} = 0$, without loss of generality. However, this will not generally induce a local normal coordinate chart for points near p.

Consequently, to make this an effective scheme in which to do computations we would ideally like a description of the spacetime where $h_{\mu\nu}$ is small and $\bar{g}_{\mu\nu}$ does not sensitively depend on the point p in the physical manifold M_{phys}. In other words, we would like Eq. (1.16) to apply over a large region around $p \in M_{\text{phys}}$, so that we only have to solve this system of equations once for all

regions in $M_{\rm phys}$ of interest to us. To apply this to cosmology we therefore need a description of what the universe looks like away from our local point in space-time, which is given to us by the Copernican principle, resulting in the FLRW metric above.

1.3.3 Gauge fixing & perturbations

Given an expansion for the metric and matter fields like Eqs (1.14) and (1.15), there is a family of diffeomorphisms, which have a form as in Eq. (1.11), that satisfy $h_{\mu\nu} \ll 1$ even for a well-motivated choice of target metric $\bar{g}_{\mu\nu}$, such as the homogeneous FLRW metric. For example, if $h_{\mu\nu}$ is small in one coordinate chart x^μ on $M_{\rm ptb}$, then the mapping $x^\mu \to y^\mu = x^\mu + \epsilon\xi^\mu$, for an arbitrary vector field ξ^μ, will also have small metric perturbations if $\epsilon \ll 1$.

Consequently, we need to choose one of these diffeomorphisms, fixing the four degrees of freedom available by the choice of ξ^μ in Eq. (1.11) to yield a completely well-determined physical system in which to do our calculations. This process is called gauge fixing and defines the coordinate system on the perturbative manifold $M_{\rm ptb}$, which we interpret as a threading of spacetime into time-like wordlines and space-like hypersurfaces that have properties that will simplify the analysis.[3]

Using the scalar-vector-tensor decomposition above, we can split the vector field that defines our diffeomorphism into

$$\xi^\mu = \left(\xi^0, \partial^i\xi + \hat{\xi}^i\right). \tag{1.17}$$

This results in a relationship between metric perturbations in different gauges, which can be found explicitly in Ref. [8]. Importantly, the definition above

[3]However, starting with a given slicing/threading does not yield enough information to uniquely determine the coordinate chart on $M_{\rm ptb}$. See the discussion in Ref. [10].

splits the gauge transformations' dependence on ξ^μ so that each scalar component in Eqs (1.4)–(1.5) is related to its corresponding perturbation in the new gauge by only the two functions ξ^0 and ξ, while the vector components are functions of also $\hat{\xi}^i$. The tensor components to the metric perturbations are manifestly gauge invariant. We can therefore choose $(\xi^0, \partial^i\xi)$ in such a way to remove two scalar degrees of freedom from the metric and $\hat{\xi}^i$ to remove two vector degrees of freedom. We will often choose the flat gauge with

$$\Phi = E = 0, \tag{1.18}$$

where constant-time hypersurfaces are spatially flat.

1.4 Single-field inflation

The simplest way that we can get inflation is through the action

$$S_\phi = \int d^4x\sqrt{-g}\left[-\frac{1}{2}\partial_\mu\phi\partial_\mu\phi - V(\phi)\right], \tag{1.19}$$

where ϕ is a Lorentz scalar with potential energy density V and a canonical form for its kinetic energy. The equation of motion for ϕ from Eq. (1.19) is the Klein-Gordon equation

$$\frac{1}{\sqrt{-g}}\partial_\mu\left(\sqrt{-g}\,\partial^\mu\phi\right) - \frac{dV}{d\phi} = 0, \tag{1.20}$$

where the determinant of the FLRW metric is $g = -a^6$ in three dimensions. The $0-0$ portion of the Einstein equation, for the homogeneous background with a and ϕ independent of the spatial location, yields

$$H^2 = \frac{1}{3}\left(\frac{1}{2}\dot{\phi}^2 + V(\phi)\right), \tag{1.21}$$

where $H \equiv \dot{a}/a$ is the Hubble parameter and overdots are derivatives with respect to cosmic time t. This can be substituted into Eq. (1.20) to get

$$\ddot{\phi} + 3H\dot{\phi} + \frac{dV}{d\phi} = 0 \tag{1.22}$$

for a homogeneous scalar field.

Inflation is realized by a configuration that is dominated by V, which is approximately constant and smooth, so that the field ϕ has almost no change in its velocity. In this limit, the Hubble parameter is dominated by V, so that

$$H^2 \approx \frac{1}{3}V(\phi) \tag{1.23}$$

and the Klein-Gordon equation then becomes

$$\dot{\phi} \approx \frac{1}{\sqrt{3V}}\frac{dV}{d\phi}, \tag{1.24}$$

which is the *slow-roll approximation.*

1.4.1 Inhomogeneities from inflation

Importantly, inflation will also generate a perturbed, classical universe from quantum perturbations. In this section we will study this in the simplest case, which is an approximately massless scalar field, and leave the detailed exposition of the general equations for a collection of canonical scalar fields to Chapter 2.

In flat gauge, we will consider a matter sector consisting of only one scalar field that is approximately homogeneous with an inhomogeneous perturbation of the form

$$\phi(t, x^i) = \bar{\phi}(t) + \delta\phi(t, x^i). \tag{1.25}$$

The action S for the inflationary system is then the combination of the Einstein-Hilbert graviational sector (1.12) for the perturbed FLRW metric in Eqs (1.3)–(1.6) and the scalar action (1.19):

$$S = \int d^4x\sqrt{-g}\left[\frac{1}{2}\mathscr{R} - \frac{1}{2}\partial_\mu\phi\partial^\mu\phi - V\right]. \tag{1.26}$$

We then obtain the equation of motion for $\delta\phi(t, x^i)$ by expanding S to second-order in the scalar field perturbation and first-order in the metric perturbations. Changing variables to $u = a\delta\phi$ simplifies the equation of motion and we will perform our analysis with this variable. If we Fourier-transform $u(t, x^i) \to u_k(t)$, then we obtain the Mukhanov-Sasaki equation

$$u_k'' + \left(k^2 - \frac{z''}{z}\right) u_k = 0, \tag{1.27}$$

where a prime indicates a derivative with respect to conformal time $\tau \equiv \int dt/a$. We have defined the background quantities $\mathcal{H} \equiv a'/a$, which is the conformal Hubble parameter, and $z \equiv a\phi'/\mathcal{H}$. If the background is inflating, then modes with a comoving length scale of k^{-1} will expand beyond the comoving Hubble horizon.

1.4.2 Quantization

We will treat the background as if it were evolving purely classically, but require the perturbations $\delta\phi$ to be quantum fields. In general, to get the three-point and higher correlators for the theory we will need to perform calculations in the semi-classical interacting picture. However, we will not need to calculate these higher correlators from first-principles for the remainder of this thesis, so we are free to use the Heisenberg picture.

We will quantize by first defining raising and lowering operators $\hat{a}_k^\dagger$ and $\hat{a}_k$, respectively, by promoting u_k and its conjugate momentum $\pi_k \equiv u_k'$ to quantum operators, where we define

$$\hat{u}_k \equiv u_k \hat{a}_k + u_k^* \hat{a}_{-k}^\dagger \tag{1.28}$$

and similarly for its conjugate momentum and Hermitian conjugate. We then impose canonical commutation relations for

$$\left[\hat{a}_k, \hat{a}_q^\dagger\right] = \delta(\mathbf{k} - \mathbf{q}), \tag{1.29}$$

with all other combinations of $\hat{a}_k$ and $\hat{a}_q^\dagger$ commuting. We can relate this commutation relation to that of $\hat{u}_k$ and $\hat{\pi}_q$ as

$$\begin{aligned} [\hat{u}_k, \hat{\pi}_q] &= u_k u_q'^* \left[\hat{a}_k, \hat{a}_{-q}^\dagger\right] - u_k^* u_q' \left[\hat{a}_q, \hat{a}_{-k}^\dagger\right] && (1.30) \\ &= \left(u_k u_k'^* - u_k^* u_k'\right) \delta(\mathbf{k}+\mathbf{q}), && (1.31) \end{aligned}$$

where the second inequality assumes that the modes u_k depend only on $k = |\mathbf{k}|$. Importantly, we are not in general able to simultaneously enforce Eqs (1.29) and have non-vanishing commutation relations for Eq. (1.31) in a time-dependent background. Therefore, the conjugate variables $\hat{u}_k$ and $\hat{\pi}_k$ may either act like classical fields that commute or as quantum fields that do not.

Since an FLRW universe is locally diffeomorphic to Minkowski space, we will look for solutions to Eq. (1.27) that yield the canonical commutation relations $[\hat{u}_k, \hat{\pi}_q] = i\delta(\mathbf{k}+\mathbf{q})$ on sub-horizon scales with $k \gg aH$. These modes will have an equation of motion approximately equal to that of a massless scalar field in the absence of gravity,

$$u_k'' + k^2 u_k \approx 0. \tag{1.32}$$

The solutions to this are plane waves, which give the Minkowski-space commutation relations when

$$u_k = \frac{1}{\sqrt{2k}} e^{-ik\tau}, \tag{1.33}$$

up to an arbitrary choice of initial phase. It is standard to take this solution to be the initial conditions for u_k, since this is also an attracting solution for substantially sub-horizon modes with $k \gg aH$, although this initial condition can certainly be altered.

We contrast this with super-horizon modes with $k \ll aH$ that satisfy

$$\frac{u_k''}{u_k} \approx \frac{a''}{a} \tag{1.34}$$

for background solutions that obey the slow-roll equations of motion (1.24). From Eq. (1.34) $u_k \sim a$ and, since $u_k = a\delta\phi_k$, the field perturbations are constant on super-horizon scales. Similarly, if we transform to a gauge where constant time hypersurfaces have uniform density, we can directly relate the field perturbations in flat gauge to curvature perturbations ζ in uniform-density gauge; these curvature perturbations are also constant. It can be shown that the super-horizon conservation of ζ is a consequence of adiabatic evolution and is not exclusive to single-field inflation [11, 12].

Since u_k is a real function on super-horizon scales, from Eq. (1.31) we can see that $\hat{u}_k$ and $\hat{\pi}_k$ commute and modes of the quantum field that have exited the horizon act as if they were purely classical. This is the "pragmatic view" of the quantum-to-classical transition for inflationary perturbations, which can be made more precise in terms of decoherence [13].

We can define the quasi–de Sitter vacuum state as $a_k |0\rangle \equiv 0$, which gives the tree-level two-point vacuum expectation value

$$\langle 0| \hat{u}_k \hat{u}_q^\dagger |0\rangle \quad = \quad |u_k|^2 \delta(\mathbf{k} - \mathbf{q}). \tag{1.35}$$

Since a quantum expectation value is the mean value obtained from repeated, independent measurements of a physical system, in the limit that the fields become classical we can identify the N-point quantum expectation values of u_k as the N^{th} moments of the probability distribution for a random classical field. The two-point function on super-horizon scales then defines the variance of the classical probability distribution from which the $|u_k|$ are drawn:

$$\langle 0| \hat{u}_k \hat{u}_q^\dagger |0\rangle_{k,q \ll aH} = P_u(k) \delta(\mathbf{k} - \mathbf{q}), \tag{1.36}$$

where $P_u(k)$ is called the *power spectrum* for u_k.

From here on we will drop the hat over the quantum operators and infer whether it is an operator or c-number from context.

1.5 Multifield inflation

The remainder of this thesis will be concerned with the behavior of inflation models outside of this simple description. In particular, we will perform an in-depth study of multifield inflation, which is a class of models that use more than one light scalar field to drive the inflationary dynamics. These are well-motivated scenarios for the early universe that naturally appear in high energy theories such as string theory or supersymmetry. Furthermore, given that the single-field inflation mechanism that we described in Sect. 1.4 is easy to realize phenomenologically, we can treat multifield models as a generalization of the picture presented above. These models have interestingly different behavior that makes their analysis significantly more difficult than the simplest case.

The role of initial conditions.— Multifield inflation has a number of potentially observable signatures, including large amounts of primordial non-Gaussianity and a non-standard relationship between the tensor and scalar power spectra. In this thesis we will be primarily concerned with the issue of how the predictions of multifield inflation models depend on their classical initial conditions. For a given set of Lagrangian parameters, *e.g.*, masses and couplings, there is a family of inflationary solutions corresponding to different choices of initial conditions for the background spacetime. Each initial condition may result in a slightly different evolution for the potential energy and its derivatives, resulting in quantitatively different behavior for the model as modes of interest exit the comoving Hubble horizon. We can see the difference in multifield and single-field behavior in Fig. 1.1.

Additionally, in Sect. 1.4.2 we saw that the field perturbations do not evolve in single-field inflation outside of the horizon, which is also true for the comov-

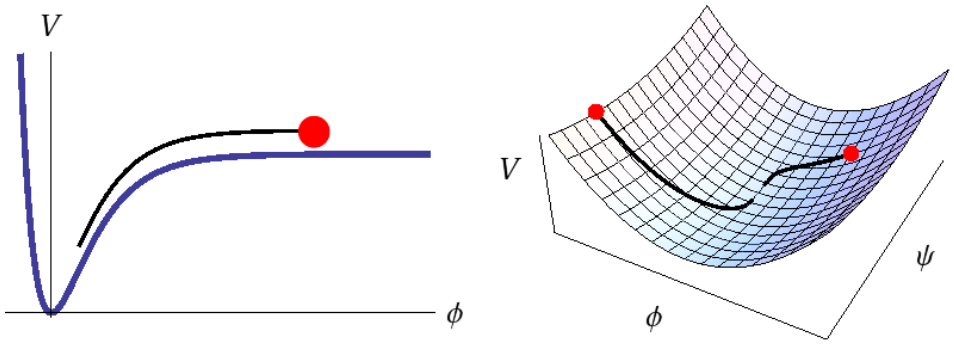

Figure 1.1: Inflationary solutions for a single-field (*left*) and multifield (*right*) model. The red dots are field-space initial conditions and their potential energy V, which are assumed to start in slow-roll. The black line is the field-space trajectory and its V, which is offset a small amount to make it easy to visualize. The blue line (*left*) and background (*right*) indicate a toy V. Most multifield models have a variety of initial conditions that lead to inflationary solutions.

ing curvature perturbation ζ. However, multifield models that have solutions that turn in field space will have significantly non-adiabatic evolution and ζ will evolve on super-horizon scales when this happens. Consequently, to understand the predictions of multifield models we will need to follow the solution to the multifield Klein-Gordon equations until an approximately adiabatic configuration is reached.

Gravitational wave consistency relation.— Of particular importance to this thesis' Chapter 6 is the gravitational wave consistency relation [14, 15], which relates the tensor spectral index n_t to the tensor-to-scalar ratio r at the pivot scale by

$$\frac{n_t}{r} = -\frac{1}{8}. \tag{1.37}$$

This is valid for all single-field models with minimal coupling to gravity during a period of slow-roll inflation, but can break down explicitly for multifield inflation. Consequently, any detected deviation from this relationship may indicate that the simplest single-field description of inflation has broken down or possibly that inflation did not happen at all. It is therefore vitally important that we understand the predictions for n_t/r in multifield models with arbitrary initial conditions, in order that we may use any potential detections of this relationship to constrain or verify non-standard models.

1.6 Thesis outline

This thesis presents five independently published chapters that examine the role of initial conditions in making predictions for multifield inflation models. This involves detailed study of both (A) the nonlinear behaviour in the background Klein-Gordon equations for multifield systems and (B) the linear, but complex relationship between adiabatic and isocurvature perturbations in multifield systems. There is a significant numerical component to this work, as well as many analytical calculations that guide our understanding of the sytems.

We start first in Chapter 2 by describing the Fortran computer program MultiModeCode, which was written to numerically solve the multifield equations of motion to first order in the field perturbations. This involves a significant exposition on the dynamics of multifield perturbation theory and looks at the predictions of an interesting multifield system that has a series of hyperbolic tangent steps in the potential energy density.

We then restrict ourselves in Chapter 3 to looking at the role of initial conditions at the level of the classical background, by examining the classical

hybrid inflation model's ability to inflate for a sample of initial conditions. The numerical solutions allow us to identify the end-state of allowed inflationary initial conditions and identify whether or not they are able to inflate sufficiently to result in a universe that looks like ours. In Chapter 4 we use lattice PDE solvers to upgrade the analysis in Chapter 3 to include pre-inflationary inhomogeneities that have wavelengths smaller than the Hubble radius.

The third portion of the thesis looks more specifically at the perturbation spectrum resulting from large-field inflation models. As these models depend on the background initial conditions, we study the sensitivity of these models' predictions to the *a priori* assumptions that we place on the allowed initial states. We do this both numerically and analytically, finding sharp, generic predictions for these types of multifield models. We conclude the thesis with a discussion on initial conditions, Bayesian methods, and how to understand the uncertainty in a theory's predictions.

PART II

A Numerical Approach

Chapter 2

MultiModeCode

This chapter is adapted from:

L. C. Price, J. Frazer, J. Xu, H. V. Peiris, and R. Easther

MultiModeCode*: An efficient numerical solver for multifield inflation*

JCAP 1503 (2015), 03 005, [16]

2.1 Abstract

We present MultiModeCode,[1] a Fortran 95/2000 package for the numerical exploration of multifield inflation models. This program facilitates efficient Monte Carlo sampling of prior probabilities for inflationary model parameters and initial conditions and is the first publicly available code that can efficiently generate large sample-sets for inflation models with $\mathcal{O}(100)$ fields. The code numerically solves the equations of motion for the background and first-order perturbations of multi-field inflation models with canonical kinetic terms and arbitrary potentials, providing the adiabatic, isocurvature, and tensor power spectra at the end of inflation. For models with sum-separable potentials MultiModeCode also computes the slow-roll prediction via the δN formalism for easy model exploration and validation. We pay particular attention to

[1] Available at www.modecode.org.

the isocurvature perturbations as the system approaches the adiabatic limit, showing how to avoid numerical instabilities that affect some other approaches to this problem. We demonstrate the use of MultiModeCode by exploring a few toy models. Finally, we give a concise review of multifield perturbation theory.

2.2 Introduction

Many simple models of inflation adeptly reproduce the observed properties of the primordial cosmological perturbations [5,17–19], predicting a nearly scale-invariant power spectrum and minimal amounts of primordial non-Gaussianity. In the slow-roll, single-field paradigm the predictions of a given model are easily determined as an algebraic function of the field's potential V and its derivatives in terms of a hierarchy of slow-roll parameters. The resulting observables are simple to compute and easy to interpret.

However, relaxing any of the basic assumptions of the slow-roll, single-field models complicates this simple analysis. In particular, for many inflationary scenarios (*e.g.*, multifield inflation, gauge inflation, and non-minimal couplings), the background and mode equations are complex systems of coupled, nonlinear ODEs, making analysis difficult in all but a few cases. Furthermore, while slow-roll, single-field inflation is a simple and easily understood model, it may not necessarily be considered natural in the context of high-energy theories. For example, low energy effective theories derived from string theory generically contain hundreds of scalar fields with complicated interactions, and many theories consider non-minimal couplings to the Ricci scalar (for a recent review, see Ref. [20]). While analytical studies have been able to overcome subsets of these problems, most of the techniques that have been used are

situation-specific, which limits their applicability to novel models.

While significant progress can be made in the slow-roll limit, only numerical techniques can explore the full predictions of more complex inflation models. Even in the purely homogeneous limit, numerically solving the nonlinear Klein–Gordon equation for the homogeneous background fields reveals many interesting features that do not arise in slow-roll analyses, *e.g.*, sensitivity to initial conditionsas studied in Refs [21, 22] and Chapters 3 and 4. These complications lead naturally to the numerical exploration of inflationary models.

In this chapter we present and describe MultiModeCode, an efficient Fortran 95/2000 package that numerically solves the equations of motion for the background fields and the first-order perturbations for multifield inflation models in which the fields have canonical kinetic terms and are minimally coupled to gravity. MultiModeCode calculates the adiabatic, tensor, and various isocurvature power spectra as a function of scale k, but does not evaluate higher order correlators. If the potential is sum-separable, MultiModeCode uses the solution to the background equations of motion to evaluate the slow-roll δN predictions for the scalar and tensor power spectra and their derivatives near the pivot scale k_*, also giving the slow-roll results for n_s, r, $f_{\rm NL}$, etc. The code has been extensively tested with various compilers, including the open-source GNU Fortran compiler.

Several numerical codes have been developed to study single-field models [23–31]. Here, we build on ModeCode [32–34], which was developed to test single-field inflation models and interfaced with tools such as CAMB [35], CosmoMC [36], and MultiNest [37]. ModeCode was designed for the Bayesian analysis of inflation and used by the *Planck* collaboration [19] to obtain the posterior probabilities and marginal likelihoods for inflation models. Moving to the multifield case significantly increases the numerical demands on

the solver, and puts a premium on efficiency due to the much greater computational resources required by these analyses. A few codes exist to analyze multifield models, but the publicly available codes are inadequate for models with many fields and arbitrary potentials. Notably, Pyflation [38–41] is an object-oriented Python code that uses the same method we employ here for solving the perturbation equations, but cannot easily generate large samples due to the speed constraints imposed by a dynamic programming language.

This significant extension to ModeCode can be used to study the power spectra of analytically intractable multifield inflationary potentials, and to explore the generic predictions of complex models by marginalizing over large numbers of possible parameters. Complementing currently available codes [38–41], MultiModeCode specializes in obtaining large Monte Carlo samples of initial conditions and parameter prior probabilities. To help users familiarise themselves with MultiModeCode the package includes initial conditions priors used in Ref. [42] and Chapters 3 and 5. The ability of this code to efficiently generate large Monte Carlo samples has permitted studies of the generic predictions of multifield inflation models with more than 100 fields, as in Chapters 5 and 6.

In practice, the code can simulate the evolution of the mode equations for $\mathcal{O}(10^2)$ fields,[2] but will become inefficient for significantly more fields due to the increasing dimensionality of the system, which increases with the number of fields as $\mathcal{O}(N_f^2)$. However, it can efficiently sample the evolution of the background equations of motion for at least $\mathcal{O}(10^3)$ fields. While solving just the background equations allows the exploration of background dynamics for such a large number of fields, if the model is sum-separable, then it will also

[2]Estimates regarding field number are based on N_f-quadratic inflation, which is not numerically intensive.

give the slow-roll predictions for the adiabatic curvature power spectrum, as well as $f_{\rm NL}$ and $\tau_{\rm NL}$, in terms of the δN approximation. This should be valid when the fields are much lighter than H at horizon crossing and slow-roll holds throughout the duration of inflation. MultiModeCode is released with several example models already implemented and it is straightforward to add to this number.

In §4.5, we demonstrate the features of MultiModeCode with an N_f–flation potential with a sharp step, which we parametrize by a hyperbolic tangent function, following Refs. [23, 43]. We show that, in addition to oscillatory features in the adiabatic curvature power spectrum that are expected from the single-field analysis [23, 44], with more than one field there are also oscillatory features in the isocurvature spectra, which might result in non-trivial evolution of the power spectrum after inflation. We also show that the numerical computation of isocurvature modes results in an inherent numerical instability, since some definitions of isocurvature perturbations involve computing the difference between two quantities that are of the same order of magnitude. This induces a dominant numerical error when these two quantities begin to approach the adiabatic limit. We overcome this problem by implementing a modified definition of isocurvature perturbations [45], which is numerically stable to many more orders of magnitude than some alternative definitions. We also implement a geometrical optics indicator of isocurvature evolution as first presented in Ref. [46]. While this measure only relies on background quantities and also does not suffer from instabilities, as implemented here it does not provide an absolute value of isocurvature, only an indicator of its growth or decay.

Finally, in §2.4 we provide a concise review of multifield perturbation theory with the aim of dispelling misconceptions that exist about this topic, which the enlightened reader can skip.

2.3 Features of MultiModeCode

We begin by highlighting some of the useful characteristics of MultiModeCode.

Speed: The purpose of MultiModeCode is to provide a fast and efficient solver that is well-tested and can be applied to a wide range of possible inflationary scenarios. MultiModeCode is written in Fortran 95/2000, increasing its capabilities relative to existing codes [38–41] and making it tractable to investigate models with many fields or to obtain large Monte Carlo samples from a model's parameter space.

Generality: The code facilitates Bayesian approaches to studying inflation, where the model's parameters are drawn from prior probabilities from which we can compute a probability distribution for specified observable associated with the model. We consider simple situations, *e.g.*, evolving a model given fixed model parameters and initial conditions, as sub-cases of the more general Bayesian framework. To facilitate the use of general priors we have implemented the sampling routines in modules which are simple to adapt and restructure for the user's purposes.

Robustness: The program exits gracefully when encountering fatal errors of either a technical or cosmological nature, while also catching specific errors that might only affect one particular configuration of the model. We have extensively checked the program output on various Macintosh and Linux machines with both the gfortran and ifort compilers, and include both a fourth-order Runge-Kutta integrator and an implicit backward-difference formula method, which is suitable for stiff problems.

Statistics: MultiModeCode provides pivot-scale observables, summarized in Table 2.1 and can sample the adiabatic and isocurvature power spectra as a function of scale k. We have implemented a variety of numerically stable indicators of the amount of isocurvature present in the system.

Slow-roll comparison: If the potential V is sum-separable, MultiModeCode can also calculate observables using the δN approximation, which assumes slow-roll. Since these quantities rely only on solutions of the background equations of motion they are efficient and simple to calculate, scaling with the number of fields as $\mathcal{O}(N_f)$. Consequently, if the model is well-described by the slow-roll approximation between horizon crossing and the end of inflation, computing observables in the δN formalism is efficient and easy.

2.4 A brief review of multifield perturbation theory

We begin with a short review of first-order, non-interacting multifield perturbation theory before describing MultiModeCode and the dynamics of many-field inflation. There are some substantial differences between single-field and multifield inflation, which we highlight in Section 2.4.1. Table 2.1 gives a list of the pivot-scale observables that MultiModeCode computes.

There are a few excellent reviews of this topic [10, 39, 47, 48] and we particularly recommend Refs. [49, 50] for more information. We first present the nuts-and-bolts of the mode function approach to first-order, multifield perturbations, which is implemented in MultiModeCode. Then we describe the widely-used δN-formalism, which has also been implemented for ease of use and for comparison to the perturbation solutions.

Power spectra (PS)	Type	Reference
$\mathcal{P}_\mathcal{R}(k)$	Adiabatic scalar spectrum	Eq. (5.5)
$\mathcal{P}_\mathcal{S}(k)$	Isocurvature spectrum	Eq. (5.6)
$\mathcal{P}_\mathrm{Pnad}(k)$	Non-adiabatic pressure spectrum	Eq. (2.36)
$\mathcal{P}_\mathrm{ent}(k)$	Entropic spectrum	Eq. (2.39)
$\mathcal{C}_{\mathcal{RS}}(k)$	Adiabatic–non-adiab. cross spectrum	Eq. (2.29)
$\mathcal{P}_h(k)$	Tensor spectrum	–
Observable at k_*	**Name**	**Description**
A_s	Scalar amplitude	$\mathcal{P}_\mathcal{R}(k_*)$
A_iso	Isocurvature ampl.	$\mathcal{P}_\mathcal{S}(k_*)$
A_Pnad	Non-adiab. pressure ampl.	$\mathcal{P}_\mathrm{Pnad}(k_*)$
A_ent	Entropy ampl.	$\mathcal{P}_\mathrm{ent}(k_*)$
A_Cross	Cross spectra ampl.	$\mathcal{C}_{\mathcal{RS}}(k_*)$
n_s	Scalar spectral index	$\mathcal{D}_* \log \mathcal{P}_\mathcal{R} + 1$
n_t	Tensor spectral index	$\mathcal{D}_* \log \mathcal{P}_h$
n_iso	Isocurvature spectral index	$\mathcal{D}_* \log \mathcal{P}_\mathcal{S}$
n_ent	Entropy spectral index	$\mathcal{D}_* \log \mathcal{P}_\mathrm{ent}$
n_Pnad	Non-adiab. pressure spectral index	$\mathcal{D}_* \log \mathcal{P}_\mathrm{Pnad}$
α_s	Scalar running	$\mathcal{D}_*^2 \log \mathcal{P}_\mathcal{R}$
r	Tensor-to-scalar ampl.	$\mathcal{P}_h(k_*)/\mathcal{P}_\mathcal{R}(k_*)$
$\cos\Delta$	ω-s correlation angle	Eq. (3.11)

Table 2.1: Typical observables at the pivot scale k_*. The derivative $\mathcal{D}_* \equiv \mathrm{d}/\mathrm{d}\log k$ is evaluated at $k = k_*$. MultiModeCode can also generate the full power spectra as a function of scale $\mathcal{P}(k)$.

2.4.1 The highlights

Multifield inflation differs from the single field case in the following important respects.

Isocurvature: Multifield inflation generally permits both adiabatic and isocurvature perturbations. Adiabatic perturbations are related by a gauge transformation to the curvature perturbation on comoving hypersurfaces $\mathcal{R}$, while isocurvature perturbations are *entropic* perturbations between different matter components on flat hypersurfaces. In single-field inflation there is only one matter component, so there are only adiabatic perturbations.

Super-horizon evolution: Isocurvature perturbations source adiabatic perturbations, causing them to evolve even on super-horizon scales. While this can generate novel signatures such as non-Gaussianity, this can also be problematic for comparing the predictions of a model with observation: unless isocurvature modes decay into an *adiabatic limit* before the end of inflation, the curvature perturbation does not become conserved and is thus sensitive to post-inflationary physics.

The two-index mode function: With more than one field, either (a) the direct interaction between fields or (b) the gravity-mediated interaction will mix the particle creation and annihilation operators as a function of time [49]. Instead of a single index mode function, we therefore need to solve for a mode matrix ψ_{IJ}, where $\delta\phi_I = \psi_{IJ}a^J$, for N_f annihilation operators a^J.

Initial conditions dependence: Multifield inflation models have an infinite number of possible inflationary solutions each of which can, in principle yield a different perturbation spectrum. Consequently, the observable spectra for

multifield models can depend on their initial conditions in ways that have no direct analogue in slow-roll, single-field models, which have only one possible trajectory in field-space.

Inherently stochastic predictions: Even if the potential V is completely fixed, multifield models will give an inherent spread of predictions due to the allowed variance in the fields' initial conditions. In general, multifield models will predict a variety of spectra, unless the stochasticity in the initial conditions can be controlled *a priori*.

2.4.2 Classical background

Consider N_f scalar fields ϕ_I with the matter sector of the action given by

$$S = \int d^4x\sqrt{-g}\left[-\frac{1}{2}\partial_\mu\phi_I\partial^\mu\phi^I - V(\phi_I)\right], \tag{2.1}$$

where we use the Einstein summation convention over repeated indices. Greek indices describe spacetime, going from $0,\ldots,3$, upper-case Latin indices describe the number of fields, going from $1,\ldots,N_f$, and lower-case Latin indices describe space, going from $1,\ldots,3$. The field space indices are raised using the Kronecker delta δ^{IJ}. The determinant of the spatial metric $g_{\mu\nu}$ is g. In this chapter we only consider inflation models with minimal coupling to Einstein gravity and a matter sector described by scalar fields. The current incarnation of MultiModeCode only solves models with canonical kinetic terms, but implementing these general field-space metrics is straightforward since MultiModeCode has been written modularly, but is left for future work.

First-order, non-interacting perturbation theory separates the homogeneous, classical background from the spatially-dependent modes as $\phi_I(t,\vec{x}) \to \phi_I(t) + \delta\phi_I(t,\vec{x})$, where we assume that these two components can be treated indepen-

dently. The homogeneous background fields obey the Klein–Gordon equations

$$\ddot{\phi}_I + 3H\dot{\phi}_I + \frac{\partial V}{\partial \phi^I} = 0, \tag{2.2}$$

where an overdot indicates a derivative with respect to cosmic time t and we use ${M_{\rm Pl}}^2 = (8\pi G)^{-1} = 1$ throughout this chapter. The 0-0 Einstein field equation gives the Friedmann equation

$$3H^2 = \frac{1}{2}\dot{\phi}_I\dot{\phi}^I \ + V(\phi_I), \tag{2.3}$$

which can be differentiated with respect to t to yield

$$2\dot{H} = -\dot{\phi}_0^2. \tag{2.4}$$

In Eq. (2.4) we have used the inflaton *trajectory velocity*, $\dot{\phi}_0^2 \equiv \dot{\phi}_I\dot{\phi}^I$. We can regard the composite field ϕ_0 as the clock of multifield inflation. It is the classical field defined along the inflaton trajectory, and represents the length of the classical field-space path.

In practice, if the dynamics are inflationary, it is numerically convenient to evolve the equation with the number of e-folds $N_e \equiv \ln a(t)$ as the independent variable, giving

$$\frac{{\rm d}^2\phi_I}{{\rm d}N_e^2} + (3-\epsilon)\frac{{\rm d}\phi_I}{{\rm d}N_e} + \frac{1}{H^2}\frac{\partial V}{\partial \phi^I} = 0, \tag{2.5}$$

where we have defined the first slow-roll parameter as

$$\epsilon \equiv -\frac{\dot{H}}{H^2} = \frac{1}{2}\frac{{\rm d}\phi_I}{{\rm d}N_e}\frac{{\rm d}\phi^I}{{\rm d}N_e}. \tag{2.6}$$

The Friedmann equation (2.3) can then also be expressed as

$$H^2 = \frac{V}{3-\epsilon}. \tag{2.7}$$

If $V \approx 0$, Eq. (2.7) requires $\epsilon \approx 3$, which will result in numerical instability whenever we try to set initial conditions that are dominated by their kinetic

energy. We side-step this issue by using the cosmic time Eq. (2.2) and H as defined in Eq. (2.3).

Solving Eq. (2.5) therefore only requires the initial conditions ϕ_I and $\mathrm{d}\phi_I/\mathrm{d}N_e$, because the dependence on the scale factor a is explicitly removed by the 0-0 Einstein equation (2.7) as a result of assuming a flat FLRW spacetime. As mentioned in §2.4.1, the perturbation spectrum depends on these initial conditions, which are specified as a prior probability distribution $P(\phi_I, \phi_I')$.

2.4.3 Mode equations

To obtain the first-order equation of motion for the perturbations $\delta\phi_I$, we need to expand the action (2.1) to second-order and include the first-order scalar perturbations to the flat FLRW metric, given by

$$\mathrm{d}s^2 = -(1+2\Phi)\,\mathrm{d}t^2 - 2a^2 B_{,i}\,\mathrm{d}t\,\mathrm{d}x^i + a^2\left[(1-2\Psi)\,\delta_{ij} - 2\partial_{\langle i}\partial_{j\rangle}E\right]\mathrm{d}x^i\mathrm{d}x^j, \quad (2.8)$$

where

$$\partial_{\langle i}\partial_{j\rangle}E \equiv \partial_i\partial_j E - \frac{1}{3}\delta_{ij}\nabla^2 E \quad (2.9)$$

is trace-free. We choose the spatially-flat gauge, so that $\Psi = E = 0$, and vary the expanded action δS_ϕ with respect to the perturbations $\delta\phi_I(t, \vec{x})$ to get the first-order equation of motion for the free-field perturbations. After Fourier-transforming the scalar perturbations to $\delta\phi_I(\mathbf{k})$, the mode equations in this gauge are

$$\frac{\mathrm{d}^2\delta\phi_I}{\mathrm{d}N_e^2} + (3-\epsilon)\frac{\mathrm{d}\delta\phi_I}{\mathrm{d}N_e} + \frac{k^2}{a^2H^2}\delta\phi_I + C_{IJ}\delta\phi^J = 0, \quad (2.10)$$

where

$$C_{IJ} \equiv \frac{\partial_I\partial_J V}{H^2} + \frac{1}{H^2}\left(\frac{\mathrm{d}\phi_I}{\mathrm{d}N_e}\partial_J V + \frac{\mathrm{d}\phi_J}{\mathrm{d}N_e}\partial_I V\right) + (3-\epsilon)\frac{\mathrm{d}\phi_I}{\mathrm{d}N_e}\frac{\mathrm{d}\phi_J}{\mathrm{d}N_e} \quad (2.11)$$

and $\partial_I \equiv \partial/\partial\phi_I$. The equation of motion for the tensor metric perturbations can be derived similarly; since the non-gauge degrees of freedom are massless

and only minimally coupled to the matter sector, the resulting equations of motion are identical to the case of single-field inflation.

To solve the perturbation equations, it is usually convenient to work with the Mukhanov–Sasaki variable $u_I \equiv a\delta\phi_I$. The mode equation for u_I is

$$\frac{\mathrm{d}^2 u_I}{\mathrm{d}N_e^2} + (1-\epsilon)\frac{\mathrm{d}u_I}{\mathrm{d}N_e} + \left(\frac{k^2}{a^2H^2} - 2 + \epsilon\right) u_I + C_{IJ}u^J = 0 \tag{2.12}$$

with C_{IJ} as in Eq. (2.11). Since the mass matrix, defined as $m_{IJ}^2 \equiv \partial_I\partial_J V$, is not necessarily diagonal, the perturbation equations (2.12) mix the annihilation operators for all of the fields [49]. We therefore need to expand each perturbation mode $u_I(\mathbf{k})$ and $u_I^\dagger(\mathbf{k})$ using N_f harmonic oscillators $a_J(\mathbf{k})$:

$$u_I(\mathbf{k}, N_e) = \psi_I{}^J(\mathbf{k}, N_e) a_J(\mathbf{k}) \tag{2.13}$$

and

$$u_I^\dagger(\mathbf{k}, N_e) = \psi_I{}^{J,*}(\mathbf{k}, N_e) a_J^\dagger(\mathbf{k}), \tag{2.14}$$

where $(\dagger)$ and $(*)$ represent Hermitian and complex conjugation, respectively.[3] We can then define canonical commutation relations

$$[a_J(\mathbf{k}), a_I^\dagger(\mathbf{k}')] = (2\pi)^3 \delta_{IJ}\delta^{(3)}(\mathbf{k} - \mathbf{k}'). \tag{2.15}$$

The mode matrix ψ_{IJ} evolves according to

$$\frac{\mathrm{d}^2\psi_{IJ}}{\mathrm{d}N_e^2} + (1-\epsilon)\frac{\mathrm{d}\psi_{IJ}}{\mathrm{d}N_e} + \left(\frac{k^2}{a^2H^2} - 2 + \epsilon\right)\psi_{IJ} + C_{IL}\psi^L{}_J = 0. \tag{2.16}$$

Finding the perturbation spectrum requires setting initial conditions in Eq. (2.16) and using the background equations (2.5) to find the time $N_{e,\mathbf{k}}$ when the mode $\mathbf{k}$ leaves the horizon, which also depends on the moment at which the pivot scale k_* leaves the horizon, N_* e-folds before the end of inflation.

[3] An alternative approach is to simply bypass this issue by solving for the field correlation functions directly rather than the individual modes, as in the transport method [46, 51–53].

The usual initial condition is the Bunch-Davies state [54], which assumes the field basis has been chosen such that the ψ_{IJ} are originally diagonal and sets the initial condition for Eq. (2.16) as if the mode matrix were freely oscillating in Minkowski space. This is well-motivated, since for modes deep in the horizon $k \gg aH$, the mode matrix ψ_{IJ} obeys the free wave equation in conformal time

$$\frac{\mathrm{d}^2\psi_{IJ}}{\mathrm{d}\tau^2} + k^2\psi_{IJ} = 0, \tag{2.17}$$

where $d\tau \equiv a\,dt$. If we assume that the mode matrix is initially diagonal at $\tau = -\infty$, then Eq. (2.17) yields two solutions

$$\psi_{IJ} = \frac{1}{\sqrt{2k}}\left(C_1 e^{ik\tau} + C_2 e^{-ik\tau}\right)\delta_{IJ}. \tag{2.18}$$

Translating to e-fold time, the initial conditions can be set by

$$\psi_{IJ}\Big|_{N_e=0} = \frac{1}{\sqrt{2k}}\left(C_1 + C_2\right)\delta_{IJ} \tag{2.19}$$

and

$$\frac{\mathrm{d}\psi_{IJ}}{\mathrm{d}N_e}\Big|_{N_e=0} = \frac{i}{aH}\sqrt{\frac{k}{2}}\left(C_1 - C_2\right)\delta_{IJ}\ . \tag{2.20}$$

The Bunch-Davies initial condition is equivalent to choosing $C_1 = 0$ and $C_2 = 1$. While only the Bunch-Davies initial condition is implemented in MULTIMODECODE, non–Bunch-Davies modes could be easily accommodated.

Although the u_I's are convenient for short wavelength modes, they grow exponentially after the modes exit the horizon. So once the mode is outside the horizon, MULTIMODECODE switches from u_I to $\delta\phi_I$ by matching boundary conditions at a time N_e^* just after horizon crossing with

$$u_I\Big|_{N_e^*} = e^{N_e^*}\delta\phi_I\Big|_{N_e^*} \qquad \text{and} \qquad \frac{\mathrm{d}u_I}{\mathrm{d}N_e}\Big|_{N_e^*} = e^{N_e^*}\left(\delta\phi_I + \frac{\mathrm{d}\delta\phi_I}{\mathrm{d}N_e}\right)\Big|_{N_e^*}. \tag{2.21}$$

2.4.4 Power spectra

Unlike single-field inflation, the multifield power spectrum involves contractions of the mode matrix. Using the canonical commutation relations above, the two-point VEV of the field perturbations yields the power spectrum

$$P^{IJ}_{\delta\phi}(k) = \frac{k^3}{2\pi^2}\left[\frac{1}{a^2}\right]\psi^I_L\,\psi^{JL,*}\,. \tag{2.22}$$

When the field trajectories are not turning, on super-horizon scales the fields ϕ_I and their momenta π_I commute, indicating that they have transitioned to a regime where Eq. (2.22) can be interpreted as an expectation value over realizations of classical, random fields.

To relate this field-space power spectrum to gauge-invariant perturbation variables [55–57], we first define the curvature perturbation on comoving hypersurfaces $\mathcal{R}$ by

$$\mathcal{R} \equiv \Psi + \frac{1}{3}\nabla^2 E + aH\left(B + v\right), \tag{2.23}$$

where v is given in terms of the momentum density of the stress-energy tensor $T^{\mu}_{\ \nu}$ as

$$T^{i}_{\ 0} \equiv \left(\bar{\rho} + \bar{P}\right)\delta^{ij}\frac{\partial v}{\partial x^j}, \tag{2.24}$$

where $\bar{\rho}$ and $\bar{P}$ are the background energy and pressure densities, respectively. If we evaluate Eq. (2.23) on spatially-flat hypersurfaces during inflation, $\mathcal{R}$ reduces to

$$\mathcal{R} = -\frac{H}{\dot{\phi}_0}\,\omega_I \delta\phi^I, \tag{2.25}$$

where $\omega_I \equiv \dot{\phi}_I/\dot{\phi}_0$ is a basis vector that projects $\delta\phi_I$ along the direction of the classical background trajectory, given by the solutions to Eq. (2.5). The vector $\vec{\omega}$ and a complementary set of $(N_f - 1)$ mutually orthonormal basis vectors $\vec{s}_K$ form the kinematic basis [58, 59], where the separation between the adiabatic perturbations in Eq. (2.25) and transverse, isocurvature perturbations is made

explicit. Since $\vec{\omega}$ depends on the nonlinear background evolution, in MULTIMODECODE we find the $\vec{s}_K$ numerically by Gram–Schmidt orthogonalization.

The *adiabatic curvature power spectrum* $\mathcal{P}_\mathcal{R}$ is then the projection of $\mathcal{P}^{IJ}_{\delta\phi}$ along the field vector ω_I, scaled by the pre-factor in Eq. (2.25), leaving

$$\mathcal{P}_\mathcal{R}(k) = \frac{1}{2\epsilon}\omega_I\omega_J\mathcal{P}^{IJ}_{\delta\phi}(k). \tag{2.26}$$

The gauge-invariant scalar density spectrum in Eq. (5.5) is the final result for the adiabatic two-point function to first-order in perturbation theory.

Since Eqs. (2.25) and (5.5) are projected along $\vec{\omega}$, a simple definition for the isocurvature perturbations $\mathcal{S}_K$ is the orthogonal projection along the $\vec{s}_K$ directions

$$\mathcal{S}_K \equiv -\frac{H}{\dot{\phi}_0}s_K{}^J\delta\phi_J. \tag{2.27}$$

By projecting $\mathcal{P}^{IJ}_{\delta\phi}$ onto all the directions s_K that are orthogonal to ω_I and scaling the result as in Eq. (5.5), leads to the *isocurvature power spectrum*:

$$\mathcal{P}_\mathcal{S}(k) = \frac{1}{2\epsilon}\sum_{KL}^{N_f-1}\sum_{IJ}^{N_f} s_I{}^K s_J{}^L\,\mathcal{P}^{IJ}_{\delta\phi}(k), \tag{2.28}$$

where we have left the summations explicit to indicate that the isocurvature basis vectors are (N_f-1)–dimensional. We include this definition of isocurvature because it is numerically stable, as we discuss in §2.6.1.

Similarly, we define the *adiabatic-isocurvature cross-spectra* $\mathcal{C}_{\mathcal{RS}}$, which is the cross-correlation between the comoving curvature perturbation and the total isocurvature perturbation, given by the contraction of $\mathcal{P}^{IJ}_{\delta\phi}$ with both ω and the isocurvature basis vectors s_K

$$\mathcal{C}_{\mathcal{RS}}(k) = \frac{1}{2\epsilon}\sum_{K}^{N_f-1}\sum_{IJ}^{N_f}\omega_I s_K^J\left(\mathcal{P}^{IJ}_{\delta\phi} + \mathcal{P}^{JI}_{\delta\phi}\right). \tag{2.29}$$

Cross-correlations are generically expected if the background trajectory is curved as modes of interest leave the horizon. By parametrizing Eq. (2.29)

with the scalar value

$$\cos\Delta \equiv \frac{\mathcal{C}_{\mathcal{RS}}}{\sqrt{\mathcal{P}_{\mathcal{R}}\,\mathcal{P}_{\mathcal{S}}}}, \tag{2.30}$$

it was shown in Ref. [60] that, for the case of $N_f = 2$, the value of r is suppressed relative to the single-field, slow-roll expectation by $r \approx 16\epsilon \sin^2\Delta$, to first-order in slow-roll. In principle, Δ may be detectable from CMB observations [61,62].

However, by differentiating Eq. (2.23) with respect to time t, the comoving curvature perturbation will not necessarily be constant even for $k \ll aH$. Instead,

$$\dot{\mathcal{R}} = -\frac{H}{\dot{\phi}_0^2}\delta P_{\rm nad}, \tag{2.31}$$

where $\delta P_{\rm nad}$ is the non-adiabatic pressure perturbation [11,63,64]. This quantity is the difference between the total pressure perturbation

$$\delta P = \sum_I \left[\dot{\phi}_I \delta\dot{\phi}_I - \dot{\phi}_I^2\Phi - V_{,I}\delta\phi_I\right], \tag{2.32}$$

and the adiabatic pressure perturbation $\delta P_{\rm ad} = c_s^2\delta\rho$, where the speed of sound is $c_s^2 = \dot{P}/\dot{\rho}$ and the lapse function is

$$\Phi = \frac{1}{2H}\dot{\phi}_I\delta\phi^I, \tag{2.33}$$

defined in the spatially-flat gauge [65]. Given the total density perturbation

$$\delta\rho = \sum_I \left[\dot{\phi}_I \delta\dot{\phi}_I - \dot{\phi}_I^2\Phi + V_{,I}\delta\phi_I\right], \tag{2.34}$$

the *non-adiabatic pressure power spectrum* $\mathcal{P}_{\rm Pnad}$ reduces to

$$\mathcal{P}_{\rm Pnad}(k) = \frac{k^3}{2\pi^2 a^2}\quad \left[A^I A^J \psi_I{}^L \psi^*_{LJ} + A^I B^J \psi_I{}^L \psi'_{LJ} + B^I A^J \psi^*_J{}^L \psi'_{LI} + B^I B^J \psi'_I{}^L \psi^{*\prime}_{LJ}\right], \tag{2.35}$$

where $(\prime)$ indicates a derivative with respect to e-foldings N_e and we have defined the vectors

$$A_I = \frac{1}{3aH^2\epsilon}\phi'^{,L}\left[\left(-3H^2\phi'_L - \partial_L V\right)\partial_I V + H^2\partial_M V\,\phi'^{,M}\left(\delta_{LI} + \frac{1}{2}\phi'_L\phi'_I\right)\right] \tag{2.36}$$

and

$$B_I = \left(1 - c_s^2\right) H^2 \phi_I'. \tag{2.37}$$

By analogy to Eq. (2.27), we can build an entropy perturbation from the non-adiabatic pressure perturbation [39, 58, 66], with

$$\delta S = \frac{H}{\dot{P}} \delta P_{\rm nad}. \tag{2.38}$$

From this we obtain our final definition of isocurvature, the *comoving entropy spectrum*, given by

$$\mathcal{P}_{\rm ent}(k) = \left(\frac{H}{\dot{P}}\right)^2 \mathcal{P}_{\rm Pnad}. \tag{2.39}$$

2.4.5 δN formalism

The separate-universe assumption [11, 67–71], often referred to as δN, states that when smoothed on some physical scale much larger than the horizon, the evolution of each smoothed patch can be computed using only background quantities. By identifying that $\zeta = \delta N$, where ζ is the curvature perturbation on constant density hypersurfaces and δN measures the variation in the number of e-folds between an initial flat hypersurface and a subsequent constant density hypersurface, Lyth and Rodriguez demonstrated that this assumption can be taken advantage of when computing correlation functions by performing a Taylor expansion in terms of the initial conditions [72].

$$\zeta = N_{,I} \delta\phi_*^I + \frac{1}{2} N_{,IJ} \delta\phi_*^I \delta\phi_*^J + \dots . \tag{2.40}$$

The main difficulty in this approach lies in computing the derivatives of the number of e-folds ($N_{,I} \equiv \partial N_e / \partial \phi^{I,*}$, $N_{,IJ}$ *etc.*). However for sum-separable models these expressions can be computed analytically [73, 74]. For models with fields much lighter than H at horizon crossing, the numerically intensive

calculation of solving for the modes may therefore be unnecessary. MULTIMODECODE implements this δN slow-roll formalism where we assume that t_* is the moment when the pivot-scale k_* leaves the horizon and that the field perturbations at this time are uncorrelated, with a power spectrum

$$\mathcal{P}_{\delta\phi}^{IJ} = \left(\frac{H}{2\pi}\right)^2 \delta^{IJ}. \tag{2.41}$$

We also assume that the tensor modes, which are massless and uncoupled to the matter sector, have a power spectrum

$$\mathcal{P}_h = 8\left(\frac{H}{2\pi}\right)^2. \tag{2.42}$$

At least to first order, on super-horizon scales $\zeta = \mathcal{R}$ [75], which allows us to compare the predicted power spectrum for ζ using the δN formalism to the adiabatic power spectrum in Eq. (5.5).

If the potential V is sum-separable so that

$$V = \sum_I V_I(\phi_I), \tag{2.43}$$

then we can use the Klein–Gordon equations (2.5) for the scalar fields to obtain a sum-separable expression for the amount of expansion between the two surfaces

$$N_e = -\sum_I \int_*^c \frac{V_I}{V_I'} d\phi_I, \tag{2.44}$$

where $V_I' \equiv dV_I/d\phi^I$. If V were not sum-separable, the derivatives of N_e would in general have to be obtained numerically by evolving the background equations of motion (2.5) on a stencil in field-space and taking the finite difference. We have not implemented this feature in MULTIMODECODE as it is at least as computationally intensive as solving the mode equations, since there would be $\mathcal{O}(N_f)$ points in the stencil, each of which requires evaluating $\mathcal{O}(N_f)$ coupled Klein-Gordon equations.

When the potential is sum-separable, the derivatives of N_e can be simplified into the expressions [73, 74]

$$N_{,I} = \frac{1}{\sqrt{2\epsilon_I^*}} \frac{V_I^* + Z_I^c}{V^*} \tag{2.45}$$

and

$$N_{,IJ} = \delta_{IJ}\left[1 - \frac{\eta_I^*}{2\epsilon_I^*}\left(\frac{V_I^* + Z_I^c}{V^*}\right)\right] + \frac{1}{\sqrt{2\epsilon_J^*}V^*}\frac{\partial Z_J^c}{\partial \phi_I^*}, \tag{2.46}$$

where

$$Z_I^c = V^c\frac{\epsilon_I^c}{\epsilon^c} - V_I^c, \tag{2.47}$$

$$Z_{IJ}^c = -\frac{V_c^2}{V^*}\sqrt{\frac{2}{\epsilon_J}}\left[\sum_{K=1}^{N_f}\epsilon_K\left(\frac{\epsilon_I}{\epsilon} - \delta_{IK}\right)\left(\frac{\epsilon_J}{\epsilon} - \delta_{JK}\right)\left(1 - \frac{\eta_K}{\epsilon}\right)\right]_c, \tag{2.48}$$

and the slow-roll parameters are

$$\epsilon \equiv \sum_I \epsilon_I = \frac{1}{2}\sum_I \frac{V_I'^2}{V^2} \tag{2.49}$$

and

$$\eta \equiv \sum_I \eta_I = \sum_I \frac{V_I''}{V}. \tag{2.50}$$

The contribution from the EOI surface is therefore completely encoded in the functions Z_I and its derivatives.

The relationship (6.4) and the expansion equation (2.44) allow us to define pivot-scale observables for the scalar perturbations ζ. We will focus on the observables obtainable only through the first and second derivatives of N_e, and express our results only to the lowest order in slow-roll. We start with the ζ power spectrum

$$\mathcal{P}_\zeta = N_{,I}N^{,I}\left(\frac{H}{2\pi}\right)^2, \tag{2.51}$$

and obtain the tensor-to-scalar ratio by comparison to the tensor spectrum (2.42)

$$r = \frac{8}{N_{,I}N^{,I}}. \tag{2.52}$$

These have simple expressions only in terms of $N_{,I}$. The adiabatic and tensor spectral indices n_s and n_t also have easily evaluated expressions

$$n_s - 1 = -2\epsilon_* - \frac{2}{N_{,I}N^{,I}} + \left(\frac{2}{V}\right)\frac{V_{,IJ}N^{,I}N^{,J}}{N_{,K}N^{,K}} \tag{2.53}$$

and

$$n_t = \frac{-2\epsilon_*}{1-\epsilon_*}. \tag{2.54}$$

The expression for the scalar running α_s is more complicated, but straightforward to compute (*e.g.*, Eq. 6.14 in Ref. [76]).

To obtain the amplitude of the predicted non-Gaussianity we further assume that the field perturbations at horizon crossing are purely Gaussian, since the non-Gaussianity generated by sub-horizon evolution of the modes is typically slow-roll suppressed [73, 77], assuming that slow-roll is not violated. Following Refs. [73, 78], we use the non-linearity parameter

$$-\frac{6}{5}f_{\rm NL} \equiv \left[\frac{\prod_i k_i^3}{\sum_i k_i^3}\right]\frac{B_\zeta}{4\pi^4\mathcal{P}_\zeta^2} \approx \frac{N_{,I}N_{,J}N^{,IJ}}{\left(N_{,K}N^{,K}\right)^2}, \tag{2.55}$$

where B_ζ is the bispectrum. Given Gaussian field perturbations at horizon crossing, the trispectrum amplitude is then parametrized by the non-linearity parameters [79, 80]

$$\tau_{\rm NL} = \frac{N_{,IJ}N^{,IK}N^{,J}N_{,K}}{\left(N_{,L}N^{,L}\right)^3} \tag{2.56}$$

and

$$g_{\rm NL} = \left(\frac{25}{54}\right)\frac{N_{,IJK}N^{,I}N^{,J}N^{,K}}{\left(N_{,L}N^{,L}\right)^3}. \tag{2.57}$$

Since $g_{\rm NL} \sim N_{,IJK}$ we do not compute it here, although it could be implemented by taking the third derivative of N_e as in Ref. [74].

2.5 The method

We outline the procedure used to obtain the power spectrum predictions, with the algorithmic structure of MultiModeCode in Algorithm 1. While this

largely follows previous implementations, such as Pyflation [38–41], we give the method for the sake of clarity and reproducibility.

We start by defining the functional form of the potential V and prior probability distribution functions (PDFs) for the parameters that define V, which we call Lagrangian parameters or model parameters, and the background initial conditions $\phi_{I,0}$ and $\phi'_{I,0}$. We treat the simple situation of exactly specifying a set of Lagrangian parameters and initial conditions as a special case, where the prior probability for these parameters is trivial. Given these priors, the program will build a numerical sample by iteration until a pre-defined number of samples is reached.

MultiModeCode first solves the background equations of motion (2.5) until the end-of-inflation. While we have included the natural condition of $\epsilon = 1$ as the default ending criterion for inflation, there is complete functionality to end inflation by another method, in particular a waterfall transition via the hybrid mechanism [81, 82] at some reference phase-space point.

Given a value for the number of e-folds N_* between when the pivot scale k_* leaves the horizon and the end-of-inflation, which is either fixed by the user or set in each iteration of the code through the sampling of a prior probability $P(N_*)$, we obtain the value of H at horizon crossing by interpolating the numerical background solution. The pivot scale k_* must be pre-defined by the user and defaults to 0.002 Mpc^{-1}. From this, we normalize the size of the universe so that $k_* = aH_*$ at $N_e = N_{\rm tot} - N_*$.

For each scale of interest k, we set the modes' initial conditions at a time $N_{e,0}$ when that mode is significantly sub-horizon, $k \gg a_0 H_0$. For the Bunch-Davis initial state, this point is chosen iteratively by making sure that the relative corrections to Eq. (2.17) that are sub-dominant for $k \gg aH$ are smaller than a pre-defined tolerance. This tolerance is set to 1×10^{-5}; from observing

Algorithm 1 MultiModeCode method

define sample size, V, k_*

for all elements in sample **do**

procedure Background Solver:

get Lagrangian parameters for V and ICs for Eq. (2.5) from prior PDF

with the end-of-inflation (EOI) criterion set by user, **solve** Eq. (2.5) until EOI

check inflation ($\ddot{a} > 0$) started and ended

procedure Scale-factor Normalizer:

get N_* from user **or** by prior PDF

check total inflationary e-folds $N_{\rm tot} \geq N_*$

define a such that $k_* = a_* H_*$ at $N_e = N_{\rm tot} - N_*$ before inflation ends

procedure δN Calculator:

if V is sum-separable, **then** calculate δN observables near k_*

for all modes k **do**

procedure Mode Initializer:

define initial time $N_{e,0}$ with $k \gg a_0 H_0$

while the corrections to Eq. (2.17) are above some tolerance:

set earlier $N_{e,0}$ and **check** $N_{e,0} > 0$

set Bunch-Davies IC for mode matrix $\psi_{IJ}(\mathbf{k})$ at $N_{e,0}$

procedure Mode Solver:

solve Eq. (2.12) until $k \approx aH$

change variable as in Eq. (2.21) and **solve** until EOI

calculate power spectra for k

procedure k_*-observable Calculator:

calculate amplitudes, spectral indices, *etc.* at k_* by finite difference in k-space

the sub-horizon evolution of the modes, using a tolerance at least this tight gives no change to the value of the modes at horizon crossing.

We then solve the mode equations (2.12) for the variable ψ_{IJ} for the period of time when the modes are smaller than the causal horizon, $k \gtrsim aH$, and then switch to a two-index matrix built from the u_I in Eq. (2.21) for super-horizon evolution. The power spectra are calculated for each k and various pivot-scale statistics are evaluated by finite-difference between a few scales k_i near k_*. If the potential V is sum-separable, the program also calculates the δN values for the observables described in Section 2.4.5.

Numerous checks are performed on the background and mode equation evolution so that MultiModeCode will fail gracefully if a fatal exception is raised and give an informative error. Similarly, if a particular initial parameter set is invalid for a non-fatal reason, MultiModeCode will iteratively generate a new set of parameters in order to explore cosmologically relevant parameter sets by rejection sampling. We have extensively tested the numerical stability of the code and have included a number of easily controllable options allowing the user to control the numerical accuracy, as well as the type of ODE solver.

2.6 Numerical results

2.6.1 Isocurvature stability

Fig. 2.1 illustrates a problem that arises when computing the isocurvature spectra $\mathcal{P}_{\rm Pnad}$ and $\mathcal{P}_{\rm ent}$. We have plotted the super-horizon evolution of the power spectra for the adiabatic and non-adiabatic pressure perturbations, as well as the adiabatic curvature, entropic, and isocurvature spectra, with $N_* =$

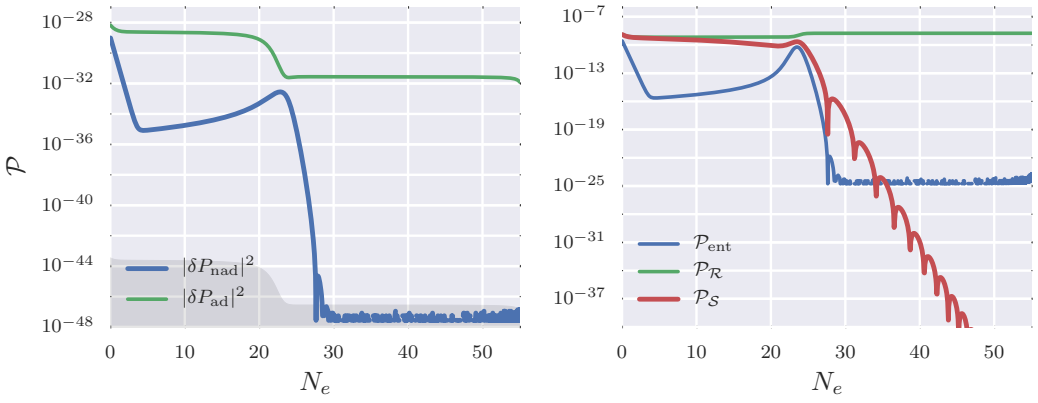

Figure 2.1: The evolution of the power spectra during the last 55 e-folds of inflation for a two-field N_f-quadratic model. (*Left*) The power spectrum for adiabatic (*green*) and non-adiabatic (*blue*) pressure perturbations δP. The total pressure spectrum and the adiabatic pressure spectrum are nearly coincident on this scale, so the total pressure spectrum $\mathcal{P}_{\delta P}$ has not been plotted. The gray area is an estimate of the region dominated by double-precision error due to round-off in $\mathcal{P}_{\rm Pnad}$. (*Right*) The power spectra for perturbations in the adiabatic curvature $\mathcal{P}_{\mathcal{R}}$, the isocurvature $\mathcal{P}_{\mathcal{S}}$, and the comoving entropy $\mathcal{P}_{\rm ent}$. $\mathcal{P}_{\rm ent}$ is a rescaling of $\mathcal{P}_{\rm Pnad}$ and is numerically unstable for $N_e \gtrsim 30$ in this model. $\mathcal{P}_{\mathcal{S}}$ is numerically stable until the end of inflation.

55, for a two-field inflation model with the potential

$$V = \frac{1}{2}m_1^2\phi_1^2 + \frac{1}{2}m_2^2\phi_2^2. \tag{2.58}$$

To match the analysis performed in Refs. [39,41,83,84] we choose $m_1^2 = 10^{-11.7}$, $m_2^2 = 10^{-10.0}$, and initial conditions $\phi_{1,0} = \phi_{2,0} = 12.0\,M_{\rm Pl}$. In particular, Fig. 2.1 can be compared directly to Figs 1 and 3 in Ref. [39]. With this choice of parameters, the background trajectory evolves primarily along the direction of the heavier field ϕ_2 for $N_e \lesssim 25$, then turns sharply toward the ϕ_1 direction for the remainder of inflation. The effect of this turn on the super-horizon perturbations can be seen clearly in the power spectra in Fig. 2.1.

In general, the calculation of $\mathcal{P}_{\rm Pnad}$ and $\mathcal{P}_{\rm ent}$ becomes dominated by numerical error as the isocurvature perturbations decay. From Fig. 2.1, regardless of the amplitude of the isocurvature modes, the adiabatic pressure perturbations $\delta P_{\rm ad} = c_s^2 \delta\rho$ do not exponentially decay between horizon exit and the end of inflation. For the example model (2.58), the power spectrum for $\delta P_{\rm ad}$ is approximately constant after the turn at $N_e \approx 25$. However, the total pressure perturbation δP is approximately equal to $\delta P_{\rm ad}$ during this time and the difference between the two reduces exponentially as the isocurvature modes decay.

Since $\delta P_{\rm nad} \equiv \delta P - \delta P_{\rm ad}$ and $\delta P_{\rm ad} \to \delta P$, the numerical accuracy for $\delta P_{\rm nad}$ is limited by the real precision of the computer, which results in a finite difference error in the numerical calculation of $\delta P_{\rm nad}$ and a loss of significance. Using standard double precision accuracy, the expected error in $\delta P_{\rm nad}$ should then be

$$\Delta_{\rm err}\mathcal{P}_{\rm Pnad} \sim \mathcal{O}(10^{-15})\, \mathcal{P}_{\delta P} \sim \mathcal{O}(10^{-15})\, \mathcal{P}_{\delta P,{\rm ad}}, \tag{2.59}$$

which is confirmed in Fig. 2.1. Without correcting for this dominant error term, the value of $\mathcal{P}_{\rm Pnad}$ will oscillate arbitrarily between zero and the limit in Eq. (2.59), which is an upper bound on the amplitude of the non-adiabatic pressure perturbations. Since entropic perturbations are usually defined as [66]

$$S_{IJ} \equiv \zeta_I - \zeta_J, \tag{2.60}$$

where ζ_I is the curvature perturbation resulting from the $I^{\rm th}$ fluid, this problem will arise naturally for all calculations of $\mathcal{P}_{\rm ent}$.

In contrast, the calculation of $\mathcal{P}_{\mathcal{S}}$ in Eq. (5.6) is directly proportional to the value of the decaying isocurvature modes in the kinematic basis. Using this isocurvature spectrum largely alleviates the numerical problems with $\delta P_{\rm nad}$, yielding a more faithful measure with a higher degree of accuracy. Figure 2.1

shows the exponential decay of $\mathcal{P}_{\mathcal{S}}$ after the super-horizon turn at $N_e \sim 25$. We compare this to $\mathcal{P}_{\rm ent}$, which becomes numerically unstable at $N_e \approx 30$, showing that the two measures $\mathcal{P}_{\mathcal{S}}$ and $\mathcal{P}_{\rm ent}$ are separated by 27 orders of magnitude at the end of inflation, despite being of the same magnitude at horizon crossing.[4]

2.6.2 A case study: N_f-flation with a step

We will show in Chapters 5 and 6 that MultiModeCode is able to produce large volume Monte Carlo samples for N_f–monomial inflation with the potential

$$V = \frac{1}{p}\sum_I \lambda_I |\phi_I|^p, \tag{2.61}$$

for real exponents p [85–94]. In Chapter 5 we will focus on the N_f–quadratic case with $p = 2$ and demonstrate that the predictions for the power spectrum do not sensitively depend on the prior probability chosen for the initial conditions of the fields. In Chapter 6 we further demonstrate this for the general case in Eq. (2.61), while focusing on the gravitational wave consistency relation. We will be able to straightforwardly compare the analytical δN results to the numerics, greatly simplifying the procedure for comparing analytical results to the full numerical calculation. We include all of the IC priors used in these papers in MultiModeCode.

[4] As the adiabatic limit is approached, $\mathcal{P}_{\mathcal{S}}$ can also receive a dominant contribution from roundoff error in the Gram-Schmidt orthogonalization procedure. If some components of the isocurvature vectors s_K^I are much smaller than others, this can result in a spurious projection of $\mathcal{P}_{\mathcal{R}}$ onto the isocurvature directions. In MultiModeCode we have included an optional subroutine `renormalize_remove_smallest` in `modpk_potential.f90`, where the components of s_K^I are set to zero if they do not affect the normalization of s_K, *i.e.*, if the value of s_K^I is indistinguishable from roundoff error. In practice, we have never seen this problem arise, so this option needs to be uncommented in the source code before compilation.

In this chapter we will instead focus on a few case studies that are interesting due to their analytic intractability. We present results for a multifield generalization of the inflationary step-potential first used in Ref. [23]. This potential has the form

$$V = \frac{1}{2}\sum_I m_I^2\phi_I^2\left[1 + c_I \tanh\left(\frac{\phi_I - \bar{\Phi}_I}{d_I}\right)\right] \tag{2.62}$$

with masses m_I and real constants d_I, c_I, and $\bar{\Phi}_I$ specifying the slope, amplitude, and position, respectively, for a step feature in the I^{th} field. Phase transitions in sectors coupled only gravitationally to the inflaton sector may generate these hyperbolic-tangent features in V and leave an observable imprint in the primordial density spectra if these symmetry breaking transitions occur during the last $\mathcal{O}(60)$ e-folds of inflation [23, 43]. In the sharp-step limit, these features introduce oscillations as a function of k into the adiabatic curvature power spectrum and a scale-dependent, oscillatory bispectrum [23, 44, 95, 96]. To keep $V > 0$ we require $c_I < 1$ and to satisfy the latest constraints on oscillations in the scalar power spectrum amplitude requires $c_I \lesssim 10^{-3}$, assuming that the step occurs as the scales relevant for the CMB leave the horizon [97–99].

With $c_I \to 0$, Eq. (2.62) is an uncoupled assisted inflation model [85, 100], first proposed in Ref. [90]. Models with a step feature are additionally interesting, because they can fit a wider range of data and have been well-studied in the single-field case. In particular, Ref. [44] contains an elegant analytical calculation for the single-field case of Eq. (2.62). However, replicating the same calculation for the general potential would be difficult — if not impossible — with the same techniques, since the possible existence of isocurvature perturbations significantly complicates the analysis. Consequently, a numerical exploration of this model is well-motivated.

Fixing the number of fields to $N_f = 10$, we set the initial conditions to $\phi_{I,0} = 10$, with the initial velocities set in slow-roll. The size and slope of the

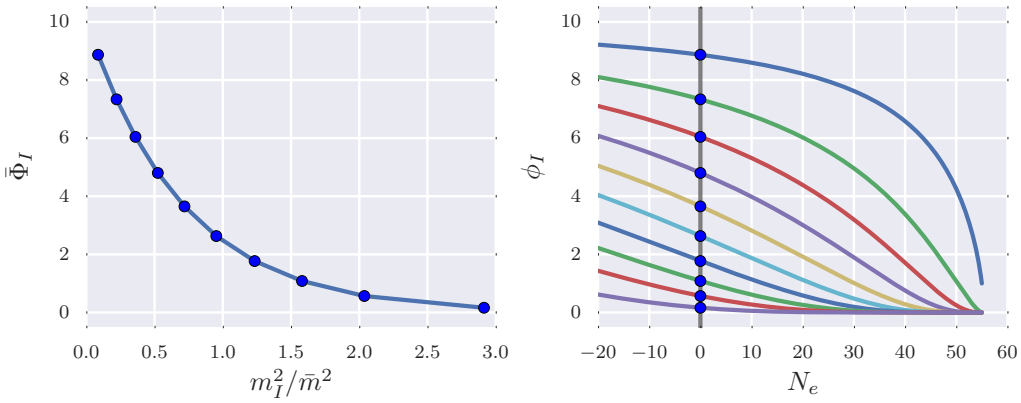

Figure 2.2: (*Left*) The masses m_I for each of the 10 fields in Eq. (2.62), drawn from the distribution (2.63) with $\bar{m}^2 = 4.3 \times 10^{-11}$, compared to the corresponding step positions $\bar{\Phi}_I$ for that field, which is positioned so that the pivot scale $k_* = 0.002\,\mathrm{Mpc}^{-1}$ leaves the horizon at $\bar{\Phi}_I$, given the initial conditions $\phi_{I,0} = 10$. (*Right*) The field trajectories (*colored lines*), with the same initial condition, as a function of e-folding N_e, with k_* (*vertical line*) leaving the horizon 55 e-folds before the end of inflation. The step positions $\bar{\Phi}_I$ are marked in blue and N_e has been renormalized so that $k_* = aH$ at $N_e = 0$.

step are set to $c_I = 10^{-3}$ and $d_I = 10^{-2}$ respectively, and the masses m_I relative to the fiducial mass to $\bar{m}^2 = 4.30 \times 10^{-11}$, which in the single-field limit yields A_s at the best-fit value from the *Planck TT* data. Following Ref. [89], we choose the masses m_I according to the Marčenko-Pastur distribution

$$P(m_I^2) = \frac{1}{2\pi m_I^2\, \bar{m}^2 \beta} \sqrt{(\beta_+ - m_I^2)\,(m_I^2 - \beta_-)}, \tag{2.63}$$

where

$$\beta_\pm = \bar{m}^2 \left(1 \pm \sqrt{\beta}\right)^2 \tag{2.64}$$

with $\beta = 1/2$. This distribution of masses is derived in Ref. [89], and has also been used in Refs. [93, 101, 102] and Chapter 5.

We set the step positions $\bar{\Phi}_I$ for each field at the field-space point where

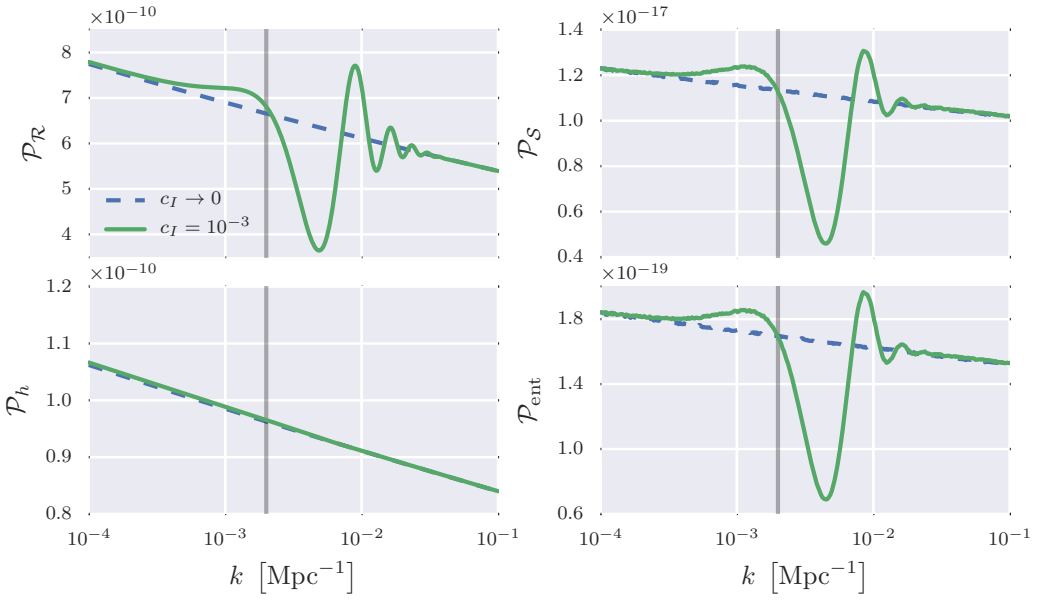

Figure 2.3: Features in the power spectra due to the step (2.62), which is positioned so that it affects the power spectra around the pivot scale $k_* = 0.002$ Mpc^{-1} (*gray*). We compare (*dashed, blue*) the no-step case with $c_I = 0$, to (*solid, green*) the case with $c_I = 10^{-3}$. While there are oscillations in the adiabatic $\mathcal{P}_\mathcal{R}$, isocurvature $\mathcal{P}_\mathcal{S}$, and entropic $\mathcal{P}_{\rm ent}$ spectra, there is little variation in the tensor spectrum $\mathcal{P}_h$.

the pivot scale $k_* = 0.002$ Mpc^{-1} leaves the horizon at $N_* = 55$ e-folds before the end of inflation in the no-step limit, $c_I \to 0$. Since the fields have identical initial conditions, the $\bar{\Phi}_I$ are functions only of the masses, so we plot the step positions versus the m_I in Fig. 2.2. We also present the field-space trajectories according to Eq. (2.5) for the last 75 e-folds of inflation with these parameters. The heavier fields relax more quickly toward their minimum at $\phi_I = 0$ and the lighter fields have a larger value at horizon crossing. Since $c_I = 10^{-3}$, the step is not obviously visible at the level of the background trajectory without zooming in significantly.

However, Fig. 2.3 shows the substantial effect on the power spectra due

to the steps. We see oscillatory behavior in the adiabatic, isocurvature, and entropic power spectra, but almost no change in the tensor spectrum. Furthermore, we can see clearly that $\mathcal{P}_{\mathcal{S}}$ and $\mathcal{P}_{\rm ent}$ exhibit a nearly identical feature, simply scaled by a factor of roughly 65. These features in the isocurvature spectrum may lead to interesting effects during reheating or the subsequent evolution of the post-inflation universe.

2.7 Conclusion

We present the Fortran 95/2000 code MultiModeCode, designed to maximize computational efficiency when numerically exploring a broad range of multifield inflation models. The code also provides Monte Carlo sampling of prior probabilities for inflationary model parameters and initial conditions, enabling automated model exploration and the computation of probability distributions for observables. The mode equation method has a broad range of applicability, but the computational cost scales with the number of fields as $\mathcal{O}(N_f^2)$. For models with sum-separable potentials, we have also implemented a slow-roll δN calculation, which only requires solving the background equations of motion once in order to obtain the full power spectrum as well as higher order statistics. This drastically improves computation time, since the background equations of motion are only $\mathcal{O}(N_f)$.

Here, we demonstrated its use with an N_f-flation model with a step. We find that a feature in the inflationary potential not only results in a feature in both the adiabatic power spectrum as a function of scale, $\mathcal{P}_{\mathcal{R}}(k)$, as well as the isocurvature spectra $\mathcal{P}_{\mathcal{S}}$, $\mathcal{P}_{\rm ent}$, and $\mathcal{P}_{\rm Pnad}$, with possible implications for the dynamics of many-field preheating scenarios. Further, we see numerical evidence that the isocurvature spectrum $\mathcal{P}_{\mathcal{S}}$ is a simple rescaling of the entropic

spectrum $\mathcal{P}_{\rm ent}$, indicating that the projection of the mode power spectrum onto the isocurvature directions is related to a quantity that sources a change in $\mathcal{R}$ on super-horizon scales.

MultiModeCode complements codes that currently exist to numerically compute the inflationary power spectra [23, 25, 32–34, 38–41, 103, 104]. The theoretical basis of the method is outlined in Section 4.4. The ability of MultiModeCode to solve numerically challenging problems, such as the step-potential in §2.6.2, and to provide large samples of many-field inflationary models adds significantly to the early universe cosmologist's toolkit for exploring and understanding realistic inflation models.

PART III

Sensitivity to Initial Conditions

Chapter 3

The Homogeneous Initial Conditions Problem

This chapter is adapted from:

R. Easther and L. C. Price

Initial conditions and sampling for multifield inflation

JCAP 1307 (2013) 027, [105]

3.1 Abstract

We investigate the initial conditions problem for multifield inflation. In these scenarios the pre-inflationary dynamics can be chaotic, increasing the sensitivity of the onset of inflation to the initial data even in the homogeneous limit. To analyze physically equivalent scenarios we compare initial conditions at fixed energy. This ensures that each trajectory is counted once and only once, since the energy density decreases monotonically. We present a full analysis of hybrid inflation that reveals a greater degree of long range order in the set of "successful" initial conditions than was previously apparent. In addition, we explore the effective smoothing scale for the fractal set of successful initial conditions induced by the finite duration of the pre-inflationary phase. The role of the prior information used to specify the initial data is discussed in

terms of Bayesian sampling.

3.2 Introduction

The standard hot big bang is synonymous with the Friedmann-Lemaître-Robertson-Walker (FLRW) metric. This model imposes maximally symmetric initial conditions on the metric and the mass-energy distribution, as specified on an arbitrary initial spatial hypersurface. These initial conditions acausally correlate spacelike-separated regions and require further fine-tuning for the Universe to be spatially flat at late times, leading to the well-known horizon and flatness problems. Famously, these problems are resolved by inflation [1–4], which grafts a phase of accelerated expansion onto the very early universe, setting the stage for the standard cosmology. During inflation the comoving Hubble volume contracts and the visible universe is driven toward the spatially flat FLRW universe.

Given that inflation attempts to explain the otherwise *ad hoc* initial conditions of the standard hot big bang, a viable inflationary mechanism must itself be free of tunings. Tunings can appear as technically unnatural parameter values in the inflaton sector or the need for a special pre-inflationary field configuration: the latter question is the focus of this chapter. Inflationary models with unnatural initial conditions are at best incomplete and, at worst, not viable as descriptions of the early universe. Moreover, the level of tuning required to ensure the onset of inflation can differ substantially between scenarios with largely degenerate observational predictions, providing a possible mechanism for discriminating between them.

The initial conditions problem arises even in the purely homogeneous limit. For instance, chaotic inflation [106] begins for a large range of initial field val-

Set	Description
$\mathcal{I}$	Initial conditions surface, however defined
$\mathcal{Z}$	Set of initial conditions with zero velocity
$\mathcal{C}_E$	Set of initial conditions with equal energy E
$\mathcal{S}_E$	Successfully inflating subset of $\mathcal{C}_E$
$\mathcal{F}_E$	Non-inflating subset of $\mathcal{C}_E$
$\mathcal{B}_E$	Boundary between $\mathcal{S}_E$ and $\mathcal{F}_E$

Table 3.1: Subsets of phase space: notation.

ues, but new inflation with the Coleman-Weinberg potential [3, 4] requires a special initial state. Inflationary models with multiple scalar degrees of freedom introduce a further level of complexity. With two or more fields the homogeneous dynamics are potentially chaotic, as first pointed out in Ref. [21] and also discussed by Refs [22,107]. Chaos is synonymous with sensitive dependence on initial conditions, rendering multifield models qualitatively different from their single field counterparts. Multifield scenarios are widely studied and more natural in many settings. In particular, string theoretic inflationary scenarios often possess many scalar degrees of freedom. Further, even if a model has an effective single-field description once inflation is underway, the pre-inflationary phase may contain many interacting fields. Several analyses of the initial conditions problem for multifield inflation exist [22,107–113] and we return to this question here.

We need to sample the "initial conditions space" $\mathcal{I}$ for these scenarios, determining the overall fraction that inflates and the topology of the inflationary region within this space. A homogeneous, spatially flat universe containing

N scalar fields ϕ_i with arbitrary interactions has $2N$ independent degrees of freedom since the scale factor can be eliminated by the 0-0 Einstein equation. The solutions to the equations of motion — called trajectories or orbits — are non-intersecting curves that fill the $2N$–dimensional phase space. Yet, the initial field values and velocities are not independent or identically distributed (iid) random variables as different points in $\mathcal{I}$ are correlated by the solutions to the field-equations, *i.e.*, many points belong to the same trajectory. (See Table 3.1 for a summary of our notation.)

The phase space is foliated by surfaces of equal energy, $\mathcal{C}_E$. The energy density $\rho = E^4$ of FLRW universes is monotonic, decreasing in a homogeneous universe as

$$\dot{\rho}(t) = -3H \sum_{i=1}^{N} \dot{\phi}_i^2, \tag{3.1}$$

where the Hubble parameter $H \propto E^2$ and overdots denote derivatives with respect to coordinate time t. For a specific energy E, orbits intersect $\mathcal{C}_E$ once and only once, identifying each point on $\mathcal{C}_E$ with a unique solution to the equations of motion. To build a well-defined sample of trajectories we choose initial conditions from the constraint surface $\mathcal{C}_E$.

Many previous treatments of the multifield initial conditions problem [108–112] have been based on $\mathcal{Z}$, the N–dimensional subset of $\mathcal{I}$ on which all velocities vanish simultaneously. Although the set of inflationary trajectories intersecting $\mathcal{Z}$ is easier to sample than $\mathcal{C}_E$, orbits for which all velocities vanish at the same instant are not generic, given the finite duration of the pre-inflationary era. Many orbits thus never intersect $\mathcal{Z}$, while in principle others may intersect it multiple times, correlating apparently distinct points — issues that cannot arise when sampling from $\mathcal{C}_E$. By contrast, Ref. [22] samples the full phase space $\mathcal{I}$ and also varies the parameters in the potential itself, effectively marginalizing over the energy scale E. The current chapter is the

first analysis of the initial conditions problem for multifield inflation that does not either (a) study a lower-dimensional surface in the initial conditions space (however defined) or (b) sample the entirety of $\mathcal{I}$, disregarding the fact that different points belong to the same solution of the field equations.[1]

Any description of the primordial universe breaks down above some energy scale, and this scale defines the appropriate initial conditions hypersurface $\mathcal{C}_E$ for a well-specified model.[2] This energy will be associated with some scale in the particle physics sector, such as the characteristic size of extra dimensions, the string scale, next-to-leading order corrections to Einstein gravity, or ultimately its breakdown at the Planck scale. Points on $\mathcal{C}_E$ are thus physically commensurate, whereas points in $\mathcal{I}$ span several orders of magnitude in energy. Qualitatively, we will also find that the set of successfully inflating points has a simpler structure and more obvious long range order when chosen from $\mathcal{C}_E$ rather than $\mathcal{Z}$, allowing us to better understand the underlying cosmological dynamics.

Beyond the choice of initial conditions surface, we must also specify the prior probability distributions (in Bayesian terms) for the initial field values and velocities. If ω is a probability distribution that weights an initial condition $\mathbf{x}_0$ according to how well its final state matches the observed universe, then the expected value of ω over initial conditions $\mathbf{x}_0 \in \mathcal{C}_E$ is

$$\langle \omega(\mathcal{C}_E) \rangle = \int_{\mathcal{C}_E} \omega(\mathbf{x}_0) P_E(\mathbf{x}_0) d^N x_0 \approx \frac{1}{n} \sum_{i=1}^{n} \left\{ \omega(\mathbf{x}_0^{(i)}) \right\}_{\mathbf{x}_0^{(i)} \in C_E}, \tag{3.2}$$

where P_E is the prior probability distribution for initial conditions on the constraint surface $\mathcal{C}_E$ and the sum is evaluated at n points sampled from C_E. The

[1] Tetradis [110] presents a single equal energy slice, although a degree of freedom was removed by requiring the velocities to be equal, similar to the projections we introduce for convenience in Figs 3.3–3.5.

[2] If the potential has one or more local minima where $V_\Lambda > 0$, choosing $E^4 < V_\Lambda$ will necessarily exclude all trajectories which evolve toward these minima.

prior in Eq. (3.2) acts as the probability density function for initial conditions on the space of FLRW universes. The form of P_E is only weakly constrained by fundamental considerations. The freedom to choose P_E is analogous to the measure problem in the multiverse [114–118], albeit restricted to the subspace of homogeneous FLRW universes. In many previous works the prior is often not directly discussed, and thus implicitly defined as a uniform distribution on the initial conditions. We consider several possible choices of prior (all of which are uninformative) and vary the energy of the surfaces $\mathcal{C}_E$. We find that the choice of prior significantly alters the fraction of trajectories that lead to inflation, potentially distorting conclusions about the extent to which a given inflationary model requires fine-tuned initial conditions.

In what follows we work with a widely studied two-field model: canonical hybrid or false-vacuum inflation [81, 82, 119]. We relate the initial conditions problem to that of determining the (fractal) topology and the geometry of the subset of points $\mathcal{S}_E \subset \mathcal{C}_E$ that successfully inflate, since this is independent of the choice of prior. Like Refs [22,112] we see that $\mathcal{S}_E$ has a fractal topology due to the presence of chaos in the underlying dynamical system, demonstrating that hybrid inflation has regions of phase space where orbits are highly sensitive to their initial conditions and confirming the results of Ref. [21]. Hybrid inflation is associated with a blue power spectrum[3] at odds with recent astrophysical data [17, 122–125]. However, our primary focus is not hybrid inflation itself, but developing tools that can be used to understand the initial conditions problems in generic models of multifield inflation. We use this model because (a) it is the prototypical multifield model with chaotic dynamics and a narrowly defined inflationary attractor; (b) we are primarily interested in the onset of inflation; and (c) to make contact with previous work.

[3] Although see Refs [120, 121].

The pre-inflationary universe is dissipative, so the fractal structure must have a nontrivial scale dependence: there is necessarily a minimum scale below which two nearby trajectories will remain correlated until they reach either the inflationary attractor or a minimum of the potential, smoothing $\mathcal{S}_E$ below this scale. Conversely, while we assume classical homogeneity, quantum fluctuations prevent the universe from being *perfectly* smooth. If $\mathcal{S}_E$ has structure on scales smaller than a typical fluctuation we cannot sensibly define the homogeneous limit for this system. Consequently, we propose a sampling technique that identifies regions where $\mathcal{S}_E$ has structure below this minimum scale.

This chapter is arranged as follows: in Section 3.3 we review hybrid inflation and discuss its dynamics. In Section 4.5 we describe our numerical methods, characterize the properties of the set of inflationary trajectories with different energies and priors P_E, and investigate the fractal dimension of $\mathcal{S}_E$. In Section 4.6 we discuss the implication of our results and identify future lines of enquiry.

3.3 Inflationary dynamics

For simplicity we consider two homogeneous scalar fields, ψ and the inflaton ϕ, interacting through a potential $V(\psi,\phi)$ in a homogeneous FLRW universe. The equations of motion are

$$\ddot{\phi} + 3H\dot{\phi} + \frac{\partial V}{\partial \phi} = 0 \qquad \text{and} \qquad \ddot{\psi} + 3H\dot{\psi} + \frac{\partial V}{\partial \psi} = 0, \tag{3.3}$$

and the Hubble parameter H can be eliminated by the 0-0 Einstein equation

$$H^2 = \frac{8\pi}{3M_{\rm Pl}^2}\left[\frac{1}{2}\dot{\phi}^2 + \frac{1}{2}\dot{\psi}^2 + V(\psi,\phi)\right], \tag{3.4}$$

where $M_{\rm Pl}$ is the Planck mass. Following Refs [21, 22, 107–112] we consider hybrid inflation [81, 82, 119] with the potential

$$V(\psi,\phi) = \Lambda^4\left[\left(1-\frac{\psi^2}{M^2}\right)^2 + \frac{\phi^2}{\mu^2} + \frac{\phi^2\psi^2}{\nu^4}\right], \tag{3.5}$$

with real parameters Λ, M, μ, and ν. Inflation occurs in the "inflationary valley" with $\psi \approx 0$ and $|\phi| > \phi_c$, where $\phi_c = \sqrt{2}\,\nu^2/M$ is the critical point at which the effective mass of ψ becomes complex and inflation comes to an end. The potential is symmetric under $\phi \to -\phi$ and $\psi \to -\psi$, with two equivalent valleys for $\phi > \phi_c$ and $\phi < -\phi_c$ and minima at $\{\psi,\phi\} = \{\pm M, 0\}$. Orbits will either enter one of the false-vacuum inflationary valleys or evolve directly toward one of the true vacua.

We set the amplitude A_s of the dimensionless power spectrum $\mathcal{P}_\mathcal{R}$ to be roughly compatible with the WMAP9 data [123, 124], which fixes the potential energy scale. This results in

$$A_s \approx \frac{1}{24\pi^2 M_{\rm Pl}^4}\left(\frac{V}{\epsilon_V}\right) = (2.43 \pm 0.08)\times 10^{-9}, \tag{3.6}$$

where $\epsilon_V = (M_{\rm Pl}^2/2)(V_{,\phi}/V)^2$ is the slow-roll parameter. Setting $M = .03\,M_{\rm Pl}$, $\mu = 500\,M_{\rm Pl}$, and $\nu = .015\,M_{\rm Pl}$ and assuming perturbations are generated when $\psi \approx 0$ and $\phi \approx \phi_c$, we derive $\Lambda \approx 6.8\times 10^{-6}\,M_{\rm Pl}$.[4] Lastly, Ref. [126] determined that quantum fluctuations dominate the classical field evolution in the inflationary valley when

$$\Lambda > \Lambda_q \equiv 4\pi\sqrt{3}M_{\rm Pl}^3\frac{\phi_c}{\mu^2}. \tag{3.7}$$

For our parameters $\Lambda_q = 9.6\times 10^{-4}\,M_{\rm Pl}$, so the classical equations are self-consistent.

[4] The super-Planckian value of μ is an artifact of this definition of the potential; the actual mass term is $m_\phi^2 = 2\Lambda^4/\mu^2 \approx 10^{-26}\,M_{\rm Pl}^2$, and safely sub-Planckian.

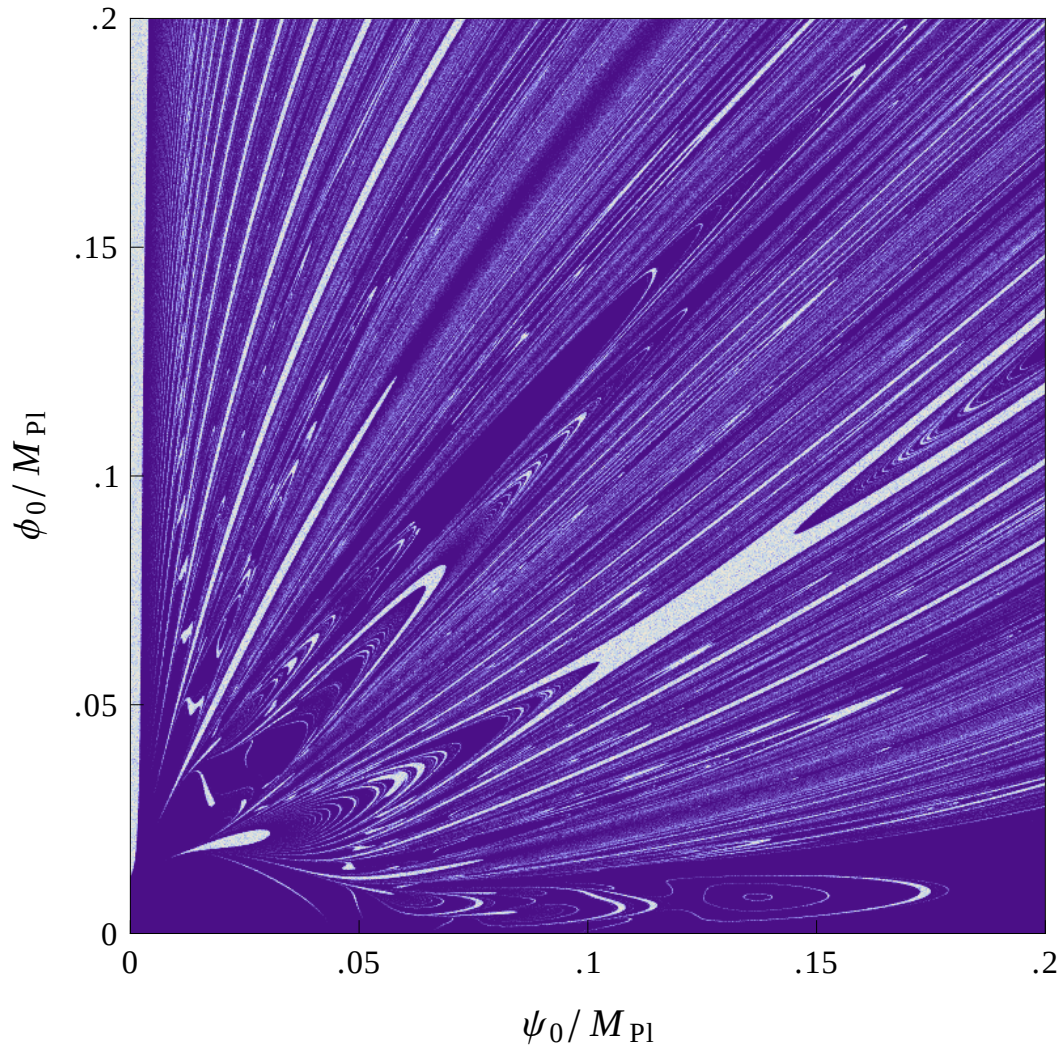

Figure 3.1: Distribution of successfully inflating initial conditions drawn from the zero-velocity slice $\mathcal{Z}$. White areas have the highest number of successful points; darker regions have the fewest. This plot matches Fig. (1) of Ref. [22], with M = $.03\,M_{\rm Pl}$, μ = $636\,M_{\rm Pl}$, and ν = $.0173\,M_{\rm Pl}$. The figures are similar (verifying our codes and algorithms) but are not expected to be identical, due to different binning procedures.

The inflationary valley is a small subset of the total phase space, which might suggest the model has a fine-tuning problem. References [108, 110, 111] considered sub-Planckian initial field values on the zero-velocity surface $\mathcal{Z}$, pessimistically concluding that — in the absence of effects that increase the friction experienced by the fields — only trajectories which start inside the inflationary valley yield 60 e-folds of inflation. By contrast, Ref. [109] was more optimistic, showing that a supergravity-inspired hybrid inflation model has a significant number of "successful" points outside the inflationary valley. With more exhaustive sampling of $\mathcal{Z}$, subsequent studies by Clesse, Ringeval, and Rocher [22, 112] extended this optimistic conclusion to the potential (4.4). They showed that successful initial conditions are distributed in an intricate series of patches and fine lines outside the inflationary valley, with a fractal boundary separating inflating and non-inflating initial conditions. The distribution of successfully inflating initial conditions on $\mathcal{Z}$, for a specific scenario from Ref. [22], is reproduced in Fig. 3.1. The fine-tuning problem may also be less serious if the initial field values are assumed to be super-Planckian or if the interaction term dominates [112, 127].

References [22, 120] also present a Markov Chain Monte Carlo (MCMC) sampling of all possible parameter choices and sub-Planckian field configurations, including those with initial velocities. The conclusion was that 60 e-folds of inflation is generic for the potential in Eq. (4.4) and fine-tuned initial conditions in the inflationary valley are not required. Although we have argued that sampling from any two-dimensional subspace, such as $\mathcal{Z}$, is of limited benefit, sampling the whole four-dimensional space $\mathcal{I}$ may not be strictly necessary, even though an MCMC technique marginalizes the unknown initial energy E. We instead choose to explore how fine-tuned the initial conditions must be when sampling from constraint surfaces $\mathcal{C}_E$ that incorporate the energy con-

straint Eq. (3.1).

3.4 Numerical results

3.4.1 Method

We numerically integrate Eqs (3.3)–(4.4) using a backward-difference formula implemented by the FCVODE package from the SUNDIALS computing suite [128]. We sample initial conditions from constraint surfaces $\mathcal{C}_E$ with constant energy density

$$\rho = \frac{1}{2}\dot{\psi}_0^2 + \frac{1}{2}\dot{\phi}_0^2 + V(\psi_0, \phi_0) = E^4, \tag{3.8}$$

where

$$E = 10^i \, M_{\rm Pl} \qquad \text{for} \qquad i \in \{-5, \ldots, 0\}. \tag{3.9}$$

The last 60 e-folds of inflation occur at $\{\psi, \phi\} \approx \{0, \phi_c\}$ with $E \sim 10^{-6}\, M_{\rm Pl}$. With $E = 10^0 M_{\rm Pl}$ we are at the limit of classical Einstein gravity; we only include this case to illustrate the underlying dynamical system.

We stop integrating when either (a) the orbit achieves more than 60 e-folds during inflation or (b) $\rho < \Lambda^4$ and the trajectory is trapped by the potential wells at $\{\psi, \phi\} = \{\pm M, 0\}$. Initial conditions which lead to 60 e-folds of inflation are "successful" and define the subset $\mathcal{S}_E$, while its complement — the "failed" points — comprise the subset $\mathcal{F}_E$.[5] The boundary between these sets, whose properties determine the extent to which they "mix," is denoted $\mathcal{B}_E$.

We select points randomly on the constraint surface as follows. We first draw ϕ_0 and ψ_0 from the uniform distribution over $0 \le \{\psi_0, \phi_0\} \le .2\, M_{\rm Pl}$, excluding any choices with $V(\phi_0, \psi_0) > E^4$. The symmetry of the potential (4.4)

[5] Again, additional constraints can be added, e.g. data matching for n_s, r, or other observables.

allows the restriction to positive field values, whereas the upper bound is set to be consistent with Ref. [22]. Given these initial field values, the kinetic energy is typically dominant unless $E \approx \Lambda \sim 10^{-6}\ M_{\rm Pl}$. We apportion the remaining energy by drawing one of $v_1 \in \{\dot{\phi}_0, \dot{\psi}_0\}$ from a uniform prior on the range

$$-\sqrt{2(E^4 - V_0)} \leq v_1 \leq \sqrt{2(E^4 - V_0)} \tag{3.10}$$

and giving the leftover energy to the other field velocity v_2 with the overall sign again chosen randomly. We maintain the symmetry between $\dot{\phi}_0$ and $\dot{\psi}_0$ by alternating the order in which these velocity terms are set.[6] This procedure implicitly defines the initial priors $P_{\rm orig}$ on the constraint surfaces $\mathcal{C}_E$.

To estimate the size of inhomogeneous fluctuations at the initial energy E, we note that $\delta\phi \sim H/2\pi$ and $H \sim E^2/M_{\rm Pl}$ for a massless field in de Sitter space. Similarly, the minimal variation in velocities is expected to be of order H^2 across a Hubble volume [126,129,130]. The fields ψ and ϕ are not massless and the pre-inflationary universe is not de Sitter, but we can use this relationship to put an approximate lower bound on the homogeneity of the primordial universe. In regions of $\mathcal{S}_E$ whose typical scale in any phase space dimension is less than

$$\Delta \equiv \{\delta\psi_0, \delta\phi_0, \delta\dot{\psi}_0, \delta\dot{\phi}_0\} = \frac{1}{2\pi}\{H, H, H^2, H^2\} \tag{3.11}$$

the homogeneous approximation breaks down and further analysis is invalid or ambiguous. If we smooth the universe on scales larger than the Hubble horizon, then Δ indicates a 1σ fluctuation from the fiducial initial value in phase space, if we assume a white noise spectrum. If a successfully inflating point is within Δ of an unsuccessful point, then there is significant ambiguity in

[6] This prior generates the high tails in the velocity distributions seen in Fig. 3.6. If the first velocity chosen is v_1, the second will be $v_2 = \pm\sqrt{2(E^4 - V_0) - v_1^2}$. Since v_1 is uniformly distributed, v_2 is a quadratic distribution, favoring higher values.

the final state due to this estimate of the initial inhomogeneity. Physically, in these regions we cannot self-consistently assume that the primordial universe is homogeneous.

We exclude these regions from $\mathcal{S}_E$ by sampling $\mathcal{C}_E$ in clusters. We first choose points from $\mathcal{C}_E$ and integrate Eqs (3.3)–(4.4). At each point that successfully inflates we randomly draw 100 points within Δ of that point.[7] If any of these new points do not inflate, we conclude that the original point was a "false" (or perhaps ambiguous) positive. Applying this simple stability check at various other points along the trajectory's evolution is straightforward, but computationally expensive. Furthermore, the largest fluctuations occur at the highest energies, so testing the initial energy surface captures the most relevant effects. Although this approach incorporates points lying near (but not actually on) our designated equal energy surface, we do not weight our conclusions by these secondary points.

This analysis does not address the inhomogeneous initial conditions problem; it simply limits the extent to which the initial conditions can be self-consistently fine-tuned in a homogeneous universe, given that the chaotic dynamics of the potential may cause closely correlated trajectories to diverge exponentially. Fig. 3.2 shows three solutions of Eqs (3.3)–(4.4), at $E = 10^{-5}\, M_{\rm Pl}$ with initial field values which differ by only $10^{-8} M_{\rm Pl}$. They eventually diverge, with each trajectory reaching a distinct end-state. If an inflation model has a fractal $\mathcal{S}_E$ or $\mathcal{B}_E$ that is distributed in a complex manner over $\mathcal{C}_E$, then almost all successfully inflating initial conditions may be within Δ of an initial condition which does not inflate.

[7] For the lowest values of E, $\left\{\delta\psi_0/\psi_{\rm max},\, \delta\phi_0/\phi_{\rm max},\, \delta\dot{\psi}_0/\dot{\psi}_{\rm max},\, \delta\dot{\phi}_0/\dot{\phi}_{\rm max}\right\} \sim 10^{-10}$, which is far below the resolution of our figures. We confirmed the accuracy of the FCVODE integrator in this domain by using an arbitrary precision integrator from Mathematica.

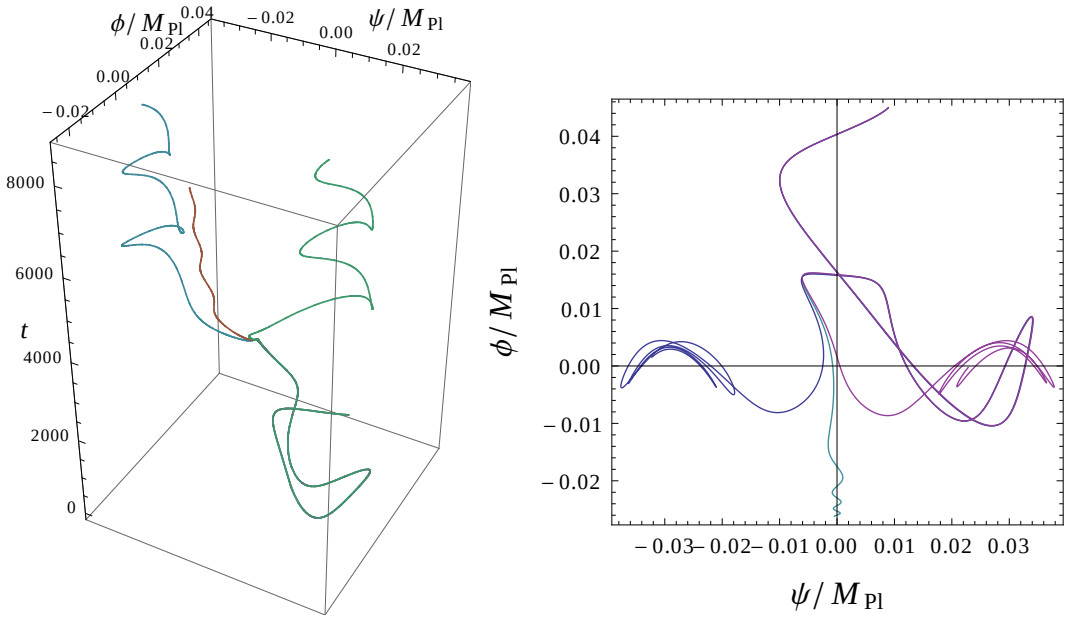

Figure 3.2: Parametric trajectory plots for three orbits at energy $E = 10^{-5}\,M_{\rm Pl}$ initially separated by $10^{-8}M_{\rm Pl}$ in the field values and $10^{-8}M_{\rm Pl}^2$ in the field velocities. These orbits are exponentially diverging, with each of the three trajectories branching at $t \approx 3600\,M_{\rm Pl}^{-1}$; one goes to each of the global minima at $\psi = \pm M$ and one inflates.

3.4.2 Successful inflationary trajectories

The fraction of successful points at any given energy E is summarized in Table 3.2, both including and excluding the "false positives." The highest probability for success is at higher energies. We should expect this since, given that the effective equation of state is not the same on all trajectories, orbits accumulate on the narrow inflationary attractor over time, leaving a larger flux of orbits through the attractor at lower energies. In comparison to a sample drawn from $\mathcal{C}_E$, an identical sample from a slice $\mathcal{C}_{E'}$ with $E > E'$ will not place as much weight on trajectories inside the inflationary attractor and we expect to see fewer successfully inflating initial conditions on the lower energy surface.

Figures 3.3 to 3.5 show two dimensional slices of $\mathcal{S}_E$ at different values

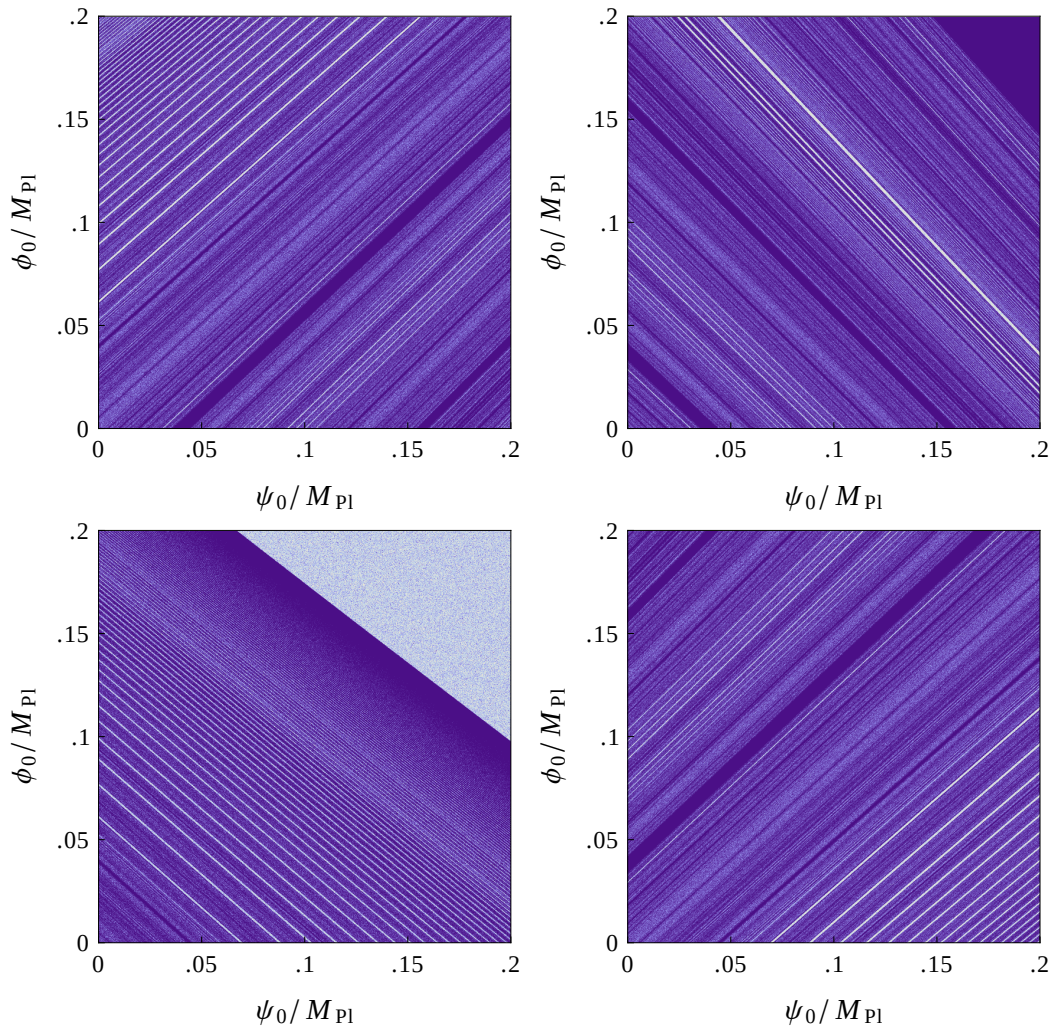

Figure 3.3: Two dimensional slicings of $\mathcal{C}_E$ for $E = 10^{-2}\, M_{\rm Pl}$, including the ambiguous, "false positive" points in $\mathcal{S}_E$. Parameters are $\Lambda = 6.8 \times 10^{-6}\, M_{\rm Pl}$, $M = .03\, M_{\rm Pl}$, $\mu = 500\, M_{\rm Pl}$, and $\nu = .015\, M_{\rm Pl}$. The light and dark areas are regions that have a higher and lower density of points in $\mathcal{S}_E$, respectively. The results have been binned over a 1000×1000 grid. All velocities are of equal magnitude, however the left column has $\dot{\phi} > 0$, the right column is at $\dot{\phi} < 0$, the top row has $\dot{\psi} > 0$, and the bottom row has $\dot{\psi} < 0$.

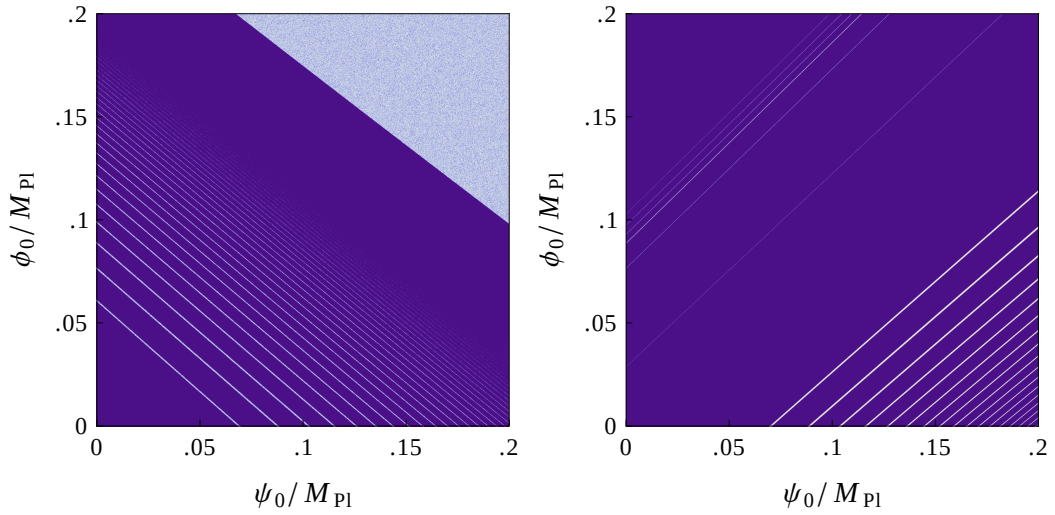

Figure 3.4: Two dimensional slicings of $\mathcal{C}_E$ for $E = 10^{-2}\,M_{\rm Pl}$, excluding any ambiguous or "false" positives from the set of successfully inflating initial conditions, $\mathcal{S}_E$. All velocities are of equal magnitude; the left panel has $\dot{\psi}_0 < 0$ and $\dot{\phi}_0 > 0$; and the right panel has $\{\dot{\psi}_0, \dot{\phi}_0\} < 0$.

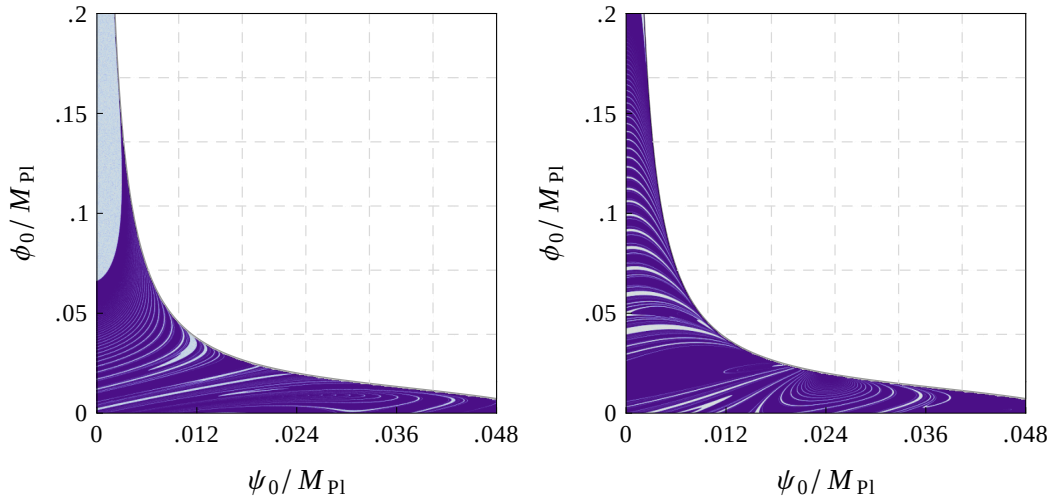

Figure 3.5: Two dimensional slicings of $\mathcal{C}_E$ for $E = 10^{-5}\,M_{\rm Pl}$, where the checked background has $V(\psi_0, \phi_0) > E^4$ and has not been sampled. All velocities are of equal magnitude; the left panel has $\{\dot{\psi}_0, \dot{\phi}_0\} > 0$ and the right panel has $\{\dot{\psi}_0, \dot{\phi}_0\} < 0$.

E [$M_{\rm Pl}$]	$n_{\rm succ}$ [M]	$n_{\rm total}$ [M]	$n_{\rm false}$ [k]	$f_{\rm true}$	$f_{\rm total}$
10^{0}	0.00	2.01	1000.0	0.000	0.498
10^{-1}	1.00	2.24	72.7	0.447	0.479
10^{-2}	1.00	2.57	114.6	0.389	0.434
10^{-3}	1.00	3.34	105.9	0.300	0.331
10^{-4}	1.00	4.89	30.4	0.205	0.211
† 10^{-5}	1.00	4.45	0.012	0.225	0.225

Table 3.2: Total fraction of successfully inflating points sampled from priors $P_{\rm orig}$ on the equal energy slices $\mathcal{C}_E$ — both excluding ($f_{\rm true}$) and including ($f_{\rm total}$) false positives from $\mathcal{S}_E$. Also shown are the number of successful points $n_{\rm succ}$, the number of false positives $n_{\rm false}$, and the combined number of fail points, false positives, and successful points $n_{\rm total}$. The numbers $n_{\rm succ}$ and $n_{\rm total}$ are measured in millions [M] of points, $n_{\rm false}$ is measured in thousands [k] of points, and the energy E is in units of the Planck mass $M_{\rm Pl}$. (†) The sampling procedure deviates from an "equal-area" sample as $E \to \Lambda$.

of E. We bin $\mathcal{S}_E$ on a 1000×1000 grid: white regions are those with the highest number of successful points and the darkest regions have the fewest. We accumulated 2.5 million successful points on each slice and see minor stochastic variation in the number of points per bin. Figures 3.3, 3.4 ($E = 10^{-2}\, M_{\rm Pl}$), and 3.5 ($E = 10^{-5}\, M_{\rm Pl}$) show two-dimensional slices of $\mathcal{C}_E$ on which the initial velocities have equal magnitude $|\dot{\phi}_0| = |\dot{\psi}_0|$. Looking at Figs 3.3 through 3.5 we can see areas where $\mathcal{S}_E$ and $\mathcal{F}_E$ mix together, forming an intricate substructure similar to that seen in Refs [22, 112]. In Fig. 3.4 we also see contiguous regions and thick bands which reliably inflate and survive the subtraction of the false positives from $\mathcal{S}_E$. Qualitatively, $\mathcal{S}_E$ exhibits considerable long range order

when compared to Fig. 3.1. At higher energy, contiguous regions in $\mathcal{S}_E$ occupy a larger portion of $\mathcal{C}_E$, which can be seen clearly in Figs 3.3 and 3.4. The transition from Figs 3.3 to 3.5 shows how the geometry of $\mathcal{S}_E$ changes with E.

Figures 3.3 to 3.5 are projections of three dimensional regions and suppress information about the field velocities of the successful initial configurations. Intuitively, the points most likely to inflate (for given ϕ_0 and ψ_0) would be those which had a large $|\dot{\phi}_0|$ and small $|\dot{\psi}_0|$. These points are essentially "launched" up the inflationary valley, while the slope of the potential focuses them toward smaller values of ψ. To show this dependence on the initial values $\dot{\phi}_0$ and $\dot{\psi}_0$, Fig. 3.6 shows histograms of these values sampled from the whole of $\mathcal{C}_E$. The fraction of sampled points in $\mathcal{S}_E$ as a function of initial velocity confirms our intuition: most successful points have larger $|\dot{\phi}_0|$ and smaller $|\dot{\psi}_0|$. Points for which $\dot{\phi}_0 \approx 0$ are particularly disfavored, further suggesting that the zero-velocity slice $\mathcal{Z}$ is unrepresentative of typical inflationary trajectories. We can also see the impact of the "false positives" in these plots: these are more frequent at high energies and in the limiting case $E = M_{\rm Pl}$ all naïvely-inflating initial conditions are false positives, since Δ encompasses the whole of $\mathcal{I}$ in this limit.

With sub-Planckian initial field values the kinetic energy dominates the potential energy for $E \gg \Lambda$. Thus, even if a trajectory starts inside the inflationary valley, its velocity is such that it is unlikely to remain there. For example, when $E = 10^{-2}\, M_{\rm Pl}$ the slices of $\mathcal{S}_E$ in Figs 3.3 and 3.4 show no special preference for points within the valley. In contrast, with $E = 10^{-5}\, M_{\rm Pl} \sim 10\Lambda$ the valley is clearly distinguishable, as shown in Fig. 3.5, but only when the initial velocity of ϕ is directed "uphill," i.e. with $\dot{\phi}_0 \geq 0$. Conversely, each slice contains many successful points that lie outside the inflationary valley.

In Fig. 3.7 we project specific representative solutions of Eqs (3.3)–(4.4)

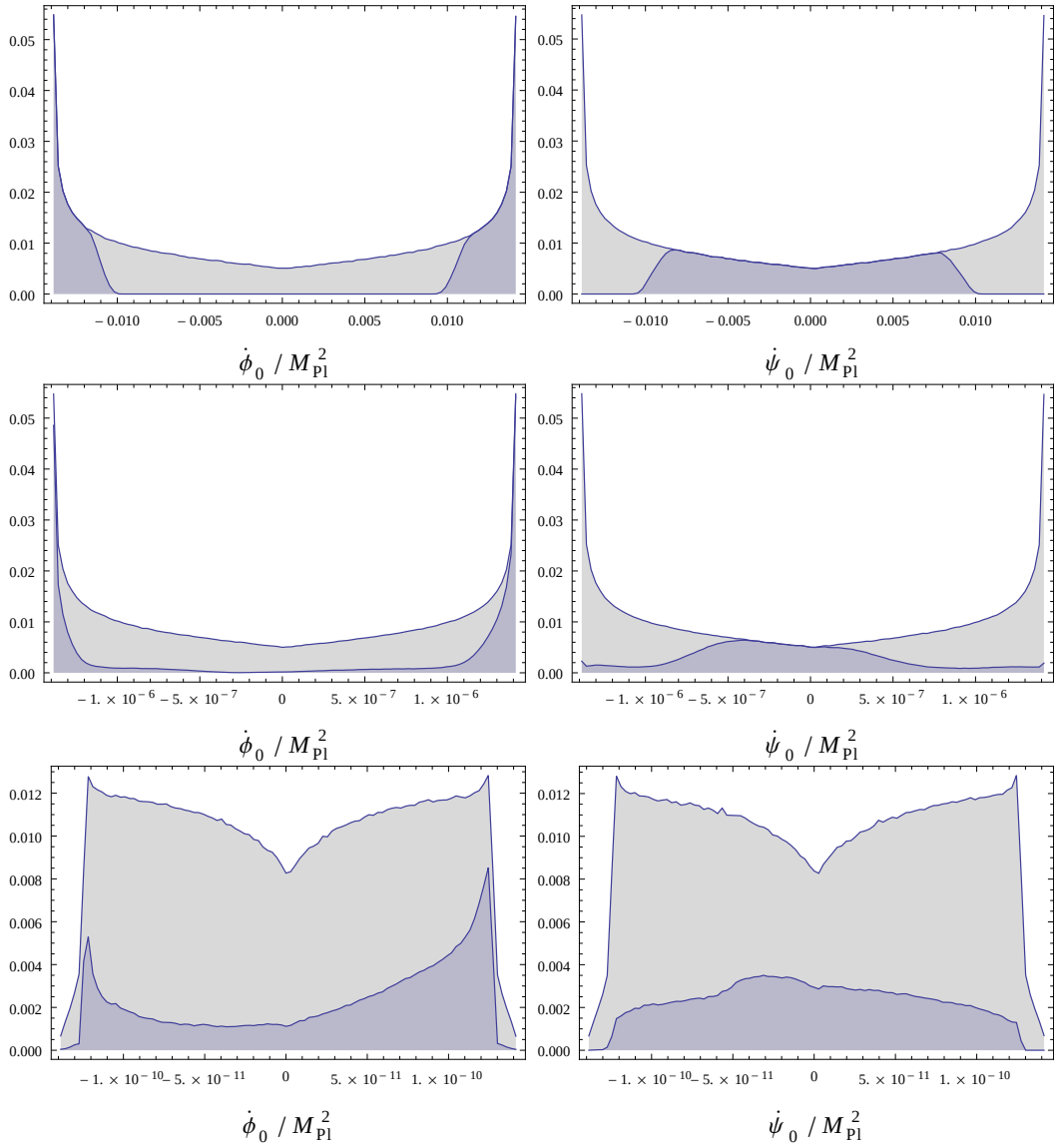

Figure 3.6: Histograms of $\dot{\phi}_0$ (left column) and $\dot{\psi}_0$ (right column) drawn from equal energy surfaces $\mathcal{C}_E$ with priors $P_{\rm orig}$. The rows have energy $10^{-1}\, M_{\rm Pl}$ (top), $10^{-3}\, M_{\rm Pl}$ (middle), and $10^{-5}\, M_{\rm Pl}$ (bottom). The gray background is the total sample from $\mathcal{C}_E$ and the blue foreground is the successful subset $\mathcal{S}_E$. At $E = M_{\rm Pl}$ (not displayed), there are false positives only.

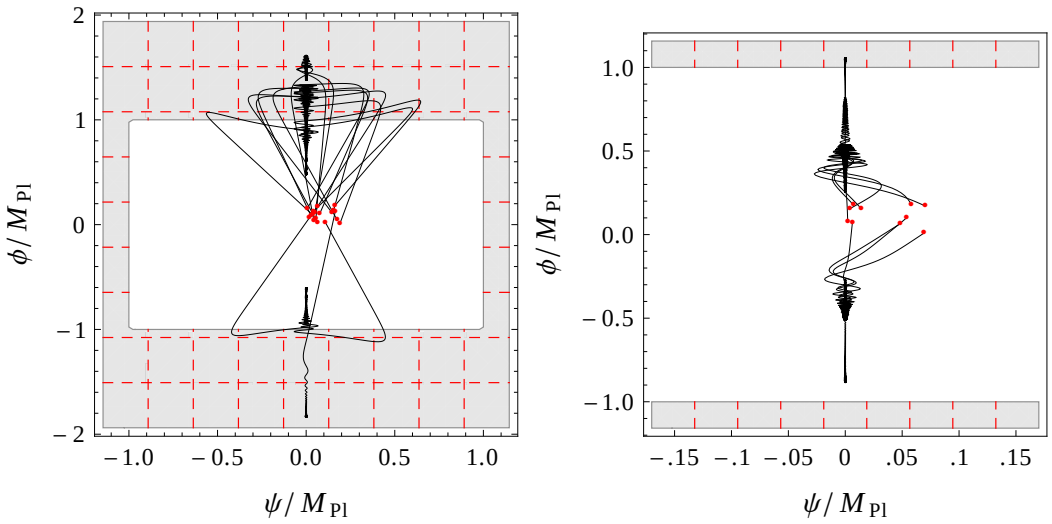

Figure 3.7: Successfully inflating trajectories projected onto the $\{\psi, \phi\}$ plane, with initial conditions $\{\psi_0, \phi_0\}$ marked in red. The left panel is at energy $E = 10^{-2}\, M_{\rm Pl}$ and the right panel is at energy $E = 10^{-4}\, M_{\rm Pl}$. The gray, checked region is where the magnitude of the field values exceeds $M_{\rm Pl}$.

onto the $\{\psi, \phi\}$ plane for initial conditions with energies $E = 10^{-2}\, M_{\rm Pl}$ and $E = 10^{-4}\, M_{\rm Pl}$. Trajectories which unambiguously inflate show little topological mixing and are all reflected off of the maximum of the potential $V_{\rm max} = V|_{\psi=\phi}$ toward the inflationary valley. For $E \gtrsim 10^{-3} M_{\rm Pl}$, most trajectories contain regions in which the field values are super-Planckian. We do not exclude these trajectories, but we could easily add this as a separate requirement for a viable inflationary scenario, in which case almost no successful inflationary trajectories exist at these energies.

To quantify the sensitive dependence on initial conditions independently of our sampling procedure, we use the box-counting method to estimate the fractal dimension of both $\mathcal{S}_E$ and its boundary $\mathcal{B}_E$, including the "false" positives [131]. We first cover each set $\mathcal{S}_E$ and $\mathcal{B}_E$ with progressively smaller four-dimensional boxes of size δ, then count the number $N(\delta)$ of δ-sized boxes

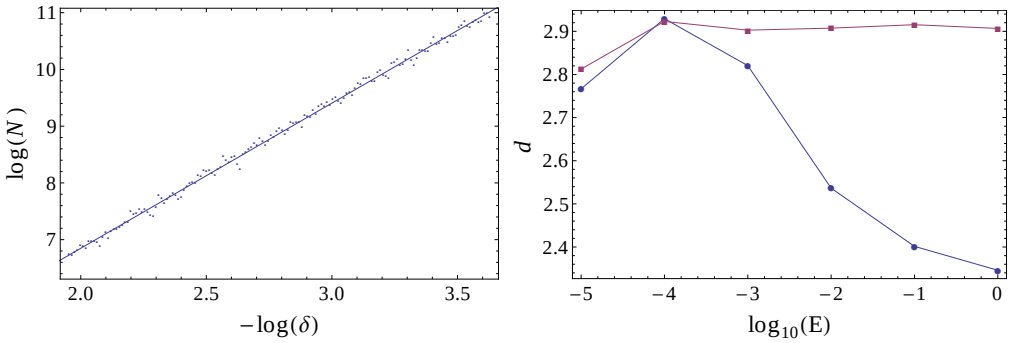

Figure 3.8: The left panel shows the box counting of $\mathcal{B}_E$ for $E = 10^{-2}\, M_{\rm Pl}$. The slope of the best-fit line $d = 2.558$ is the box counting dimension. The right panel is the box counting dimension d versus the energy E for sets $\mathcal{S}_E$ and $\mathcal{B}_E$ at the energies in Eq. (3.9). The red line with boxes indicates $\mathcal{S}_E$ and the blue line with circles is $\mathcal{B}_E$.

in each covering. The box-counting dimension

$$d = \lim_{\delta \to 0} \frac{\log(N(\delta))}{\log(1/\delta)} \tag{3.12}$$

is estimated by the slope of the line fitted to the linear portion of the curve $\log(N)$ as a function of $\log(1/\delta)$. To compute the dimension of $\mathcal{B}_E$ we count boxes that contain elements of both $\mathcal{S}_E$ and $\mathcal{F}_E$. Figure 3.8 shows both a typical fit (for $\mathcal{B}_E$ with $E = 10^{-2}\, M_{\rm Pl}$) and the computed values of d for $\mathcal{S}_E$ and $\mathcal{B}_E$. The result is sensitive to the detailed fitting procedure, which we trained by testing the algorithm on sets with known dimension, such as Cantor dust. Furthermore, the estimate for d depends both on the non-trivial distribution of $\mathcal{S}_E$ over $\mathcal{C}_E$ and the resolution of sampled points, which is a function of the initial energy and sampling prior. The reported values of d should be interpreted as an upper bound to the related Hausdorff dimension [131] that improves with increasing E, where the set $\mathcal{S}_E$ has higher long-range order. The Hausdorff dimension and the box-counting dimension coincide for cases where the fractal is exactly self-similar.

The regions considered here are multifractal, in that the dimension of $\mathcal{S}_E$

will be a function of both position in $\mathcal{I}$ and the overall scale. The first is easy to see: each surface $\mathcal{C}_E$ contains regions in which essentially all points inflate (in these regions $d \approx 3$) and regions that are approximately isolated points (with $d < 3$). Consequently, the computed value of d is effectively a weighted average of at least two different regions, which explains why the dimension of $\mathcal{S}_E$ is close to 3 but still measurably non-integer. Secondly, at very small scales $\mathcal{S}_E$ must consist of smooth contiguous regions and on these scales we expect $d \to 3$. These regions exist in spite of the chaotic dynamics due to the dissipative terms in Eqs (3.3)–(4.4) and put a lower limit on the mixing scale.

3.4.3 The role of the prior

It is well-known [114–118, 127, 132] that probability measures on different hypersurfaces result in different conclusions regarding the likelihood of inflation; we explore here how this relates to the choice of sampling prior. Although surfaces with different energies (as well as different initial conditions surfaces, such as a slice of constant comoving time) are homeomorphic to $\mathcal{C}_E$ and, by definition, have the same topology, the prior on $\mathcal{C}_E$ is not a topological property and is not preserved under either homeomorphism or a change of variables.[8] Each initial condition surface then has a different prior and different likelihood for inflation, even given the same sampling technique.

In Table 3.3 we compare different uninformative priors, defined implicitly through four sampling algorithms, on surfaces $\mathcal{C}_E$ at the energies in Eq. (3.9). Since the kinetic energy is initially dominant for the energies and ranges we consider, we leave the selection method for $\{\psi_0, \phi_0\}$ the same as in Section 3.4.1, but vary the way we set the velocities $v \in \{\dot{\psi}_0, \dot{\phi}_0\}$. The original prior $P_{\rm orig}$

[8] A homeomorphism is provided by time-translation along the integral curves of the equations of motion. Note that $\mathcal{Z}$, being of a lower dimension, is not homeomorphic to $\mathcal{C}_E$.

—	$P_{\rm orig}$		$P_{\rm square}$		$P_{\dot\phi}$		$P_{\dot\psi}$	
E $[M_{\rm Pl}]$	$f_{\rm true}$	$f_{\rm total}$	$f_{\rm true}$	$f_{\rm total}$	$f_{\rm true}$	$f_{\rm total}$	$f_{\rm true}$	$f_{\rm total}$
10^{0}	0.000	0.498	0.000	0.497	0.000	0.704	0.000	0.294
10^{-1}	0.447	0.479	0.426	0.471	0.651	0.681	0.243	0.276
10^{-2}	0.389	0.434	0.347	0.408	0.582	0.624	0.196	0.242
10^{-3}	0.300	0.331	0.245	0.285	0.438	0.469	0.162	0.194
10^{-4}	0.205	0.211	0.188	0.195	0.247	0.253	0.163	0.169
10^{-5}	0.225	0.225	0.215	0.215	0.265	0.265	0.183	0.183

Table 3.3: Fraction f of sampled points from $\mathcal{C}_E$ that inflate — both excluding (true) and including (total) false positives. The sampling techniques ($P_{\rm orig}$, $P_{\rm square}$, $P_{\dot\phi}$, and $P_{\dot\psi}$) are explained in the text. Excluding the ambiguous or false positive cases only significantly affects the success probability for $E \gtrsim 10^{-1} M_{\rm Pl}$.

draws one velocity v_1 from a uniform distribution, bounded by $\pm\sqrt{2(E^4 - V_0)}$, and then sets v_2 by the energy constraint (3.8). All signs are chosen randomly and this procedure is alternated on subsequent choices of points to obtain a symmetric distribution in the velocities. The second prior $P_{\rm square}$ is similar, except we draw the *square* of the velocity v_1^2 from a uniform distribution bounded below by zero and above by $2(E^4 - V_0)$, with the sign of v_1 chosen randomly. Again, we alternate this to obtain a symmetric distribution. With this modest change in prior, the calculated fraction $f_{\rm true}$ of $\mathcal{C}_E$ that inflates (excluding false positives) differs by only a few percent, with $P_{\rm square}$ giving a slightly lower fraction at each energy. The fraction $f_{\rm true}$ again decreases with decreasing E.

We compare this to two priors $P_{\dot\phi}$ and $P_{\dot\psi}$ that are asymmetric in the velocities. For $P_{\dot\phi}$ we always draw $\dot\psi_0$ from a uniform distribution bounded

by $\pm\sqrt{2(E^4 - V_0)}$ and always set $\dot{\phi}_0$ by the energy constraint. For $P_{\dot{\psi}}$ we do the opposite: draw $\dot{\phi}_0$ and set $\dot{\psi}_0$. This gives a uniform distribution in the sampled velocity v_1, but a high-tail distribution similar to Fig. 3.6 in the velocity v_2. The prior $P_{\dot{\phi}}$ focuses more of the sample around $\dot{\psi}_0 \approx 0$, the area identified as being most-likely to inflate, and $P_{\dot{\psi}}$ gives more points around $\dot{\phi}_0 \approx 0$, the area least-likely to inflate. At $E = M_{\rm Pl}$ the difference in $f_{\rm total}$ (including false positives) between the asymmetric priors is as much as 41.0 percentage points. The differences decrease with decreasing E, indicating that later-time hypersurfaces become progressively independent of the prior. However, Table 3.3 demonstrates how any measure of f is prior-dependent, especially with respect to the implicit dependence of the prior on the initial energy.

3.5 Conclusion

We have considered the initial conditions problem for multifield inflation, quantifying the likelihood of inflation by sampling an initial conditions surface, evolving the points numerically, and dividing them into successfully and unsuccessfully inflating sets. We draw initial conditions from an equal energy slice of phase space, denoted $\mathcal{C}_E$, the maximum energy at which the underlying theory is assumed to be an accurate description of the primordial universe. Since FLRW universes have a monotonic energy density, sampling initial conditions from $\mathcal{C}_E$ ensures that we count only unique solutions to the equations of motion. A sample of points from $\mathcal{C}_E$ is thus a well-defined sample of homogeneous universes. Typically, we cannot predict the flux of orbits through $\mathcal{C}_E$ and must choose a prior, accordingly. We considered four different uninformative priors on $\mathcal{C}_E$ and showed that the likelihood of inflation varies by as much as

a factor of roughly two between candidate priors. However, one can imagine scenarios where the prior dependence was much more dramatic.

After specializing to hybrid inflation we examined the topology of the set of successful points $\mathcal{S}_E$, which is independent of continuous deformations to the prior. We confirm that both $\mathcal{S}_E$ and the boundary between the successful and unsuccessful points is fractal for all sampled energies. The structure of $\mathcal{S}_E$, as seen in Figs 3.3 to 3.5, is qualitatively smoother than when initial conditions are chosen from the zero-velocity slice shown in Fig. 3.1. Further, since the equations of motion (3.3)–(4.4) are dissipative, there must be a small-scale cutoff to any fractal structure. However, quantum corrections to the classical analysis presented here will generate inhomogeneities in the resulting semi-classical picture, which would depend on the detailed behavior of the pre-inflationary state. This puts a fundamental lower limit on the homogeneity of the early universe: if $\mathcal{S}_E$ has structure below this scale, the assumption of homogeneity is not self-consistent. Fluctuations are larger at higher energies and above some critical energy E the number of viable, homogeneous scenarios is vanishingly small, even though the naïve counting statistic suggests that a nontrivial fraction of the initial conditions space is inflationary.

Our specific calculations are performed for the hybrid potential (4.4), but our underlying goal is to develop tools that can be applied to the initial conditions problem associated with generic multifield scenarios. Recent progress has been made by studying both random multifield models [133–138] and inflection point models [132, 138–142]. These approaches yield contrasting conclusions regarding the distribution of inflationary trajectories; applying the methods developed here to these models will be an interesting extension of this work.

This analysis assumes that the universe is initially spatially flat and homogeneous, but even if inflation begins without tuning in the homogeneous

limit there is no guarantee that this result will survive the addition of pre-inflationary inhomogeneities. Inhomogeneous pre-inflationary configurations were examined by Goldwirth and Piran [143–145], who showed that single-field chaotic inflation and new inflation [3, 4] remain robust in the presence of nontrivial inhomogeneity, provided that the initial field value is approximately correlated over several Hubble radii. We examine this question with lattice PDE techniques in Chapter 4.

Chapter 4

Inflating an Inhomogeneous Universe

This chapter is adapted from:

R. Easther, L. C. Price, and J. Rasero,

Inflating an Inhomogeneous Universe

JCAP 1408 (2014) 041, [146]

4.1 Abstract

While cosmological inflation can erase primordial inhomogeneities, it is possible that inflation may not begin in a significantly inhomogeneous universe. This issue is particularly pressing in multifield scenarios, where even the homogeneous dynamics may depend sensitively on the initial configuration. This chapter presents an initial survey of the onset of inflation in multifield models, via qualitative lattice-based simulations that do not include local gravitational backreaction. Using hybrid inflation as a test model, our results suggest that small subhorizon inhomogeneities do play a key role in determining whether inflation begins in multifield scenarios. Interestingly, some configurations which do not inflate in the homogeneous limit "succeed" after inhomogeneity is included, while other initial configurations which inflate in the homogeneous limit "fail" when inhomogeneity is added.

4.2 Introduction

The key predictions of inflation are strongly supported by observations of both large-scale structure [147–150] and the cosmic microwave background, *e.g.*, WMAP9 [123, 124], ACT [125], SPT [122, 151], and *Planck* [17, 152]. While inflation can ameliorate fine-tunings associated with the hot Big Bang, this presupposes that the inflationary mechanism does not itself rely on fine-tuned fundamental parameters.[1] In particular, if inflation can only begin from a narrow range of possible configurations of the pre-inflationary universe, then the fine-tuning problems of the standard Big Bang have not been solved.

Despite its importance, the inflationary initial conditions problem has received relatively little attention. In some cases (*e.g.*, new inflation [3, 4, 157]) the initial conditions must be tuned in the purely homogeneous limit, but a complete treatment of the issue involves the fully inhomogeneous Einstein equations. This problem has been addressed for single-field inflation, with the conclusion that approximate homogeneity is needed over a volume of a few Hubble radii for chaotic inflation [144, 145], whereas new inflation has an inflationary attractor [158–161]. However, the inhomogeneous dynamics of multifield inflation are almost entirely unexplored. Multifield inflation models have rich dynamics and are motivated from high-energy theory [162–165], making them relevant for studies of inflationary initial conditions.

We take the first step toward analysing this topic by performing lattice simulations of the pre-inflationary period for two-field hybrid inflation [81, 82, 119]. This is a qualitative exploration, as our results are based on solutions of the inhomogeneous scalar field dynamics in a homogeneous, expanding spacetime, ignoring both local gravitational backreaction and non-zero spatial curvature.

[1] For a recent discussion of these problems see Refs [153–156].

By ignoring inhomogeneities in the metric we are making the same assumptions that underpin a vast number of numerical studies of inflationary preheating. We focus on initial configurations which represent small perturbations to a homogeneous background, as the small initial field gradients ensure that our analysis is self-consistent. Furthermore, this approach allows us to take advantage of the mature numerical tools that have been developed to analyze preheating [166–168]. Consequently, while this project represents a significant advance on previous studies of the initial conditions problem for multifield inflation, all of which have been performed in the purely homogeneous limit, it also paves the way for analyses based on full numerical relativity.[2]

The chaotic nature of the homogeneous limit of multifield inflation (as investigated in Ref. [21] and Chapter 3) means adjacent trajectories in phase space are highly divergent, but as field gradients contribute to the energy density, field values at nearby *spatial* points cannot diverge by arbitrary amounts. This effect potentially "focusses" trajectories relative to the homogeneous limit, and our lattice-based simulations let us explore the role of the gradient energy in the inhomogeneous evolution of this system. Using Monte Carlo explorations of the initial conditions space, we confirm that the qualitative consequences of the chaotic dynamics, especially phase-space mixing, persist when moderate-to-large inhomogeneity is added. However, for many initial configurations the inflationary outcome is not changed by the addition of small amplitude inhomogeneities, demonstrating the focussing effect. Moreover, while many initial conditions that "succeed" in the homogeneous limit do "fail" when in-

[2]Numerical solvers for the single field Einstein-Klein-Gordon equation in three dimensions are described by [144, 145, 169], and there has been recent progress in simulations of highly inhomogenous bubble collisions for single field systems in one dimension [170, 171] but three dimensional, multifield scenarios with significant inhomogeneity are beyond the scope of currently available numerical tools.

homogeneity is included, we also see initial configurations which "fail" in the homogeneous limit that successfully inflate when inhomogeneity is included.

4.3 Model

We consider hybrid inflation [81, 82] with two inhomogeneous scalar fields ϕ and ψ, in a flat FLRW universe with equations of motion

$$\ddot{\phi}_i + 3H\dot{\phi}_i - \frac{1}{a^2}\nabla^2\phi_i + \frac{\partial V}{\partial \phi_i} = 0\,, \tag{4.1}$$

where a is the scale factor, $H = \dot{a}/a$ is the Hubble parameter, and a subscript i denotes the components of the vector $\{\phi, \psi\}$. The inhomogeneous energy density is

$$\rho(t, \mathbf{x}) = \frac{1}{2}\sum_i \left[\dot{\phi}_i^2 + \frac{(\nabla\phi_i)^2}{a^2}\right] + V(\phi_i), \tag{4.2}$$

the pressure is

$$p(t, \mathbf{x}) = \frac{1}{2}\sum_i \left[\dot{\phi}_i^2 - \frac{1}{3}\frac{(\nabla\phi_i)^2}{a^2}\right] - V(\phi_i), \tag{4.3}$$

and a evolves according to the Einstein equations. In general, the metric is spatially dependent, but we set $a = \langle a(t, \mathbf{x})\rangle$ and $H^2 = \langle \rho(t, \mathbf{x})\rangle/3$, where $\langle . \rangle$ indicates an integrated spatial average, which is an accurate approximation when the fields' variance is small. Relaxing this assumption would require a full numerical treatment of the Einstein equations.

The generic hybrid inflation potential V has the form

$$V(\phi, \psi) = \Lambda^4\left[\left(1 - \frac{\psi^2}{M^2}\right)^2 + U(\phi) + \frac{\phi^2\psi^2}{\nu^4}\right], \tag{4.4}$$

where $U(\phi)$ drives a sustained period of slow-roll inflation in the "inflationary valley" at $\psi \approx 0$, but is otherwise subdominant. A graceful exit from inflation occurs when the effective mass of the waterfall field $m^2_{\text{eff},\psi} \equiv \Lambda^4(\phi^2/\nu^4 - 2/M^2)$ becomes imaginary.

Parameter	Λ	M	μ	ν
Value $[M_{\rm Pl}]$	$6.8{\times}10^{-6}$	0.03	500.0	0.015

Table 4.1: Parameter values for the potential in Eqs (4.4) and (4.5). The overall energy scale is set by Λ, but the background dynamics are not affected by this choice.

We work with

$$U(\phi) = \frac{\phi^2}{\mu^2}, \tag{4.5}$$

although the *Planck* results [152] rule out slow-roll inflation with this form of $U(\phi)$, since it predicts $n_s > 1$. However, the exact form of $U(\phi)$ is likely to have little impact on the initial conditions problem since, by hypothesis, it only dominates the potential in a small portion of field space and the multifield dynamics for this scenario are well-studied in Refs [22,107–112] and Chapter 3. We use hybrid inflation as a toy model to illustrate the interesting multifield dynamics resulting from the interaction between the dynamical fixed points at $\psi = \{0, \pm M\}$ and the tachyonic instability points $\phi_{\rm crit} = \pm\sqrt{2}\,\nu^2/M$. We note that a red scalar spectrum can be achieved through other choices of $U(\phi)$ [172,173], as does inflation during the waterfall transition [112,120,121,174].

The numerical parameters used in our simulations are listed in Table 4.1. The background dynamics are independent of the value of Λ, but we choose $\Lambda = 6.8 \times 10^{-6} M_{\rm Pl}$ to match the measured amplitude of the scalar power spectrum [152]. The onset of inflation in this model has been thoroughly investigated in the homogeneous limit (*e.g.*, Refs [22,107–112] and Chapter 3) and surveys of initial conditions that consider both the initial velocities and field values [22, 105,112] find that hybrid inflation scenario begins for a significant fraction of initial configurations. However, the chaotic nature of the underlying dynamics

ensures that the set of successful initial conditions is fractal.

4.4 Numerical methods

Equations: We solve the equations of motion (4.1) using LatticeEasy[3] [166] and assuming periodic boundary conditions $\phi_i(t,\mathbf{x}) = \phi_i(t,\mathbf{x}-\mathbf{L})$, where $\mathbf{L}$ is the length of the spatial box defined by the simulation. On a lattice, the Fourier transforms can be expressed as a finite series

$$\phi_i(t,\mathbf{x}) = \int \frac{d^3k}{(2\pi)^3}\hat{\phi}_{i,\mathbf{k}}(t)e^{2\pi i\mathbf{k}\cdot\mathbf{x}} \to \frac{1}{L^3}\sum_{\mathbf{k}}\hat{\phi}_{i,\mathbf{k}}(t)e^{2\pi i\mathbf{k}\cdot\mathbf{x}}\,. \tag{4.6}$$

We specify initial conditions in Fourier space, through $\hat{\phi}_{i,\mathbf{k}}(0)$ and its time derivatives $\partial_t\hat{\phi}_{i,\mathbf{k}}(0)$. In order to sample a large number of initial configurations, we restrict the inhomogeneity to one spatial direction, effectively assuming a translational symmetry in the orthogonal directions. We allow a small initial velocity in the 0^{th} mode, but set $\partial_t\hat{\phi}_{i,\mathbf{k}>0} = 0$.

Inhomogeneous $T_{\mu\nu}$: With a single excited mode, the initial field configuration is

$$\phi_i(0,x) = \bar{\phi}_{i,0}\left[1 + A\sin\left(\frac{2\pi nx}{L}\right)\right]. \tag{4.7}$$

Periodic boundary conditions require the lattice-size to be a multiple of the wavelength $k = n/L$ for some integer n. Without loss of generality, we can set the boxsize L to the wavelength of the largest mode we excite, given our choice of periodic boundary conditions, and define $n_{\text{largest}} \equiv 1$.

We further assume that $A \lesssim 1$ to keep the backreaction on the scale factor initially small and maintain the self-consistency of Eq. (4.1). The average

[3] www.felderbooks.com/latticeeasy/

initial energy density is

$$\langle \rho_0 \rangle = \frac{1}{2} \sum_i \dot{\phi}_i^2 + \langle V(\phi_i) \rangle + \sum_i \left(\frac{n\pi A \bar{\phi}_{i,0}}{a_0 L} \right)^2 \tag{4.8}$$

and the initial average gradient energy density is suppressed by $(nA/L)^2$. Likewise, the relevant contribution of the inhomogeneity to the trace and traceless parts of the stress tensor are proportional to the square of the field gradient and are also suppressed by this factor at the start of the simulation. The momentum density is

$$\mathcal{J}_j = -\sum_i \dot{\phi}_i \partial_j \phi_i, \tag{4.9}$$

which we keep small initially by considering only small initial velocities in the 0^{th} mode, combined with a small value for nA/L. However, the spatial average of $\mathcal{J}_j$ over the simulation volume is strictly zero when the fields have the form in Eq. (4.7).

As the simulation progresses we do not require that the components of the energy-momentum tensor to remain small, but only require that a and H are well approximated by their spatial average. To ensure that the inhomogeneous contributions to the stress-energy tensor do not induce a large backreaction on the subsequent evolution, we require that each field's variance

$$\text{Var}_i \equiv \left\langle \phi_i^2 \right\rangle - \langle \phi_i \rangle^2 \tag{4.10}$$

remains small throughout the simulation, since large values would require a more sophisticated analysis involving solutions of the full Einstein field equations. Solutions for which the variance exceeds $\text{Var}_i \gtrsim 10^{-2}\ {M_{\text{Pl}}}^2$ are dropped from our analyses, but in practice, almost none of the configurations we consider generate variances that cross this threshold, as the overall simulation time is relatively short.

Initial inhomogeneity: We parametrize the initial inhomogeneity associated with a mode of wavenumber k using f, the ratio of its wavelength λ to the initial Hubble radius in the homogeneous limit:

$$f \equiv \frac{a_0 \bar{H}_0}{k}, \tag{4.11}$$

where $a_0 \equiv 1$ is the initial scale factor and $\bar{H}_0$ is the initial Hubble parameter in the homogeneous limit, *i.e.*, using only $\bar{\phi}_{i,0}$ and $\partial_t \bar{\phi}_{i,0}$. The initial horizon size in the homogeneous limit is related to the size of the simulation box by $2\pi f = a_0 \bar{H}_0 L$. We consider only subhorizon perturbations with $f \lesssim 1$ since superhorizon inhomogeneities can be well modeled by a collection of homogeneous universes with different initial conditions, using the separate universe assumption. Subhorizon inhomogeneities contribute only perturbatively to the Newtonian potential, which further justifies ignoring metric inhomogeneities. Assuming we start in an almost-FLRW universe, these small-scale inhomogeneities can contribute only an effective pressure term with $w = 1/3$ that cannot contribute to exponential expansion [175].

Ending condition: We require $N_e \geq 55$ e-folds of accelerated expansion with $\epsilon < 1$, although this limit is somewhat arbitrary as almost any specific initial condition yields either $N_e \gg 55$ or $N_e \ll 5$. We follow previous analyses, such as Refs [22, 112] and Chapter 3, by defining an initial configuration as "successful" if it gives $N_e > 55$, and as a "failure" if it does not. In practice, almost all of the e-folds occur in the inflationary valley when $\psi \approx 0$, so we halt our simulations once $N_e > 5$ and $\langle \psi \rangle \approx 0$, *i.e.*, once the trajectory has settled into the inflationary valley. Alternatively, we stop the integration if $\rho < V(0, \phi_c) = 2\Lambda^4 \nu^4 / M^2 \mu^2$, since the trajectory cannot enter the inflationary valley; these trajectories are by definition unsuccessful. In Section 4.5 we compare our results for initial configurations with non-zero gradient energies

to the homogeneous cases studied in Refs [22, 105, 108–112], which are in the "homogeneous limit" with $\nabla\phi_{i,0} \to 0$.

4.5 Results

4.5.1 Single excited mode

We begin by examining two specific background initial conditions, $\mathrm{IC}_{\mathrm{succ}}$ and $\mathrm{IC}_{\mathrm{fail}}$, which have different homogeneous dynamics. These correspond to choices of initial conditions for which $N_e > 55$ and $N_e < 5$, respectively. The specific choices are

$$\mathrm{IC}_{\mathrm{succ}} \equiv \begin{bmatrix} \bar{\psi}_{0,\mathrm{succ}} \\ \bar{\phi}_{0,\mathrm{succ}} \\ \dot{\bar{\psi}}_{0,\mathrm{succ}} \\ \dot{\bar{\phi}}_{0,\mathrm{succ}} \end{bmatrix} = \begin{bmatrix} 9.6405 \times 10^{-3}\, M_{\mathrm{Pl}} \\ 2.7359 \times 10^{-2}\, M_{\mathrm{Pl}} \\ -1.0211 \times 10^{-10}\, M_{\mathrm{Pl}}^2 \\ 1.6059 \times 10^{-11}\, M_{\mathrm{Pl}}^2 \end{bmatrix}, \tag{4.12}$$

$$\mathrm{IC}_{\mathrm{fail}} \equiv \begin{bmatrix} \bar{\psi}_{0,\mathrm{fail}} \\ \bar{\phi}_{0,\mathrm{fail}} \\ \dot{\bar{\psi}}_{0,\mathrm{fail}} \\ \dot{\bar{\phi}}_{0,\mathrm{fail}} \end{bmatrix} = \begin{bmatrix} 1.0361 \times 10^{-2}\, M_{\mathrm{Pl}} \\ 2.7497 \times 10^{-2}\, M_{\mathrm{Pl}} \\ -6.6330 \times 10^{-11}\, M_{\mathrm{Pl}}^2 \\ 7.3672 \times 10^{-11}\, M_{\mathrm{Pl}}^2 \end{bmatrix}. \tag{4.13}$$

The combined initial kinetic and potential energy is $E_0 = 10^{-5}\, M_{\mathrm{Pl}}$ and quantum fluctuations at this energy should have minimal impact on the end-state of the background evolution, as studied in Chapter 3. By adding initial inhomogeneity to these background field values, we find that the amount of inflation given by both of these trajectories can change drastically.

In Fig. 4.1 we plot the spatially averaged values of (ϕ, ψ) for a set of 10 configurations with background field values of $\mathrm{IC}_{\mathrm{fail}}$. We perturb each configu-

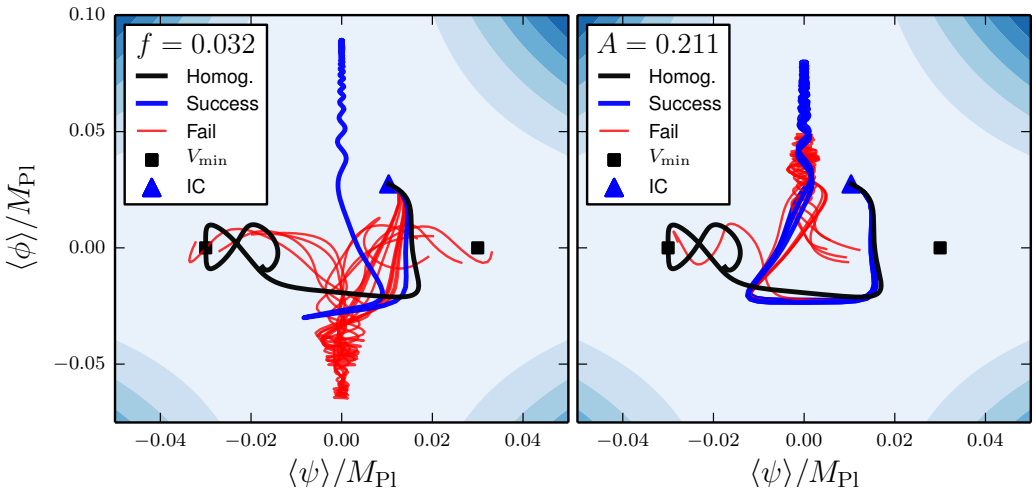

Figure 4.1: Spatially averaged solutions to Eq. (4.1) for ten initial conditions with the same background field values $\mathrm{IC}_{\rm fail}$, with a sinusoidal inhomogeneity, of amplitude A and comoving wavelength $\lambda/2\pi = f/a_0\bar{H}_0$, added in-phase to both fields. In the homogeneous limit the background field values give $N_e \ll 55$. The blue contours show the potential energy density V. (*Left*) The initial fraction f is fixed and the amplitude is varied between $10^{-0.5} < A < 1$. (*Right*) The initial amplitude is fixed to $A = 1$ and the fraction f is varied between $10^{-2} < f < 10^{-1}$.

ration by adding a sinusoidal inhomogeneity with equal phases (as in Eq. (4.7)) to both fields. All of the plotted solutions explore much of the field space and most of the sampled trajectories are eventually captured in the inflationary valley at $\langle\psi\rangle = 0$; however, only some trajectories stay there and inflate sufficiently. Interestingly, this demonstrates that subhorizon inhomogeneity can actually cause inflation in scenarios that fail to inflate in the homogeneous limit. Hybrid inflation has been shown to be chaotic, first in the $H \to 0$ limit in Ref. [21], then in the homogeneous limit in Refs [22, 112] and Chapter 3. Since phase-space mixing is a characterisitic of chaos, this is the first indication that this behaviour extends to the inhomogeneous Klein-Gordon equation. The non-linear dynamics of multifield inflation may therefore have a significant

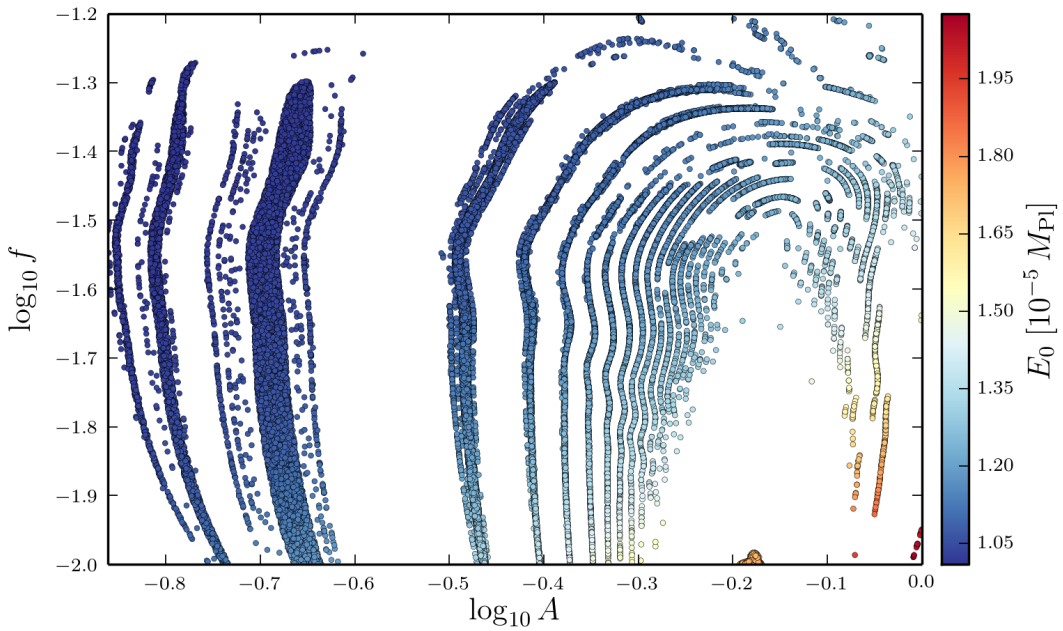

Figure 4.2: Distribution of independent initial conditions that succeed at generating $N_e > 55$ e-folds of inflation, as a function of initial inhomogeneity. The background field values $\mathrm{IC}_{\mathrm{fail}}$ are set so that in the homogeneous limit $N_e \ll 55$. A sinusoidal inhomogeneity, with amplitude A and comoving wavelength $\lambda/2\pi = f/a_0\bar{H}_0$, has been added, in-phase, to both fields. The initial energy E_0 is indicated by color.

effect on whether inflation successfully begins with from an inhomogeneous universe.

Since we are solving (1+1)-dimensional PDEs, the computational cost of evaluating each configuration is not excessive and we are able to generate large samples to test whether this behavior is generic. Figure 4.2 shows $\mathcal{O}(10^6)$ Monte Carlo samples with background field values of $\mathrm{IC}_{\mathrm{fail}}$. We again add a sinusoidal inhomogeneity with logarithmic priors on the parameters, $-2.0 < \log_{10} f < -1.2$ and $-1.0 < \log_{10} A < 0.0$. Trajectories with lower initial gradient energy than this do not deviate significantly from the homogeneous solution and fail. The set of successful points has a fractal structure, similar to that seen

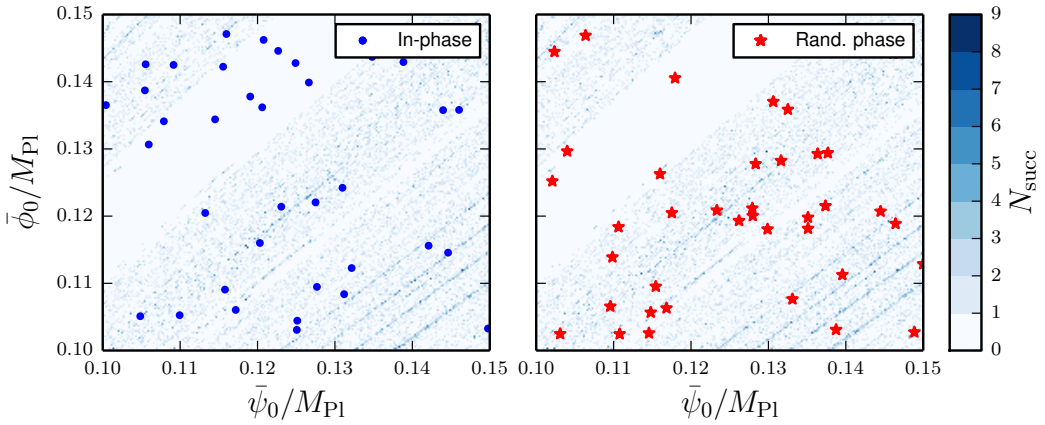

Figure 4.3: Addition of sub-horizon inhomogeneity can turn failure ICs into successful ICs. We add one sinusoidal inhomogeneity (*left*) in-phase and (*right*) with a random phase difference to 50 randomly selected background ICs that fail in the homogeneous limit. We find 38/50 and 39/50 change to "successful," respectively, with no noticeable correlations between them. (*Background*) Histogram of successfully inflating ICs ($N_e \gg 55$) in the homogeneous limit, with the number of successful points per bin $N_{\rm succ}$ indicated by color.

with homogeneous hybrid inflation. Using the box-counting method defined in Eq. (3.12) we are able to determine a fractal dimension of $d = 1.27$, $d = 1.85$, and $d = 1.25$, for the set of points in Fig. 4.2 that are successful, unsuccessful, and the boundary between the two, respectively. This is convincing evidence that the dynamics remain chaotic in some regions of parameter space.

We also check that this behavior does not depend on the specific choice of $\mathrm{IC}_{\rm fail}$, by looking at scenarios with different background field values, and with the perturbations in ϕ and ψ either in-phase or with an arbitrarily chosen phase difference. The results of this investigation are presented in Fig. 4.3. We set the initial field velocities to zero and draw the background initial conditions from $0.10\,M_{\rm Pl} < \bar{\phi}_0, \bar{\psi}_0 < 0.15\,M_{\rm Pl}$. We then chose 50 configurations that fail in the homogeneous limit and add sub-horizon inhomogeneity with arbitrary

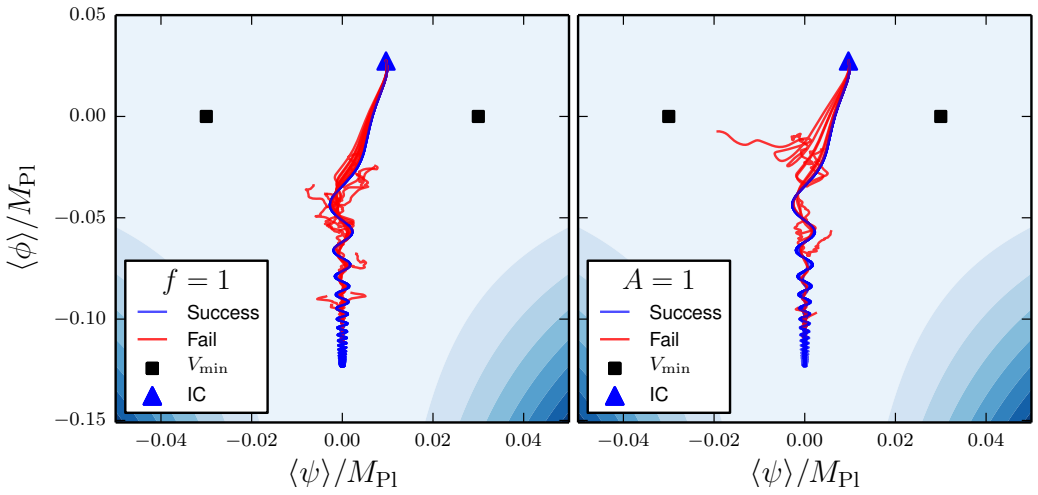

Figure 4.4: Spatially averaged solutions to the inhomogeneous Klein-Gordon equation for twenty initial conditions $\mathrm{IC}_{\mathrm{succ}}$, and varying initial gradient energy, provided by a sinusoidal inhomogeneity, with amplitude A and comoving wavelength $\lambda/2\pi = f/a_0\bar{H}_0$, in each field and with identical phase. The blue contours show the potential energy density V. (*Left*) The initial inhomogeneous wavelength is fixed to the initial Hubble scale $f = 1$ and the amplitude is varied between $10^{-3} < A < 1$. (*Right*) The initial amplitude is fixed $A = 1$ and the wavelength is varied between $10^{-2} < f < 1$.

or zero phase differences between the modes in each field. In most cases we find a mixture of inflationary and non-inflationary solutions at each point, demonstrating the generality of this phenomenon.

Conversely, Fig. 4.4 displays the spatially averaged trajectories for initial configurations with background field values of $\mathrm{IC}_{\mathrm{succ}}$ with the in-phase sinusoidal perturbations. The spatially averaged field trajectories begin by following the homogeneous trajectory and oscillating around the inflationary valley at $\langle\phi\rangle < -\phi_{\mathrm{crit}}$. For those configurations with initially small gradient energies, accelerated expansion exponentially dampens the inhomogeneity, the trajectory is captured in the inflationary valley, and successfully inflates. The suc-

cessfully inflating trajectories in Fig. 4.4 are nearly indistinguishable from each other and from the field-space trajectory of the homogeneous solution. With larger gradient energies — obtained either by reducing the wavelength of the perturbation relative to the horizon or increasing the amplitude A — the inhomogeneity can pull the spatially averaged trajectory out of the valley. These trajectories then evolve more-or-less directly to the minimum of the potential and will give at most a few e-folds during any transient inflationary phases.

Fig 4.5 gives the variance Var_i for representative successful and unsuccessful solutions with initial background field values of $\mathrm{IC}_{\mathrm{succ}}$. For the successful case, the trajectory is captured by the false vacuum and oscillates around $\langle\psi\rangle = 0$ with a frequency of 40 [oscillations/e-fold]. Since $\mathrm{Var}_\psi \sim \langle\psi\rangle^2$ it therefore oscillates at a frequency of 80 [oscillations/e-fold]. The variance in ϕ peaks only once at $N_e = 0.5$ and remains below $\mathrm{Var}_\phi < 10^{-7}\ M_{\mathrm{Pl}}^2$. In the failing universe there is no extended period of oscillation around the false-vacuum at $\langle\psi\rangle = 0$, so the oscillations in Var_ψ have a much smaller frequency. After $N_e \gtrsim 0.5$ the inhomogeneities in ψ start to grow substantially, destablising the dynamics, and causing failure.

Figure 4.6 shows the results of a Monte Carlo sampling for $\mathrm{IC}_{\mathrm{succ}}$, analogous to that in Figure 4.2, with one initially excited mode added in-phase to both ψ and ϕ. We again use a logarithmic prior, but with the ranges: $-2.0 < \log_{10} f < 0.0$ and $-3.0 < \log_{10} A < 0.0$. Adding perturbations to $\mathrm{IC}_{\mathrm{succ}}$ with initially small gradient energies does not cause the spatially averaged trajectories in field-space to deviate significantly from the homogeneous solution, as seen in Fig. 4.4, and these configurations successfully inflate. However, if we add more significant inhomogeneity with amplitude $A \gtrsim 0.1$, then any transitory inflation is typically disrupted before $N_e \sim 5$. We do not see any indication of a fractal structure in the distribution of successful configuration in (A, f)-space for this

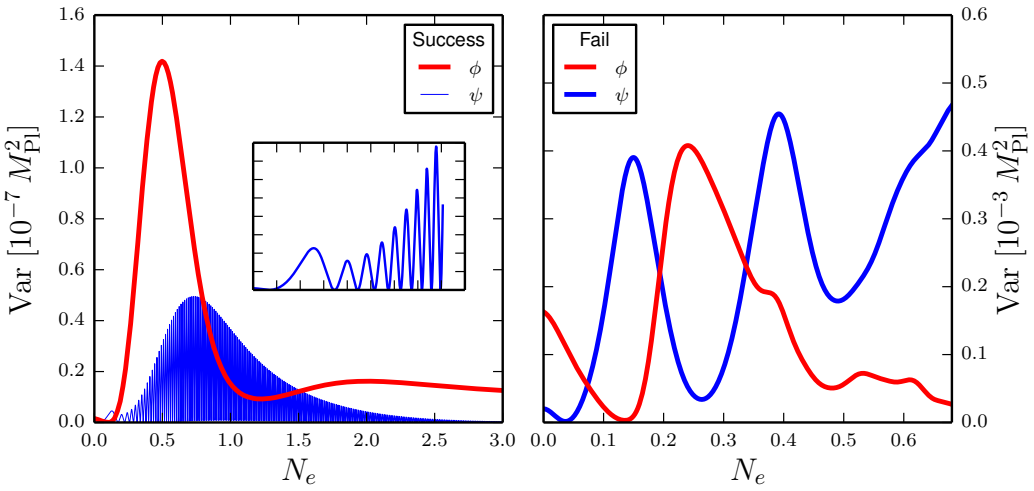

Figure 4.5: Variance in the fields $\mathrm{Var}_i = \langle \phi_i^2 \rangle - \langle \phi_i \rangle^2$ as a function of e-folding N_e for initial configurations with background field values of $\mathrm{IC}_{\mathrm{succ}}$, as in Fig. 4.4. (*Left*) Configuration yielding $N_e > 55$ with $f = 1.890 \times 10^{-1}$ and $A = 2.035 \times 10^{-3}$; (*left inset*) zoom-in on ψ for $N_e < 0.403$. (*Right*) Configuration yielding $N_e \ll 55$ with $f = 3.556 \times 10^{-1}$ and $A = 6.598 \times 10^{-1}$.

initial condition.

4.5.2 Multiple excited modes

We now turn to the more general case, with multiple excited modes in both fields ϕ and ψ:

$$\phi_i(0,x) = \bar{\phi}_{i,0}\left[1 + \sum_{j=1}^{\mathcal{N}} A_{ij} \sin\left(\frac{2\pi n_{ij} x}{L} + \alpha_{ij}\right)\right], \tag{4.14}$$

where A_{ij} is the real amplitude and α_{ij} is the phase of the j^{th} mode for the i^{th} field. The box size L is set to the wavelength of the largest mode of interest by fixing f via Eq. (4.11). The integer n_{ij} gives the ratio of the i^{th} field's j^{th} mode's wavelength, relative to the largest mode. Each field is assumed to have $\mathcal{N}$ excited modes.

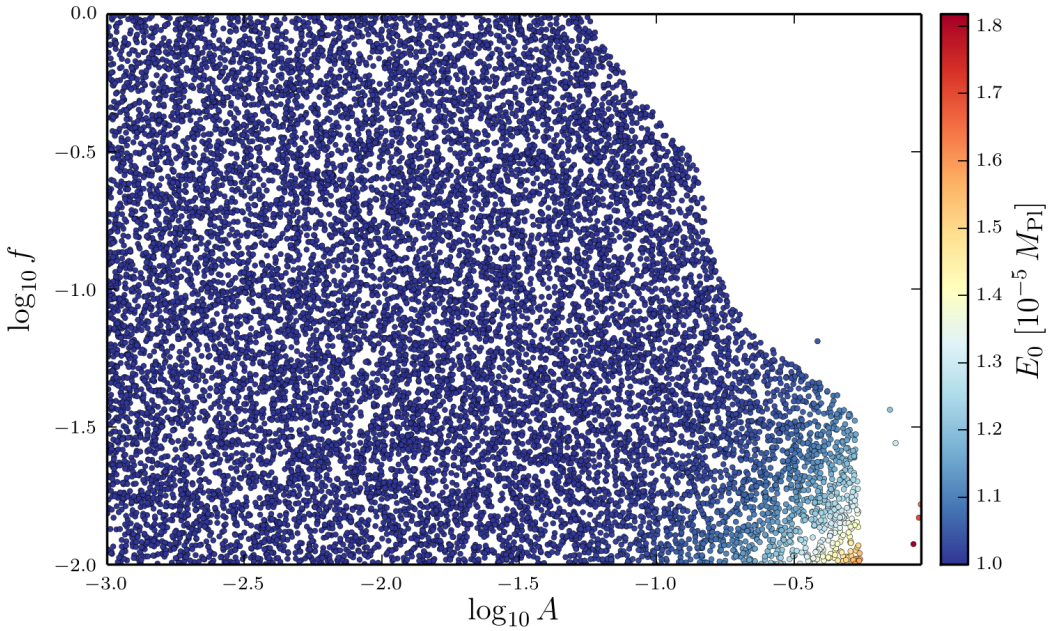

Figure 4.6: Distribution of independent ICs that succeed at generating $N_e > 55$ e-folds of inflation, as a function of initial inhomogeneity. The background field values $\mathrm{IC}_{\mathrm{succ}}$ are set so that in the homogeneous limit $N_e > 55$. A sinusoidal inhomogeneity, with amplitude A and comoving wavelength $\lambda/2\pi = f/a_0\bar{H}_0$, has been added, in-phase, to both fields. The initial energy E_0 is indicated by color.

Figs 4.7 and 4.8 plot the results of a Monte Carlo analysis with $\mathcal{N} = 2$ excited modes. We choose the background values $(\bar{\psi}, \bar{\phi}, \partial_t\bar{\psi}, \partial_t\bar{\phi})$ so that each configuration has initial energy $E_0 = 10^{-5}\, M_{\rm Pl}$ using the *iso-E* measure of Chapters 3 and 5. In general, multifield models make predictions for observables that are largely independent of the prior probability distribution of the ICs, as demonstrated in Ref. [42] and Chapters 3 and 5, so this choice should not have a large effect on the results. We then add initial inhomogeneity, which marginally increases the overall energy. We draw the amplitudes from a logarithmic prior, $10^{-2} < A_{ij} < 1$, and the largest mode with a logarithmic prior in the range $10^{-3} < f < 1$. The wavelength of the second mode is drawn uniformly

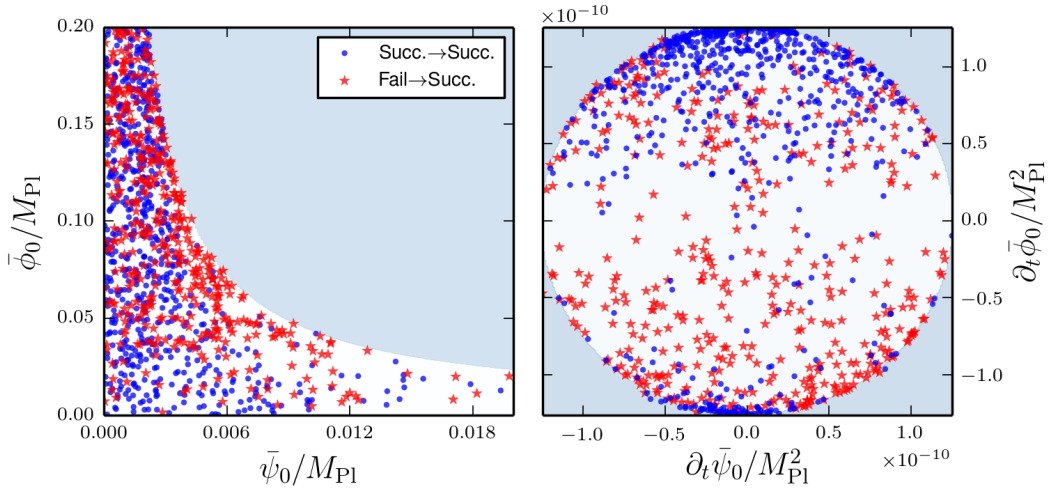

Figure 4.7: Distribution of successful ICs in (*left*) field-space and (*right*) velocity-space that are (*blue dots*) successful and (*red stars*) unsuccessful at giving $N_e > 55$ in the homogeneous limit. The homogeneous ICs are chosen with $E_0 = 10^{-5}\,M_{\rm Pl}$. The ICs have two initially excited modes of different scales. (*Background*) The gray region has not been sampled since the initial energy density would have exceeded E_0^4. For the velocities, the background has also been offset by Λ^4.

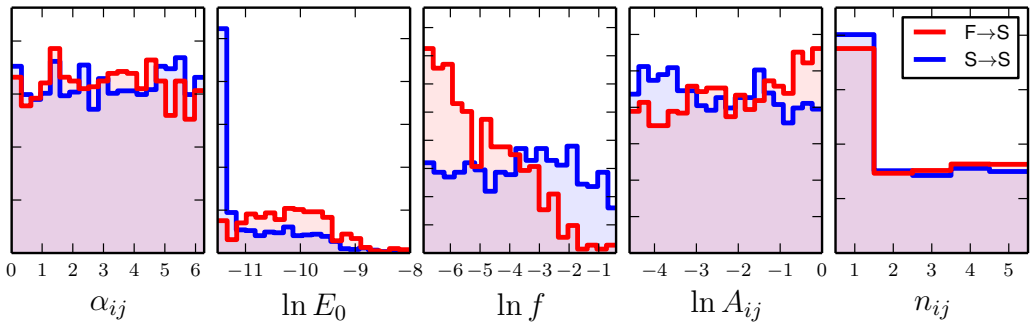

Figure 4.8: Histograms of marginalized inhomogeneity parameters from Eq. (4.14) for successfully inflating ICs; the data for both fields have been plotted together. Two modes have been initially excited in each field and we plot ICs that both (*blue*) succeed and (*red*) fail to inflate in the homogeneous limit. The large amplitude bin at $n = 1$ (*far-right*) results from setting the largest mode to $n = 1$ and is therefore systematic.

from the range $1 < n_{ij} < 5$ with uniform random phase $0 < \alpha_{ij} < 2\pi$. These plots can be compared to Fig. 3.5 in Chapter 3, which presents histograms of successful ICs in the homogeneous limit.

Figure 4.7 shows successful initial configurations projected onto both the homogeneous field space $\{\bar{\psi}_0, \bar{\phi}_0\}$ and the homogeneous velocity space $\{\partial_t\bar{\psi}_0, \partial_t\bar{\phi}_0\}$. When including initial inhomogeneity, successful configurations are approximately uniformly distributed for $\bar{\psi}_0 \lesssim 0.005\, M_{\rm Pl}$. There is some minor difference between the location of ICs that succeed and those that fail, which is primarily due to the the fact that ICs closer to $\psi \approx 0$ tend to be more likely to inflate as they are closer to the inflationary valley. In velocity space, there is a tendency for successful ICs to have $\partial_t\bar{\phi}_0 \sim 10^{-10}\, M_{\rm Pl}^2$ and $\partial_t\bar{\psi}_0 \approx 0$, since having a large velocity in ψ causes the trajectory to evolve away from the inflationary valley at $\langle\psi\rangle \approx 0$. This behavior again matches the homogeneous limit of Chapter 3, as the blue points in Fig. 4.7 cluster in this range. Again, many configurations that fail in the homogeneous limit succeed when multiple modes are initially excited.

Fig. 4.8 displays normalized histograms of the inhomogeneity parameters A_{ij}, n_{ij}, and α_{ij}. Because we have not been careful to sample unique solutions to Eq. (4.1) [105, 176, 177] and because we have used hybrid inflation (4.4) only as a toy model, we do not give a detailed analysis of the inhomogeneity parameters in each field, but rather plot the values together. The histograms do not show any dependence on the phases α_{ij}, indicating that the results in Section 4.5.1, which use in-phase inhomogeneities, are robust. There is a large peak in the mode number n_{ij} at the largest wavelength; however, we have forced at least one mode to have $n_{ij} = 1$ and set the other modes with wavelengths with integer multiples of this largest mode. Consequently, the spike at $n_{ij} = 1$ results from systematics only and there is no strong dependence

on mode number for successful ICs that are either successful or unsuccessful in the homogeneous limit. Because we fix the background energy scale, the histogram for E_0 directly measures the initial gradient energy, which we allow to be up to 35 times the initial homogeneous energy.

Initial configurations that are successful in the homogeneous limit tend to also be successful with initial inhomogeneity, provided the initial gradient energy is relatively small. Again, this can be understood in terms of Fig. 4.4, as the trajectories with small initial gradients are indistinguishable from the homogeneous trajectory. However, many initial configurations that are successful in the homogeneous limit remain successful with a large initial gradient, although the fraction decreases with increasing initial gradient energy.

Points for which inflation fails in the homogeneous limit have a strong dependence on the size of the largest initially excited mode f and a weak dependence on mode amplitude A_{ij}, favoring higher initial gradient energy. The number of successful configurations decreases when the initial energy exceeds $E_0 \gtrsim 7.5 \times 10^{-5} M_{\rm Pl}$. Given that our lattice simulation technique will be unreliable with large gradient energies, these cases need to be investigated within the full Einstein equations.

4.6 Conclusion

We have demonstrated that adding subhorizon inhomogeneity can significantly modify the pre-inflationary dynamics of hybrid inflation, yielding counterintuitive results. While the solutions to the Klein-Gordon equation are generally stable to the addition of small initial inhomogeneity, if the inhomogeneity has a larger amplitude, then the evolution changes dramatically. Unsurprisingly, large primordial inhomogeneities may prevent the onset of inflation in models

which do inflate in the homogeneous limit. However, this is not a certainty: models which do not inflate in the homogeneous limit can successfully inflate when inhomogeneity is added. The spatially averaged trajectories traverse large regions of phase-space when the underlying dynamics are chaotic, giving a greater chance of the trajectory finding attracting solutions, and inflating via a different path in phase-space. We have presented an ensemble Monte Carlo analysis with varying types of initial inhomogeneity to demonstrate that this behavior is generic for hybrid inflation and should be true for any multifield inflation model that has chaotic behavior.

We have analysed the toy hybrid inflation model defined by Eq. (4.4), but argue that this behavior should be common for multifield inflation models that have unstable fixed points or saddle points in the potential. This model does not yield the correct perturbation spectrum, but this is not a significant issue given that our focus here is the onset of inflation.

The solutions to the inhomogeneous Klein-Gordon equation (4.1) are still qualitatively chaotic when the spatially averaged field trajectories are plotted. This chapter thus provides the first confirmation that the chaotic dynamics extend from the ordinary differential equations of the homogeneous problem to the partial differential equations of the inhomogeneous universe. The chaotic dynamics result from the interplay between the fixed points and the saddle point at the critical value for ϕ. Consequently, our qualitative conclusions should extend to other models with these features.

It was argued in Refs. [6, 7] that the conditions necessary to start inflation must extend over a super-Hubble region. Here, we have demonstrated that we do not need to necessarily require homogeneity and that significant sub-horizon perturbations may not prevent inflation from beginning, despite the conventional wisdom. This work clearly has a number of possible exten-

sions, both to wider classes of models and also to include the effects of non-zero curvature, which is generically expected in pre-inflationary scenarios [178,179]. Furthermore, including local gravitational backreaction by solving the full Einstein field equations would extend this analysis to configurations with large or asymmetric gradient energies.

PART IV

Obtaining Generic Predictions

Chapter 5

Simple Predictions from Multifield Inflation

This chapter is adapted from:

R. Easther, J. Frazer, H. V. Peiris, and L. C. Price

Simple predictions from multifield inflationary models

Phys. Rev. Lett. 112 (2014) 161302, [45]

5.1 Abstract

We explore whether multifield inflationary models make unambiguous predictions for fundamental cosmological observables. Focusing on N-quadratic inflation, we numerically evaluate the full perturbation equations for models with 2, 3, and $\mathcal{O}(100)$ fields, using several distinct methods for specifying the initial values of the background fields. All scenarios are highly predictive, with the probability distribution functions of the cosmological observables becoming more sharply peaked as N increases. For $N = 100$ fields, 95% of our Monte Carlo samples fall in the ranges $n_s \in (0.9455, 0.9534)$; $\alpha \in (-9.741, -7.047)\times10^{-4}$; $r \in (0.1445, 0.1449)$; and $r_{\rm iso} \in (0.02137, 3.510)\times10^{-3}$ for the spectral index, running, tensor-to-scalar ratio, and isocurvature-to-adiabatic ratio, respectively. The expected amplitude of isocurvature pertur-

bations grows with N, raising the possibility that many-field models may be sensitive to post-inflationary physics and suggesting new avenues for testing these scenarios.

5.2 Introduction

The study of inflation has been transformed by the advent of precision cosmology. In 2013 the *Planck* Collaboration [18, 19] announced a 5σ detection of scale-dependence in the primordial power spectrum, $\mathcal{P}(k)$. Likewise, the non-Gaussian component of the initial perturbations is less than 0.01% [180] and there are strong limits on isocurvature perturbations [19]. These results are entirely consistent with single-field slow roll inflation.

The key theoretical challenge for inflation is to show how a phase of accelerated expansion is realized in particle physics. However, single-field models are not always natural; *e.g.*, string compactifications often result in hundreds of scalar fields [162–165]. Multifield models yield a wider range of possible $\mathcal{P}(k)$ and higher-order correlators than simple single-field scenarios. Consequently, it is vital to determine not only what is *possible* in multifield models, but whether specific multifield models yield *generic* predictions that can be tested against data.

Multifield models permit many distinct inflationary trajectories, and can thus be sensitive to the initial values of the background fields. The relative likelihood for different initial conditions (ICs) in the overall phase-space of the inflationary dynamical system must be encoded in the Bayesian prior for the model. Inflationary models are, to some extent, *ad hoc* hypotheses, so the IC priors typically cannot be computed or reliably predicted *a priori*. Recently it was pointed out that some multifield models make predictions for

the inflationary observables that do not depend strongly on the specific IC prior [42, 181–184], and this class of model unambiguously predicts the distributions of the inflationary observables. On the other hand, observational data could constrain the initial field configuration for models with strong sensitivity to their initial conditions.

In this chapter we present the first *generic* predictions for a multifield inflation model in the many-field limit. By numerically evolving the perturbations, we find the probability density functions (PDFs) for the spectral index n_s, the tensor-to-scalar ratio r, the running α, and the isocurvature-to-adiabatic ratio $r_{\rm iso}$ in N-quadratic inflation. We give the first complete analysis of the many-field case [85, 87, 89–91, 93] by exploring inflation with $N = 100$ fields. We consider three distinct IC priors to assess the sensitivity of the model's predictions to the initial conditions.

We see novel behavior in the many-field case, where trajectories in field space "turn" until the end of inflation, yielding an increased $r_{\rm iso}$ that may be relevant to reheating. The PDFs for n_s, α, and r become more sharply peaked at large N, implying that the many-field case is predictive. We also obtain high-density samples in the low-N limit [185, 186] with $N = \{2, 3\}$. In this limit we also see sharply peaked PDFs and a nontrivial consistency relation in the (n_s, α)–plane, but with a greater dependence on the IC prior than with $N = 100$ fields.

5.3 Method

We assess the "predictivity" of inflationary models as follows. We draw ICs from a specified prior probability distribution and evolve the background equations of motion. We require the pivot scale $k_{\rm piv} = 0.002\,{\rm Mpc}^{-1}$ to leave the hori-

zon 55 e-folds before the end of inflation; if there are fewer e-folds, we exclude the IC and draw another. Otherwise, we solve the perturbation equations numerically and compute observables by evaluating the power spectra at the end of inflation. Iterating this process, we obtain the PDF for the inflationary observables given the choice of IC prior.

We consider N-quadratic inflation with canonical kinetic terms, minimal coupling to Einstein gravity, and potential

$$V = \frac{1}{2} m_\alpha^2 \phi_\alpha^2 \,, \tag{5.1}$$

with an implied sum over repeated field indices. This model makes an excellent test case as it is both extremely simple and well-defined for any value of N.

For $N = 100$ fields, we follow Ref. [89] and draw the mass values from the Marčenko-Pastur distribution with $\beta = 0.5$. We choose the largest mass ratio as $1/8.08$ and the other masses so that they are equally spaced in the cumulative probability distribution function. We do not expect our results to depend strongly on this choice, provided the masses are all of the same order of magnitude.

5.4 Initial conditions

We consider three IC priors:

1. The *iso-E_0 prior*, defined in Chapter 3, with an equal-area prior on an initial surface with energy E_0.

2. The *iso-N_e prior* [42] with an equal-area prior set approximately N_e e-folds before the end of inflation on the surface $\phi_\alpha \phi_\alpha = 4N_e$.

3. The *slow-roll prior* with velocities set in slow-roll and field ICs distributed uniformly over some pre-defined range.

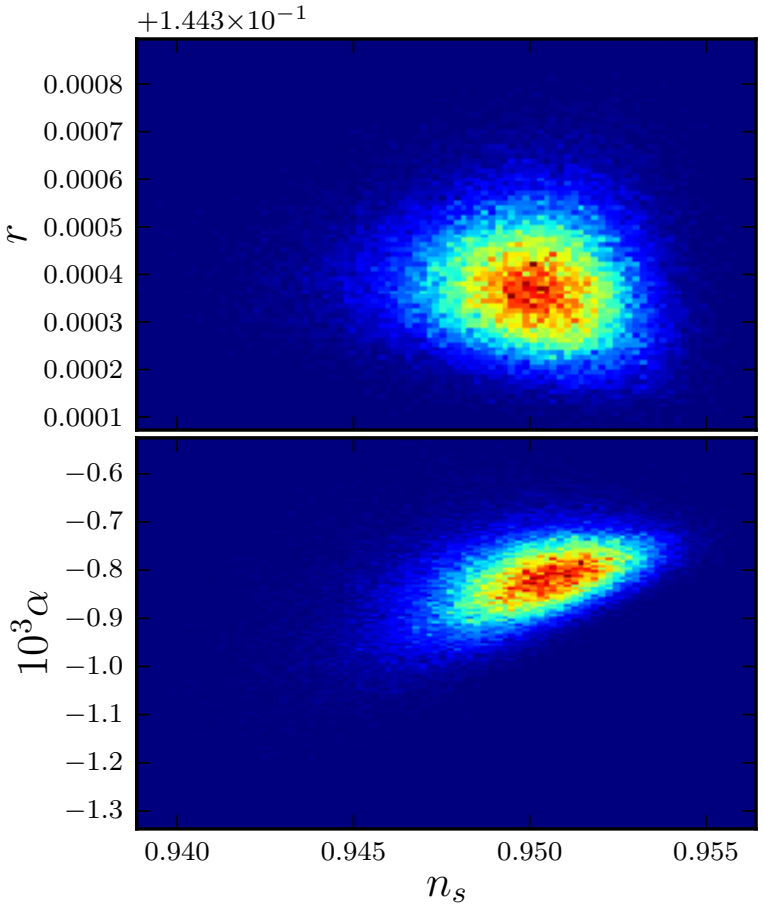

Figure 5.1: Histograms for $N = 100$ fields with the iso-E_0 prior at $E_0 = 0.1\,M_{\rm Pl}$ and masses from the Marčenko-Pastur distribution [89] with a maximum mass ratio of 1/8.08 and r is plotted relative to a baseline value of 0.1443. All observables are contained within a very small subvolume of the much larger range of possible values the model can yield, showing that it makes precise predictions for the values of the inflationary observables.

Each prior has a different physical justification and leads to significantly different distributions for the field values and velocities. For example, the iso-N_e prior near $N_e = 55$ implies we know nothing about the initial state when observable scales start to leave the horizon. By contrast, either (A) using the iso-E_0 prior with a relatively large initial energy; (B) requiring $N_e \gg 55$ for the iso-N_e prior; or (C) specifying a large field-space range for the slow-roll prior typically give solutions more scope to evolve into dynamically-favored regions of phase space, *e.g.*, slow-roll along the direction of the lightest field. Consequently, with these IC priors a higher proportion of trajectories find the attractors before the end of inflation. Conversely, the iso-N_e prior with $N_e \sim 55$ is the least predictive of these choices.

5.5 Multifield perturbations

We use MultiModeCode, as described in Chapter 2, which evolves the perturbation spectrum for an arbitrary potential, initial field values and velocities. MultiModeCode solves the 2-index mode equation [39, 49]

$$\psi''_{\alpha\beta} + (1-\epsilon)\psi'_{\alpha\beta} + \left(\frac{k^2}{a^2H^2} - 2 + \epsilon\right)\psi_{\alpha\beta} + \mathcal{M}_{\alpha\gamma}\psi_{\gamma\beta} = 0 \ , \tag{5.2}$$

where primes represent derivatives with respect to the number of e-folds, N_e; $\epsilon \equiv -\dot{H}/H^2$ is the slow-roll parameter; and $\psi_{\alpha\beta}$ is related to the Mukhanov–Sasaki variable, $u_\alpha \equiv a\delta\phi_\alpha$, by a sum over annihilation operators: $u_\alpha(\mathbf{k}, N) = \psi_{\alpha\beta}(\mathbf{k}, N)\hat{a}_\beta(\mathbf{k})$. Finally, the mass matrix is given by

$$\mathcal{M}_{\alpha\beta} = \frac{\partial_\alpha\partial_\beta V}{H^2} + \frac{\left(\phi'_\alpha\partial_\beta V + \phi'_\beta\partial_\alpha V\right)}{H^2} + (3-\epsilon)\phi'_\alpha\phi'_\beta, \tag{5.3}$$

where the Hubble parameter is $H^2 = V/(3-\epsilon)$.

For a mode k, we set the Bunch-Davies initial state for $\psi_{\alpha\beta}$ when $100k = aH$.

The power spectrum for the field perturbations $\delta\phi_\alpha$ is

$$\mathcal{P}_{\alpha\beta}(k) = \frac{k^3}{2\pi^2}\left(\frac{1}{a^2}\right)\psi_{\alpha\gamma}(k)\psi^*_{\beta\gamma}(k)\,, \tag{5.4}$$

where star denotes complex conjugation. We compute the power spectra for the comoving curvature perturbation $\mathcal{R}$ and isocurvature perturbations $\mathcal{S}$ via an appropriately-scaled projection onto directions parallel and perpendicular to the background trajectory. Consequently,

$$\mathcal{P}_\mathcal{R}(k) = \frac{1}{2\epsilon}\omega_\alpha\omega_\beta\mathcal{P}_{\alpha\beta}(k) \tag{5.5}$$

where $\omega_\alpha = \phi'_\alpha/\phi'_0$ projects onto the direction of the background trajectory for $\phi_0'^2 \equiv \phi'_\alpha\phi'_\alpha$. Directions perpendicular to ω are isocurvature directions, and can source superhorizon evolution of $\mathcal{R}$; we find the $(N-1)$ isocurvature vectors s_I by Gram-Schmidt orthogonalization. In analogy to $\mathcal{R}$, we define isocurvature perturbations $\mathcal{S}_I \equiv -(1/\phi'_0)s_{I\alpha}\delta\phi_\alpha$ with the spectrum

$$\mathcal{P}_\mathcal{S}(k) = \frac{1}{2\epsilon}\sum_{I,J}^{N-1} s_{I\alpha}s_{J\beta}\mathcal{P}_{\alpha\beta}(k)\,. \tag{5.6}$$

Conventionally, $\mathcal{P}_\mathcal{R}$ is characterized by an amplitude A_s and its logarithmic derivatives $\mathcal{D} = d/d\log k$ at the pivot scale k_*,

$$\mathcal{P}_\mathcal{R} = A_s\left(\frac{k}{k_*}\right)^{n_s-1+\frac{1}{2}\alpha\log k/k_*+\ldots} \tag{5.7}$$

with $n_s = \mathcal{D}\log\mathcal{P}_\mathcal{R}$ and $\alpha = \mathcal{D}^2\log\mathcal{P}_\mathcal{R}$. We can similarly describe $\mathcal{P}_\mathcal{S}$ or the adiabatic-isocurvature cross spectrum, although we report only the isocurvature-to-adiabatic ratio $r_{\rm iso} = \mathcal{P}_\mathcal{S}/\mathcal{P}_\mathcal{R}$. While MultiModeCode numerically computes the full functional form of $\mathcal{P}_\mathcal{R}(k)$ and $\mathcal{P}_\mathcal{S}(k)$, for convenience n_s and α are computed by central finite differences near $k_{\rm piv}$. Finally, we compute the tensor-to-scalar ratio r by evolving the appropriately-normalized tensor perturbations.

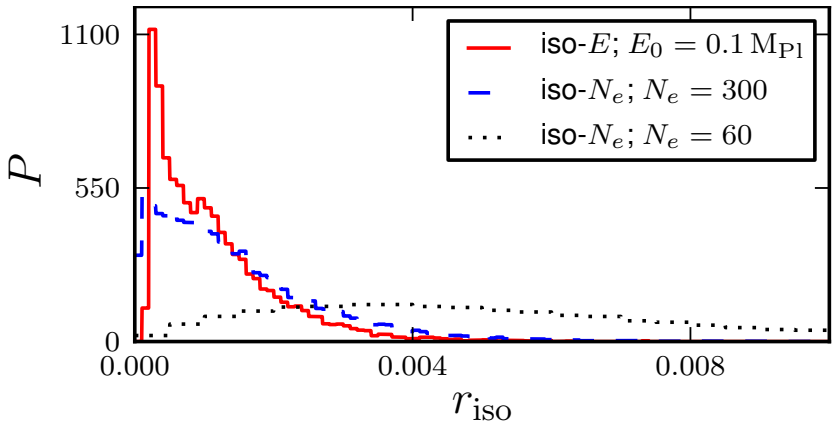

Figure 5.2: Density function of isocurvature fraction $r_{\rm iso} = \mathcal{P}_{\mathcal{S}}/\mathcal{P}_{\mathcal{R}}$ for different initial condition priors with $N = 100$ fields. The average $r_{\rm iso}$ roughly decreases with increasing number of e-folds between the surface on which we specify the IC and the end of inflation, implying the heavier masses find their minima more often when given more time to evolve before inflation ends.

5.6 Results

Figs. 5.1–5.3 show histograms for n_s, α, r, and $r_{\rm iso}$, with Scott-binning [187] for the iso-E_0 prior with $E_0 = 0.1\,M_{\rm Pl}$. Fig. 5.4 is the histogram-estimated PDF for n_s for different IC priors. The slow-roll prior yields results that are effectively indistinguishable from the iso-E_0 prior and are not plotted. We sample $\mathcal{O}(10^6)$ ICs for $N = \{2, 3\}$ fields and $\mathcal{O}(10^4)$ ICs for $N = 100$.

Fig. 5.1 shows the first-ever general predictions for n_s, α, and r for inflation with $N = \mathcal{O}(100)$ light fields. Using the iso-E_0 prior, we find that 95% of Monte Carlo samples are in the ranges: $n_s \in (0.9455, 0.9534)$; $\alpha \in (-9.741, -7.047) \times 10^{-4}$; $r \in (0.1445, 0.1449)$; and $r_{\rm iso} \in (0.02137, 3.510) \times 10^{-3}$, which is similar to the predictions of this model in the single-field limit. Crucially, while many-field N-quadratic inflation supports a broader range of *possible* observables, it nevertheless makes a sharp *generic* prediction for n_s, α, and r.

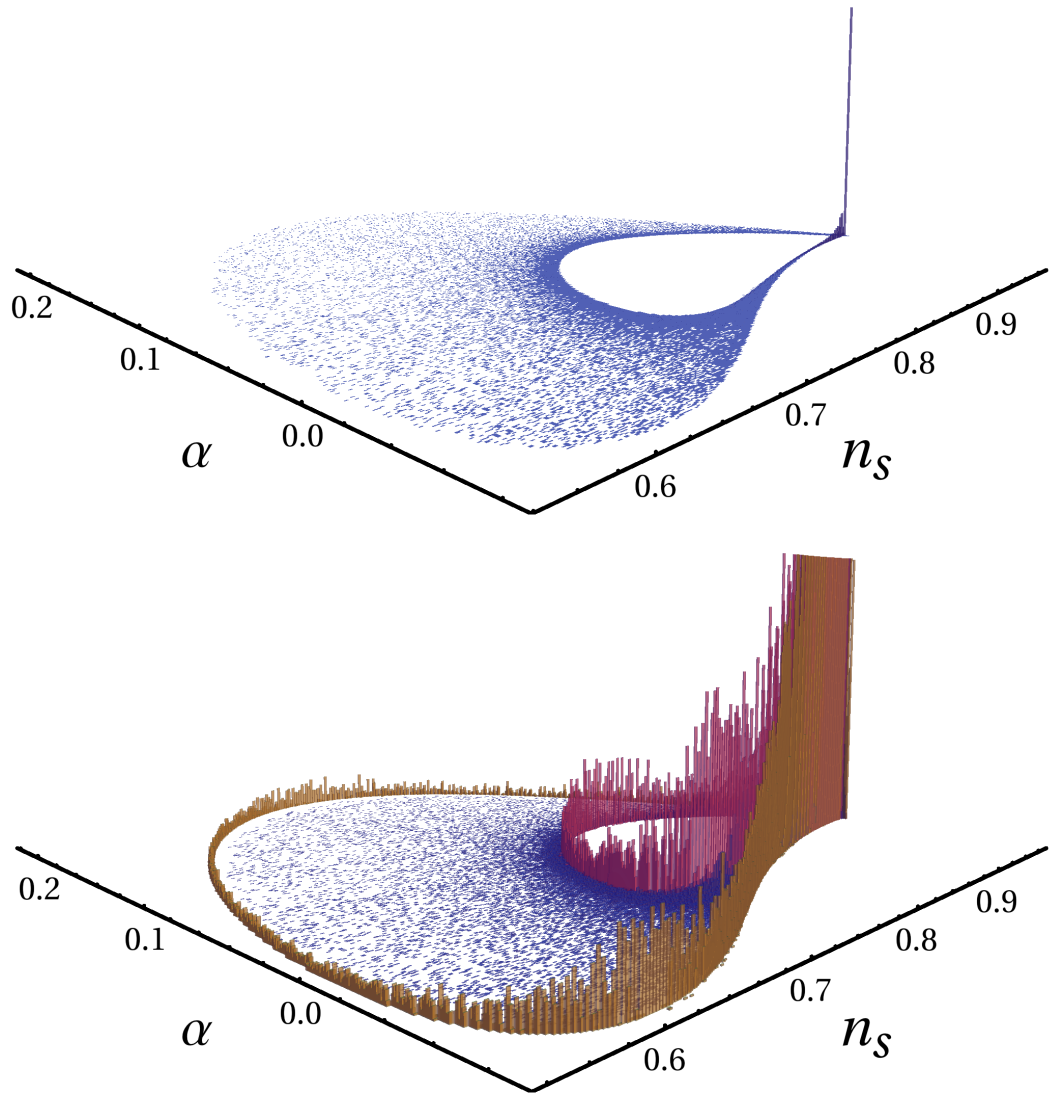

Figure 5.3: Histograms for the spectral index n_s and running α for N-quadratic inflation with equal-energy initial conditions at $E_0 = 0.1\,M_{\rm Pl}$. (Top) Three fields with mass ratios $m_i/m_1 = \{1, 7, 9\}$; (Bottom) comparison between three fields (blue; masses as above) and two fields with mass ratio $m_2/m_1 = 7$ (red; inner contour) and $m_2/m_1 = 9$ (gold; outer contour). The bottom figure emphasizes the outlying regions and does not show the full range. All sampled distributions have a peak near $n_s = 0.963$ and $\alpha = -7 \times 10^{-4}$, with appreciable deviation only in the tails.

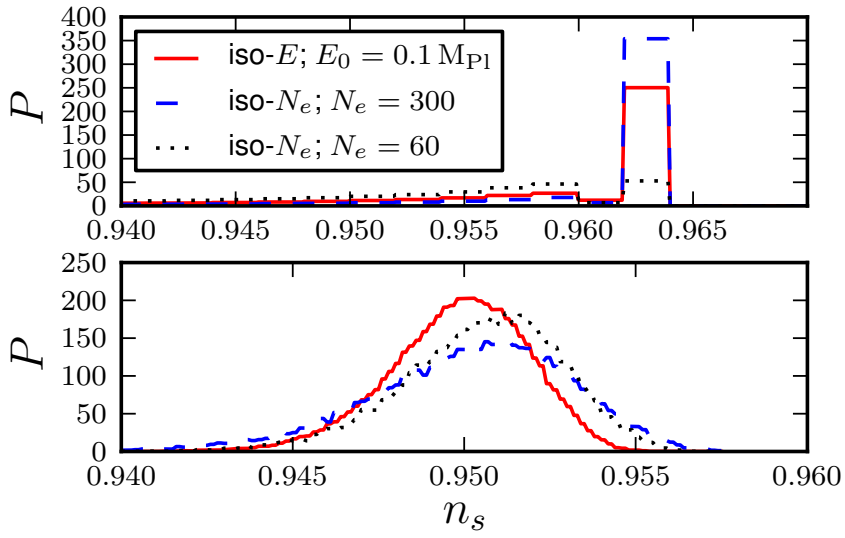

Figure 5.4: Probability distribution for (top) $N = 3$ fields and (bottom) $N = 100$ fields with different initial conditions (ICs) priors. The slow-roll prior, which overlaps the iso-E_0 prior, has not been plotted. Importantly, the upper plot shows only the peak in the PDF and the full range for n_s has not been plotted. The distributions show remarkable consistency, despite significantly different IC priors.

The $r_{\rm iso}$ component is significant with $N = 100$ fields for the two- and three-field cases. The sensitivity of $r_{\rm iso}$ on the choice of IC prior is shown in Fig. 5.2. The isocurvature fraction is largest for the iso-$N_e = 60$ prior, reflecting the relatively short period this models has to evolve before inflation ends. The average number of total e-folds for the iso-$E_0 = 0.1\,M_{\rm Pl}$ prior is $N_e = 306.6$, and the average $r_{\rm iso}$ roughly decreases with increasing total number of e-folds. Unlike the case of a few fields, the heavier fields do not always reach their minima before inflation ends, although they approach their minima given more time to evolve. Trajectories are therefore typically turning in field-space at the end of inflation, and it is known [41, 46, 135, 188] that this causes the isocurvature modes to grow. We attribute the increase in $r_{\rm iso}$ to these dynamical effects.

Fig. 5.3 shows the PDFs for the observables for $N = 3$ with an iso-E_0 prior with $E_0 = 0.1\,M_{\rm Pl}$. The PDFs have spikes in the bin $n_s \in (0.962, 0.964)$ and $\alpha \in (-0.001, -0.0005)$, which contains 48.8% of the Monte Carlo samples. With $N = 2$ we find contours in the (n_s,α)–plane, reproducing the analytic result of Ref. [42]. For three fields the distribution is bounded by the same contours, with a lower weighting around the outer contour (with $m_2/m_1 = 9$). Typical trajectories become effectively single field before the end of inflation and hence isocurvature modes decay, giving negligible $r_{\rm iso}$.

To explicitly compare different IC priors, Fig. 5.4 plots the prediction for n_s, the observable best-constrained by *Planck*. For many fields, the distributions are largely similar and are well-described near the maximum by Gaussians with means $\mu = (0.950, 0.951, 0.951)$ and variances $\sigma^2 = (1.97, 2.81, 2.24) \times 10^{-3}$, for the iso-$E_0$, iso-$N_e = 300$, and iso-$N_e = 60$ priors, respectively.

With fewer fields, we see larger differences in the PDFs. Nevertheless, the bin containing maximum probability mass coincides and all the PDFs have the same overall shape. For the iso-E_0 and iso-$N_e = 300$ priors the probability-mass lies in a small range of observable-space, giving essentially the same prediction. Furthermore, as seen in Fig. 5.3, the outlying contours non-trivially constrain the joint prediction for (n_s, α). For these two IC priors, the PDFs in Fig. 5.4 do not change drastically.

However, the iso-$N_e = 60$ prior (which is the least predictive choice *a priori*) has a significantly lower peak in Fig. 5.3 and 95% of Monte Carlo samples in the broad range $n_s \in (0.675, 0.963)$, which is comparable to the full range of predictions for this model, $n_s \in (0.543, 0.964)$. Interestingly, this IC prior yields significant mass below the most probable value of $n_s = 0.963$, and may thus perform far worse relative to the other IC priors in a Bayesian evidence calculation, as the 68% *Planck* bounds are $n_s \in (0.954, 0.973)$. This implies

that *Planck* data may constrain the initial states when N is small.

5.7 Discussion

This chapter presents a complete analysis of multifield quadratic inflation. We numerically integrate the multifield mode equations through to the end of inflation, the first time this task has been performed for a model with many degrees of freedom. We compute PDFs for key observables, and evaluate their sensitivity to priors for the initial field values and velocities.

We find that the initial conditions are not "stiff parameters" [189–191] for which small changes radically alter observables, demonstrating that this model makes sharp, robust predictions for the inflationary parameters. Given that multifield models can produce a wide range of perturbation spectra, one may specify an IC prior for which the observables are far from the peak values in the PDF found here. However, such scenarios are typically contrived, so the corresponding prior is unlikely to be physically compelling. Moreover, even with one field, initial conditions which violate slow-roll near $N_e = 60$ yield a $\mathcal{P}_\mathcal{R}$ that differs significantly from the usual result.

The matching between the number of e-folds and present-day scales depends on the post-inflationary equation of state [32, 33, 192]. This resulting uncertainty in n_s and other observables scales with α and is comparable to the width of the large-N PDFs computed here. Consequently, the spread in the predictions of the inflationary observables at large N — including the ambiguity associated with the IC prior — need not be the dominant source of theoretical uncertainty in multifield models.

For $N = 100$ the isocurvature modes are potentially nontrivial. This is a new and significant result: the presence of isocurvature modes implies that

the curvature perturbation may continue to evolve until an adiabatic limit is reached [46, 63, 76, 193, 194], even if this is after the end of inflation. However, the most probable values for the power spectra observables *at the end of inflation* are still concentrated in small regions. Recent studies of the evolution of observables during reheating focus on models with only a few fields [41, 195–197]. Given the magnitude of the $r_{\rm iso}$ for $N = 100$, it will be important to examine the reheating dependence of observables at large N, for which a non-zero $r_{\rm iso}$ may be generic.

With $N = 100$, the central values we find for n_s, r and α are consistent with those seen in previous work [89–91, 93] based on slow-roll expressions. If the duration of inflation is increased by changing the initial conditions while other parameters are held fixed, $r_{\rm iso}$ is reduced, consistent with Fig. 5.2. However, there is no generic mechanism that forces the initial values of $\dot{\phi}_i$ to be small (as noted in Chapter 3) and, with the exception of our *slow roll prior*, we start our simulations with significant field velocities, in contrast to previous work. This reduces the duration of inflation at fixed initial energy, and increases the likelihood of seeing a nontrivial value of $r_{\rm iso}$.

Importantly, our results suggest that the curvature perturbation of multi-field inflationary models has a well-defined large-N limit. Consequently, these models may be least predictive when $N = 2$ or 3. This situation mirrors that found elsewhere [89, 133] and can be understood by analogy with the central limit theorem. Determining the extent to which this phenomenon is generic in N-field inflation is clearly of the utmost importance. Finally, this analysis points the way to constraining multifield scenarios with data from observational surveys, such as *Planck*.

Chapter 6

Gravitational Wave Consistency Relations

This chapter is adapted from:

L. C. Price, H. V. Peiris, J. Frazer, and R. Easther

Gravitational wave consistency relations for multifield inflation

Phys. Rev. Lett. 114 (2014) 031301, [198]

6.1 Abstract

We study the tensor spectral index n_t and the tensor-to-scalar ratio r in the simplest multifield extension to single-field, slow-roll inflation models. We show that multifield models with potentials $V \sim \sum_i \lambda_i |\phi_i|^p$ have different predictions for n_t/r than single-field models, even when all the couplings are equal $\lambda_i = \lambda_j$, due to the probabilistic nature of the fields' initial values. We analyze well-motivated prior probabilities for the λ_i and initial conditions to make detailed predictions for the marginalized probability distribution of n_t/r. With $\mathcal{O}(100)$ fields and $p > 3/4$, we find that n_t/r differs from the single-field result of $n_t/r = -1/8$ at the 5σ level. This gives a novel and testable prediction for the simplest multifield inflation models.

6.2 Introduction

A cosmological gravitational wave background (CGWB) is a compelling signature of inflation, which is already supported by the highly Gaussian primordial perturbations [150, 180] and their broken scale invariance, now detected at 5σ significance [18, 19]. A large-amplitude CGWB provides fundamentally new tests of single-field slow-roll (SFSR) inflation via the *consistency relation* [14, 15] $n_t/r = -1/8$, which relates the tensor spectral index n_t to the ratio of the tensor and scalar perturbation amplitudes, r.

While there has been dramatic progress towards the direct detection of a CGWB through the B-mode polarization in the cosmic microwave background (CMB) [199], measuring n_t is challenging with current technologies [200–202]. However, for $r \gtrsim 0.1$ this will be feasible with the next generation of space-based [203, 204], ground-based [205–208], and balloon-borne [209, 210] experiments, while future 21 cm projects [211, 212] could also detect lensing by a CGWB and direct detection experiments [**?**, 213] would test the consistency condition using the lever arm between CMB and solar system scales to far greater accuracy with $r \gtrsim \mathcal{O}(10^{-3})$.

The simplest inflationary scenarios that yield an easily detectable CGWB are *monomial* models with the inflationary potential $V \sim |\phi|^p$, which have $0.05 \lesssim r \lesssim 0.30$ for $2/3 \lesssim p \lesssim 4$. Single field models are *simple* but not necessarily *natural*, as many high energy theories yield large numbers of scalar degrees of freedom [162–165]. For multifield models the consistency relation is reduced to an inequality, $n_t/r \leq -1/8$. While r and n_t are correlated for $N_f = 2$ [61, 62], there is no known relationship between r and n_t when N_f is large.

In this chapter, we derive a robust prediction for n_t/r for N_f*-monomial*

models, with potential

$$V = \frac{1}{p}\sum_i \lambda_i |\phi_i|^p, \tag{6.1}$$

where λ_i are real, positive constants and summations run over the number of fields, N_f. Eq. (6.1) arises naturally in many high energy theories [85–87, 87–91, 93] and is a simple, intuitive generalization of the chaotic SFSR models.

We treat the λ_i and the values of ϕ_i at a fixed number of e-folds before the end of inflation as independent random variables. When $N_f \to \infty$, the central limit theorem ensures that n_t/r is a Gaussian random variable. Critically, $\langle n_t/r \rangle$ does not reduce to the single-field limit if the couplings are identical unless the field values $\phi_{i,*}$ when the pivot scale k_* leaves the horizon are also fixed, except for the special case $p = 2$. The expected value of n_t/r depends only on two moments of the distributions of the λ_i and ϕ_i, and is independent of N_f. The variance in n_t/r is $s^2_{n_t/r} \sim 1/N_f$ (for $p > 3/4$), giving a sharp, generic prediction for the consistency relation in the many-field limit. This provides a direct test for distinguishing between N_f-monomial models and their single-field analogues.

6.3 Model

In some cases the λ_i in Eq. (6.1) might be derivable from fundamental theory, but in general we are ignorant of their values, so we treat these terms as independent random variables (RVs) with a prior probability $P(\lambda)$. Similarly, we do not know the fields' initial conditions, so we also treat these as identically distributed, but possibly correlated, RVs with a prior probability $P(\phi_0)$. We then marginalize over the $P(\lambda)$ and $P(\phi_0)$ to produce a probability distribution for n_t/r. Since a change of variables $\phi_i \to \tilde{\phi}_i(\phi_j, \lambda_j)$ will mix the λ_i and ϕ_i, it is clear that there is no *a priori* difference between these two types of parameters,

motivating our statistical approach.

The simplest choice for $P(\phi_0)$ is a uniform distribution of $\phi_{i,*}$ defined when the pivot scale k_* leaves the horizon N_* e-folds before the end of inflation. This choice contains the least Shannon information about the fields' initial states and ensures that most of the fields are dynamically relevant. Further, this $P(\phi_0)$ and others were extensively studied in Chapter 5, where it was shown that the initial conditions only weakly affect the predicted density spectra. The likely values of n_s and r for a related class of multifield monodromy models was derived in Ref. [94], finding $0.955 \lesssim n_s \lesssim 0.975$. Furthermore, $r = 4p/N_*$, and the non-Gaussianity is small.

6.4 δN formalism

The potential in Eq. (6.1) is sum-separable and, assuming slow-roll, N_* is [73, 74]

$$N_* = -\int_*^c \sum_i \frac{V_i}{V_i'} d\phi_i, \tag{6.2}$$

where $V_i' = \lambda_i |\phi_i|^{p-1}$ and $\phi_{i,*}$ and $\phi_{i,c}$ denote field values at horizon crossing and the end of inflation, respectively. For N_f-monomial inflation

$$N_* = \frac{1}{2p} \sum_i \left[\phi_{i,*}^2 - \phi_{i,c}^2\right]. \tag{6.3}$$

The δN formalism relates the field perturbations at horizon crossing to the gauge-invariant curvature perturbation ζ on constant density hypersurfaces via

$$\zeta \approx \sum_i N_{*,i} \delta\phi_{i,*}, \tag{6.4}$$

where $N_{*,i} \equiv \partial N_*/\partial \phi_{i,*}$. If the field perturbations are well-approximated by a free field theory with power spectrum $\mathcal{P}_{\delta\phi}^{ij} = (H_*/2\pi)^2 \delta^{ij}$ at horizon crossing,

the tensor-to-scalar ratio is

$$r = \frac{8}{\sum_i N_{*,i} N_{*,i}}. \tag{6.5}$$

To first-order in slow-roll $n_t = -2\epsilon$, where

$$\epsilon = \frac{1}{2} \sum_i \left[\frac{V_i'}{V} \right]^2 . \tag{6.6}$$

For N_f-monomial models, the field values $\phi_{i,c}$ at the end of inflation can typically be neglected. This *horizon crossing approximation* (HCA) (*e.g.*, Refs. [73, 92]) is a simplification of the δN formalism that incorporates the super-horizon evolution of ζ, but ignores quantities contributing to N_* from the end-of-inflation surface. Setting $\phi_{i,c} \to 0$ in Eq. (6.3), we find

$$\frac{n_t}{r} = -\frac{1}{4p^2} \epsilon \sum_i \phi_{i,*}^2 , \tag{6.7}$$

where we restrict our attention to cases that are slowly rolling at horizon crossing. Requiring $\epsilon \lesssim 0.1$ then sets the maximum deviation from the single-field result as

$$-\left(\frac{N_*}{2p}\right) \times \mathcal{O}(10^{-1}) \lesssim \frac{n_t}{r} \leq -\frac{1}{8}. \tag{6.8}$$

6.5 The many-field limit

We build the probability distribution for n_t/r by marginalizing Eq. (6.7) over $P(\phi_0)$ and $P(\lambda)$, and use the central limit theorem (CLT) to take the large N_f limit, $N_f \to \infty$. By Eq. (6.3) the HCA implies that $P(\phi_0)$ is a uniform distribution pulled back onto an N_f-sphere in field-space with radius $\sqrt{2pN_*}$. Since the multivariate normal distribution $\vec{x} \sim \mathcal{N}(0, \vec{1})$ is invariant under rotations of $\vec{x}$, we can sample this N_f-sphere uniformly by defining

$$\phi_{i,*} = \sqrt{\frac{2pN_*}{\sum_j x_j^2}}\, x_i \quad \text{for} \quad \vec{x} \sim \mathcal{N}(0, \vec{1}). \tag{6.9}$$

Using Eq. (6.9), the summations in Eqs. (6.6) and (6.7) are

$$\sum_i \lambda_i^n |\phi_{i,*}|^m = \sum_i \lambda_i^n \left[\frac{2pN_*}{\sum_j x_j^2}\right]^{\frac{m}{2}} |x_i|^m. \tag{6.10}$$

As $N_f \to \infty$ the CLT shows that the numerator is normally distributed with mean

$$\mu_{\rm num} = N_f \left(2pN_*\right)^{m/2} \langle \lambda^n \rangle \langle |x|^m \rangle \tag{6.11}$$

and standard deviation

$$s_{\rm num} = \sqrt{N_f} \left(2pN_*\right)^{m/2} \sigma_{n,m}, \tag{6.12}$$

where $\langle . \rangle$ indicates expected value and

$$\sigma_{n,m}^2 \equiv \left\langle \lambda^{2n} \right\rangle \left\langle |x|^{2m} \right\rangle - \langle \lambda^n \rangle^2 \langle |x|^m \rangle^2, \tag{6.13}$$

which assumes that the λ_i and x_j are independent. Finally, the denominator in Eq. (6.9) is drawn from the χ-distribution, which is closely approximated by $\mathcal{N}(\sqrt{N_f}, 1/\sqrt{2})$ for $x_i \sim \mathcal{N}(0,1)$.

The numerator and denominator in Eq. (6.10) are correlated by the constraint in Eq. (6.3). For a given variance in $P(\lambda)$, the correlation γ is maximized when $m = 2$ and $|\gamma| \to 1$ as the variance vanishes. Since each $\sum_i \lambda_i^n |\phi_{i,*}|^m$ is uniquely determined given $\vec{\lambda}$ and $\vec{\phi}_*$, we expect a strong correlation between the numerator and denominator in Eq. (6.6) for typical choices of $P(\lambda)$. This significantly reduces the variance of n_t/r, and ensures a sharp prediction for its value. We numerically calculate γ after defining the priors on λ.

For any normally distributed variable $y \sim \mathcal{N}(\mu, \sigma)$

$$\langle |y|^m \rangle = \frac{2^{\frac{m}{2}} \sigma^m}{\sqrt{\pi}} \Gamma\left(\frac{1+m}{2}\right) F_{1,1}\left(\frac{-m}{2}; \frac{1}{2}; \frac{-\mu^2}{2\sigma^2}\right), \tag{6.14}$$

for $m > -1$, and $F_{1,1}$ is the confluent hypergeometric function of the first kind. If $\mu = 0$, as for $x_i \sim \mathcal{N}(0,1)$, then $F_{1,1} = 1$ and only the Γ function contributes to the moments.

If $m < -1$, $\langle |y|^m \rangle$ may diverge if $P(y = 0)$ does not vanish fast enough. This is indeed the case for $x_i \sim \mathcal{N}(0, 1)$, and we cannot predict the distribution of the sums in Eq. (6.10) with $m \leq -1$. Sums like Eq. (6.10) are effectively finite numerical approximations to the integral

$$\frac{1}{N_f} \sum_i \lambda_i^n |x_i|^m \approx \int |x|^m \mathcal{N}(0,1) dx \int \lambda^n P(\lambda) d\lambda, \tag{6.15}$$

which diverges for $m < -1$. While ratios of these sums might be well-defined [42], our approach shows that a finite prediction for both the mean and the standard deviation of n_t/r requires $p > 3/4$, while only requiring a finite mean needs $p > 1/2$, using the CLT.

6.6 The method

Since n_t/r is given by Eq. (6.7) and the sums in Eq. (6.10) are ratios of correlated, normally distributed RVs, the key tool for this analysis is the ratio distribution $f_{\text{ratio}}(\alpha/\beta)$ for normally distributed RVs α and β. If $w \equiv \alpha/\beta$, then as $P(\beta > 0) \to 1$ the CDF for the ratio distribution $f_{\text{ratio}}(w)$ is approximately [214]

$$F_{\text{ratio}}(w) = \Phi\left[\frac{\mu_\beta w - \mu_\alpha}{\sigma_\alpha \sigma_\beta a(w)}\right], \tag{6.16}$$

where μ_i and σ_i^2 are the respective means and variances,

$$a(w) \equiv \left[\frac{w^2}{\sigma_\alpha^2} - \frac{2\gamma w}{\sigma_\alpha \sigma_\beta} + \frac{1}{\sigma_\beta^2}\right]^{1/2}, \tag{6.17}$$

and

$$\Phi(z) \equiv \frac{1}{2}\left[1 + \text{Erf}\left(\frac{z}{\sqrt{2}}\right)\right] \tag{6.18}$$

for real z. When N_f is large, f_{ratio} approaches a normal distribution with mean μ_α/μ_β and standard deviation

$$s = \frac{\sqrt{\mu_\beta^2 \sigma_\alpha^2 - 2\gamma \mu_\alpha \mu_\beta \sigma_\alpha \sigma_\beta + \mu_\alpha^2 \sigma_\beta^2}}{\mu_\beta^2}. \tag{6.19}$$

The mean of $f_{\rm ratio}$ is independent of the correlations γ, and the standard deviation for n_t/r is a straightforward — but messy — algebraic function of $\langle\lambda\rangle$, $\langle\lambda^2\rangle$, and $\langle\lambda^4\rangle$, as well as $\langle|x|^m\rangle$ for $m = 2, 4, p, 2p, 2p-2$, and $4p-4$.

To obtain the distribution $f_{\rm ratio}(n_t/r)$ we express the consistency relation in terms of the sums in Eq. (6.10) as

$$\frac{n_t}{r} = -\frac{pN_*}{4}\left[\frac{\sum_i \lambda_i^2|\phi_{i,*}|^{2p-2}}{\left(\sum_j \lambda_j|\phi_j|^p\right)^2}\right]. \tag{6.20}$$

For each sum above, we calculate the covariance in Eq. (6.10) between the numerator and denominator given $P(\lambda)$, and use Eq. (6.19) to find the variance of the sum. Although the denominator $(\sum_i \lambda_i|\phi_{i,*}|^p)^2$ is then χ^2-distributed, this is approximately normal in the many-field limit. We then substitute these two normally-distributed RVs back into Eq. (6.16). Similarly, we evaluate the correlation between the numerator and denominator in Eq. (6.20), finally obtaining the probability distribution for n_t/r.

6.7 Novel multifield predictions

From the ratio distribution (6.16), as $N_f \to \infty$ the value of n_t/r in Eq. (6.20) is normally distributed with a mean

$$\left\langle\frac{n_t}{r}\right\rangle_{N_f\uparrow} = \left[-\frac{1}{8}\right]\left[\frac{\langle\lambda^2\rangle}{\langle\lambda\rangle^2}\right]\left[\frac{\sqrt{\pi}\,\Gamma\left(p-\frac{1}{2}\right)}{2\,\Gamma^2\left(\frac{p+1}{2}\right)}\right] \tag{6.21}$$

and a standard deviation proportional to

$$s_{n_t/r} \propto \frac{1}{\sqrt{N_f}} \to 0 \quad \text{as} \quad N_f \to \infty, \tag{6.22}$$

which can be found by substituting the means, variances, and correlations of Eq. (6.10) into Eq. (6.19).

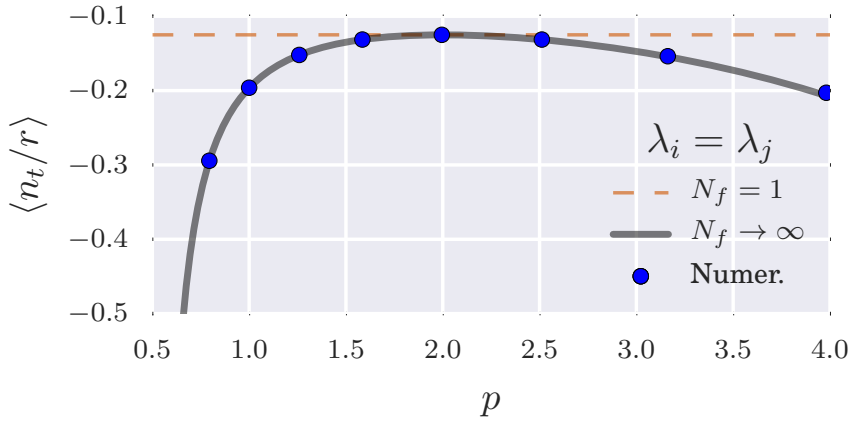

Figure 6.1: The multifield prediction from Eq. (6.21) compared to the numerical mean $\langle n_t/r \rangle$ of simulations with 5000 samples, at each plotted value of p, with $N_f = 1000$ using the horizon-crossing approximation. The field values $\phi_{i,*}$ as the pivot scale k_* leaves the horizon are drawn from a uniform prior on the surface in Eq. (6.3) and all the couplings λ_i are identical.

The first bracketed term in Eq. (6.21) is the single-field prediction, the second is due to the couplings λ_i, and the third arises from the uniform prior for $\phi_{i,*}$ on the horizon-crossing surface. This last term is due only to the spread in the field values at horizon crossing and is independent of everything except p. The functional form of this term is fixed by the uniform prior distribution on the horizon crossing surface, but other prior probabilities for $\phi_{i,*}$ result in qualitatively similar behavior as demonstrated in Chapter 5. As Eq. (6.22) vanishes in the many-field limit, Eq. (6.21) is the generic multifield prediction, which deviates from the single-field result at $> 5\sigma$ for $N_f \gtrsim \mathcal{O}(10^2)$ for typical $P(\lambda)$.

Consequently, even if $\langle \lambda^2 \rangle = \langle \lambda \rangle^2$, N_f-monomial models do not predict $n_t/r = -1/8$, unless the $\phi_{i,*}$ are also identical. Fig. 6.1 compares the predicted value for $\langle n_t/r \rangle$ in Eq. (6.21), with all λ_i equal, to numerical results obtained by directly evaluating n_t/r with Eq. (6.7), showing excellent agreement for many

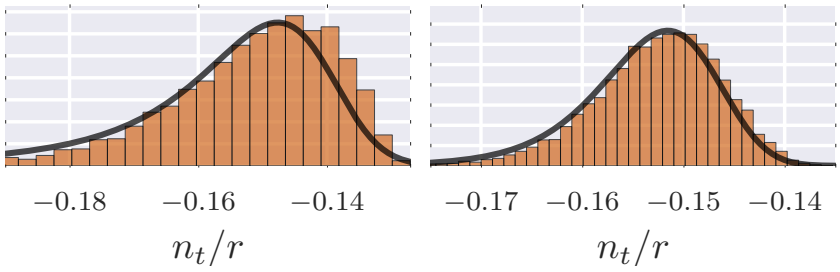

Figure 6.2: Predicted probability distributions for n_t/r with $p = 2$ compared with histograms built from 10000 numerical samples. The couplings λ_i are drawn from the Uniform Model with (*left*) $N_f = 20$ and (*right*) $N_f = 100$. For $N_f \lesssim \mathcal{O}(10^2)$, the distribution is skewed toward positive values as predicted.

fields. The divergence at $p = 1/2$ reflects the fact that $\langle |x|^{2p-2} \rangle \to \infty$. Thus, when $p \leq 1/2$, $\langle n_t/r \rangle$ may be arbitrarily large, which violates the slow-roll assumption. Consequently, these models are most easily distinguished from their single field analogues, but the hardest to make accurate predictions for.

6.8 Specific examples

To understand how the mean $\langle n_t/r \rangle$ in Eq. (6.21) is affected by $P(\lambda)$ we compare two explicit priors that are widely used in Bayesian analyses of inflation [19, 31–33, 215]. We focus on the $p = 2$ case, since the dependence on the prior on $\phi_{i,*}$ in Eq. (6.21) cancels for this scenario.

We look at two cases: uniform prior probabilities over λ_i or α_i for $\lambda_i \equiv 10^{\alpha_i}$, which we denote the *Uniform Model* and *Log Model*, respectively. The Uniform Model would be applicable when the relevant scale of λ_i is known to within an order of magnitude, while the Log Model effectively scans over a range of physical scales. The Log Model is invariant with respect to a change in scale for λ_i and is equivalent to the Jeffreys prior [216], which is commonly used in Bayesian analyses.

For the Uniform Model, the λ_i are drawn from $\mathcal{U}[a,b]$, and Eq. (6.21) becomes

$$\left(\frac{n_t}{r}\right)^{\rm unif}_{p=2} = -\frac{1}{6}\left[\frac{b^2+ab+a^2}{(b+a)^2}\right]. \tag{6.23}$$

For $\lambda_i \in [10^{-14}, 10^{-13}]$, as $N_f \to \infty$ the predicted correlation coefficient for $f_{\rm ratio}(n_t/r)$ is $\gamma \approx -0.98$ and $\langle n_t/r\rangle = -0.153$. We plot $f_{\rm ratio}$ and the results of 10000 numerical realizations using the HCA in Fig. 6.2. We find excellent agreement with Eq. (6.23), with $f_{\rm ratio}$ accurately capturing the higher order moments of the n_t/r distribution for $N_f \gtrsim 20$. For $p = \{3/2, 2, 3\}$ the single-field result $n_t/r = -1/8$ is a 5σ deviation from the mean in Eq. (6.23) for $N_f \gtrsim \{120, 120, 200\}$, respectively.

For the Log Model with $\alpha \sim \mathcal{U}[a,b]$,

$$\left(\frac{n_t}{r}\right)^{\log}_{p=2} = -\frac{\log(10)(b-a)}{16}\left[\frac{10^b+10^a}{10^b-10^a}\right]. \tag{6.24}$$

If $a \to b$, we recover the single-field result in both Eqs. (6.23) and (6.24). However, Eq. (6.24) diverges as $a \to -\infty$, reflecting the failure of slow-roll in the limit of widely separated scales. For $\alpha \in [-14, -12]$ the Log Model predicts $\mathcal{P}_\zeta \sim \mathcal{O}(10^{-9})$, $\epsilon \lesssim 0.03$, $\gamma \approx -0.95$ and $n_t/r = -0.294$. For $p = \{3/2, 2, 3\}$ the single-field result is a 5σ deviation from the mean in Eq. (6.24) for $N_f \gtrsim \{145, 135, 255\}$, respectively.

6.9 Relaxing the approximations

Fig. 6.3 compares the HCA prediction to numerical results that include the contribution from the end-of-inflation surface in Eq. (6.3), with $\phi_{i,c} \neq 0$. We numerically solve the background Klein-Gordon equations for 1000 realizations, finding the field values at the end of inflation (defined by $\epsilon = 1$) and obtaining the full δN prediction without using the HCA. Fig. 6.3 also incorporates

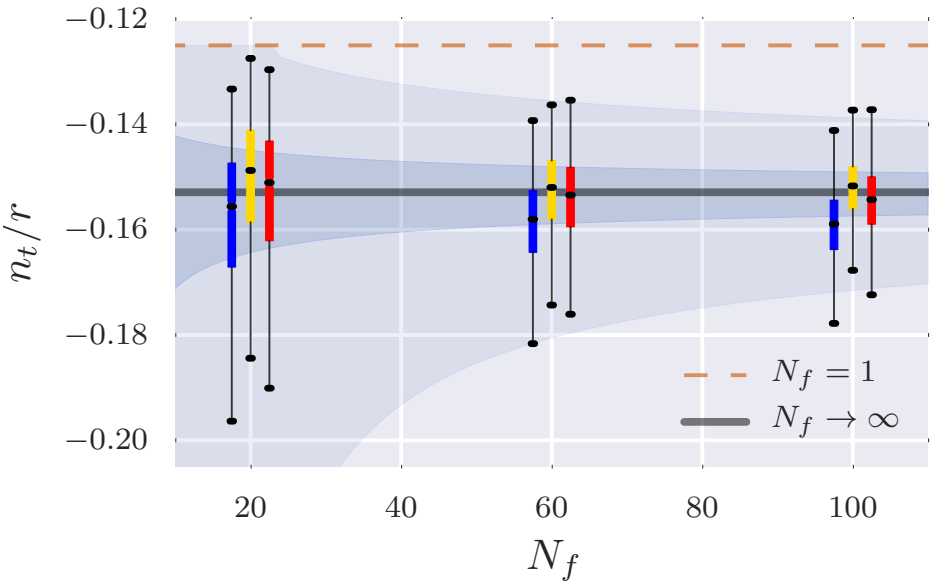

Figure 6.3: The consistency relation for the Uniform Model with $p = 2$ is plotted for different N_f, marginalizing over initial field values. The boxes/whiskers cover the 50/97% CIs and the gray regions delineate the same ranges as predicted by the HCA and the central limit theorem. The (*dashed*) brown and (*solid*) gray lines are the single-field and the many-field HCA predictions, respectively. For each case we present results derived from full numerical solutions to the mode equations (*blue/left*), the slow-roll prediction using the HCA (*yellow/center*), and the slow-roll prediction including the end-of-inflation surface (*red/right*) for $N_f = 20$, 60, and 100.

both the sub-horizon evolution of the modes and any non–slow-roll behavior by solving the mode equations numerically, as in Ref. [49] and Chapter 5, using MultiModeCode [16]. Results are plotted for the Uniform Model, with the ranges $\lambda_i \in [10^{-14}, 10^{-13}]$ and $p = 2$.

In all cases the numerical results are well-approximated by the HCA. The HCA results are marginally larger than the numerical results, which we attribute to second-order corrections to the slow-roll equations; $n_t = -2\epsilon/(1-\epsilon)$, which suppresses n_t relative to the first-order approximation. The variances in

the numerical results scale as $\sigma^2 \propto 1/\sqrt{N_f}$, as predicted by the HCA results, confirming that many-field models make sharp predictions for n_t/r.

6.10 Conclusion

We have computed the probability distribution for the consistency relation n_t/r for inflation driven by multiple scalar fields with monomial potential terms, as a function of the distribution of couplings and initial field values. The single-field result is clearly distinguishable from the many-field limit, providing a clean and compelling signature that distinguishes these models from their single-field analogues. Other than for the quadratic case, this result holds even when the couplings are identical.

We focused on computing the slow roll parameter ϵ, but the nature of the slow-roll hierarchy [217] indicates that this approach will generalize to a variety of observables, so quantities such as $f_{\rm NL}$ that rely on the second and higher slow-roll parameters should also have precise predictions that deviate from the single-field expectation even when the couplings are degenerate. This provides a further compelling example of a multifield scenario in which the observables have a sharp and *generic* prediction in the many-field limit [42, 45, 79, 89, 91–93, 133, 181–184, 218, 219].

The expected value $\langle n_t/r \rangle$ depends on only two moments of the prior probability distributions $P(\lambda)$ and $P(\phi_0)$, and the corresponding variance is $s^2_{n_t/r} \propto 1/N_f$. The single-field expectation of $n_t/r = -1/8$ differs from the multifield result at the 5σ level when $N_f \gtrsim \mathcal{O}(10^2)$. Consequently, given specific priors for the field values and couplings, we obtain generic and testable predictions for the consistency relations in this large and interesting class of multifield inflation models.

PART V

Conclusion

Chapter 7

Conclusion

This thesis has taken a joint numerical and analytical approach to studying the background and perturbative dynamics of multifield inflation models. We have focused extensively on the role that the background initial conditions play in determining both the number of e-folds of inflation and the power spectrum of models, with and without interactions. Applying Bayesian principles to the analysis has allowed us to incorporate our beliefs in these models in terms of prior probabilities for model parameters and initial conditions, leaving us with probability distribution functions for inflation's observable or quasi-observable features.

7.1 How do we get enough inflation?

We have extensively studied two models, the first of which is the standard hybrid inflation model with two dynamical fields. Hybrid inflation was chosen primarily as a toy model for those early universe scenarios that might have a pre-inflationary period that is dominated by the same scalar dynamics that give inflation. Although this model generally does not predict the observed spectrum (since $n_s > 1$), it is possible to manipulate the inflationary portion of the potential to achieve a red spectrum [120, 121, 220]. Consequently, our results in Part III of this thesis should hold not only in general for toy multifield cases, but perhaps also in the particular case of our universe, if inflation is

indeed following a non-typical hybrid pattern.

In Part III we looked specifically at the way by which hybrid inflation can begin, given an ensemble of initial states. Naïvely, hybrid inflation requires a relatively special initial condition in order to begin inflating, with the heavy hybrid field satisfying $\langle\psi\rangle \approx 0$. Depending on the initial condition chosen, this may or may not be an attracting solution. Furthermore, hybrid inflation has chaotic dynamics, which significantly complicates any *prima facie* conclusions we might be able to draw based only on what we expect in limiting cases, such as slow-roll. Previous analyses of the initial conditions dependence of this model have reached a variety of conclusions on its stability.

In order to determine what the likely or expected outcome of the models are, we first need to define how we expect the initial state to be distributed. This addition to the model is necessary from the perspective of a Bayesian model builder: if we do not know the initial state for the universe, we must instead come up with an uninformed prior probability that incorporates this level of ignorance. If different priors result in the same behavior, we can make a strong statement on the model's robustness.

This was performed in Chapter 3, where we constrained our initial conditions to lie on equal energy slices of phase space, while neglecting inhomogeneity. This constraint allows us to do two things. First, we can identify points on the constraint surface with unique solutions to the Klein-Gordon equation, making it impossible for different initial conditions to be related to each other by time-translation along allowed solutions in phase space. This is a clearer description of what we mean by the universe's initial state than many previous studies that allow any possible field-space point to be the initial condition, since two of our initial conditions will never give degenerate end-

states.[1] Second, choosing our constraint surface according to constant-energy surfaces, which is a time-like parameter for expanding FLRW universes, gives a physical criterion to define our initial state. Without any input from high energy theory, we can then define priors for initial conditions on the equal energy surface that maximize information entropy and give us the least informed way by which we can study this system. Using a variety of priors, we found that hybrid inflation does indeed give many inflationary solutions, regardless of the initial energy surface that we choose our initial conditions to lie upon.[2]

Chapter 4 is a significant improvement on the basic results obtained for the homogeneous hybrid inflation analysis in Chapter 3. In this section we allowed for initial conditions that had sub-horizon gradients, using lattice PDE solvers to replicate our Monte Carlo exploration of hybrid inflation's chaotic parameter regime. The chaotic pre-inflationary dynamics were instrumental in the conclusions that we were able to draw: small changes in the phase, amplitude, or wavelength of the perturbations can also result in radically different end-states for the universe. The conventional wisdom is that adding inhomogeneity to a pre-inflationary phase will only hurt the ability of a model to inflate. This argument has made a strong comeback in studies that have critically examined the inflationary paradigm, such as Refs. [153, 156]. However, we are able to explicitly demonstrate that sub-horizon homogeneity before inflation is not a necessary requirement for multifield models to begin inflating. In fact, initial

[1] This also defines a type of Cauchy surface in field space, in analogy to techniques in classical general relativity theory [221].

[2] After the publication of Chapter 3, Ref. [177] found a prior probability that used constant energy slicings for initial conditions, but whose predictions are independent on the initial energy. While this is an improvement on the prior probability that we used, since we found no significant energy dependence in our results, we expect this prior to have similar results to our analysis.

inhomogeneity may help an otherwise hopeless initial state to achieve many e-folds of inflation. Since this was demonstrated only for those cases where we could neglect the backreaction of the field perturbations onto the metric, we would be very interested to see this analysis repeated with a full general relativity numerical code, such as those recently developed in Refs. [170, 171, 222].

It is important to note that we have assumed that the Lagrangian that is valid during the epochs when observationally relevant modes leave the horizon is also valid in a pre-inflationary epoch. This is a strong assumption that deserves some explanation, since we might expect the potential to have significantly different features away from the region that gives the last 50-60 e-folds of inflation. A particularly strong counterargument to our approach, as mentioned recently in Refs [154, 155] and others, is that there might exist non-global minima, in which a classical trajectory might become trapped, prior to yielding the inflationary action. This results in eternal inflation, which may be ended by quantum tunneling out of the metastable vacuum directly into a configuration that will inflate for $\mathcal{O}(100)$ e-folds, providing another dynamical resolution to the initial conditions problem. While we feel that this is a legitimate concern for the types of analysis presented in Part III, we take the viewpoint that our results show that adding additional structure like nearby minima to the pre-inflationary period is not strictly necessary to get a large fraction of a model's solutions to inflate. Instead, it can be achieved by a variety of mechanisms, each of which might be termed "natural" depending on whether a bottom-up or top-down philosophy of inflationary model building is being used.

7.2 How can we get generic predictions?

The second class of model we analyzed were large-field chaotic inflation models with many fields assisting each other during inflation. These models have a characteristic structure like $V \sim \sum_i \phi_i^p$ and are obvious generalizations of the simplest phenomenological single-field models, like the simple $m^2\phi^2$ potential. In Part IV we assumed that there was some mechanism by which inflationary solutions are generated, so that the concerns in Part III can be ameliorated. However, these models have predictions that still depend on the background solution. For instance, if a given mode ζ_k leaves the horizon when almost all of the fields are in their minima, then the power spectrum for this mode looks as if it came from a model with fewer actively evolving fields. In the limit that all of the heavier fields have vanishing contributions during periods of interest, the predictions for any of these models approaches that of single-field inflation. Consequently, the prior probability for the model's background initial condition could fundamentally change the predictions for these models.

This might seem troubling since we do not have access to this type of information in the vast majority of inflationary scenarios. This leads us to one of the central points of this thesis: theoretical uncertainties can be integrated out of a model, given a careful definition of the inflationary scenario. When we have no knowledge of the initial state, we simply require the prior probability for the initial condition to have maximum Shannon entropy, *i.e.*, the definition of the prior must contain the least amount of possible information.[3] We then

[3]Often the prior probability cannot be specified in such a way that there will remain no parametrization dependence, *i.e.*, the prior for a parametrization θ will not necessarily be the same as that for a related set of coordinates θ'. However, by studying the change in the model's predictions when the prior is altered we can qualitatively assess the robustness of the predictions to the choice of parametrization, as was done in Chapter 5.

integrate over all of these nuisance parameters to get a probability distribution for the model's generic predictions or its *prior predictive distribution.*

Common criticisms of this approach include:

The issue of subjectivity: *If one changes the prior, then the shape of the PDF for the observables would change. Since the definition of priors has a subjective component, the marginalized predictions are subjective, too.*

While this is true, we note that the sensitivity of a model to its priors can be largely studied by comparing different prior probabilities, as was done in Chapter 5.[4] If we interpret the prior probability as incorporating our knowledge or beliefs about the likely value of a given parameter, then this criticism amounts to: if we knew more about the model, we would know more about its predictions. In instances where no prior knowledge is applicable, this subjectivity vanishes, since using anything besides the maximum entropy prior implies some *a priori* hypothesis by definition. This is almost certainly the case for dynamical parameters in the model, such as initial conditions, so our results should be largely robust.

The issue of frequentism: *The universe's actual parameters might correspond to a* 5σ *or greater deviation from the mean in the prior predictive distribution for an observable. The model might very well be true, but the bulk of the prior predictive distribution does not capture the model's real prediction.*

We can only place a probability on our belief in a model's parameters that is a deterministic function of the available data and our prior, which will hopefully converge to the neighborhood around a value if we are given updated, consistent datasets. In the limit that we had a clear and convincing

[4] We quickly note that if we associated each possible prior to one scientist, marginalizing over priors would give a distribution for what a population of people would expect out of the model.

reason to prefer one configuration over others, our distribution would have a strong peak near the prediction for this preferred configuration, recovering the implicit expectations of a frequentist.

To simply study a model by finding the connection between the "actual" parameter of the model and the corresponding prediction is not sufficient. For most models, particularly phenomenological ones, this level of prior knowledge is hugely impractical or even impossible. In contrast, the Bayesian methodology that we have used incorporates all possible initial states with weightings defined by the information available to us as model builders and returns a correspondingly generic prediction.

7.3 What do generic predictions look like?

In Part IV we saw that the predictivity of our models can improve when we increase the number of degrees of freedom by adding more dynamical fields. In Chapter 5 we studied the pivot scale values for the power spectrum and its derivatives, explicitly comparing different priors for initial conditions in the N_f-quadratic model, using a wide variety of different forms including what we used for hybrid inflation in Chapter 3. We found very little difference in the functional form for the predictions and only trivial reweightings of the probability distributions between different priors. We interpret these results as indicating that these types of large-field model are not sensitively dependent on their initial conditions.

In Chapter 6 we extended this further by analytically incorporating priors on both initial conditions and Lagrangian parameters into a generic prediction for a large class of observationally relevant inflation models. We found that sum-separable, large-field models have sharp generic predictions as a conse-

quence of the central limit theorem. We calculated this explicitly for the ratio of the tensor spectral index to the tensor-to-scalar ratio n_t/r, since any deviation from the single-field gravitational wave consistency relation indicates genuinely multifield contributions to the prediction. We find that both n_t and r follow Gaussian distributions that are correlated, but easily characterized if we assume that any background initial condition 55 e-folds before the end of inflation is equally likely. This provides more evidence that multifield models may become increasingly predictive as the number of fields increases.

While we have not yet carried out a similar analysis for small-field models or for multifield models with strong interactions between the fields, we feel strongly that the simple principles we have discovered here will remain. Multifield models are "predictive," as measured by the typical variance in the spread of the predicted observables; they are generally insensitive to the definition of the initial conditions prior; and this emergent behavior arises because of the models' large dimensionality. While these should be defining features of multifield models, small-field models in particular might have some greater dependence on the initial conditions than large-field inflation, since the inflationary region usually only corresponds to a local attractor, with a qualitatively smaller basin of attraction than a large-field model. Furthermore, the analytic calculations that were performed in Chapter 6 explicitly do not apply for these models, since we would need to incorporate the contribution to ζ in the δN formalism from the end-of-inflation surface. Consequently, more work must be done before we can study these types of models in as much detail as presented here, which should be a fruitful avenue for further research.

7.4 Outlook

With the release of the latest results from *Planck*, the next major milestones in the collection of CMB data will be in measuring the polarization spectra. While exciting results may certainly be obtained here, we might reasonably be pessimistic about the possibility of observing signatures that will guide us toward specific inflationary models in the near future. This point was driven home with the controversy surrounding the interpretation of dust and B-modes in the BICEP2 data, and may perhaps be a theme for next generation cosmology. In the event that the key observables for inflation — n_s, r, and $f_{\rm NL}$ — remain bounded in the general region of parameter space that they are currently in, we may not soon have a data-driven reason to radically alter our approach to inflation.

For an inflationary theorist this raises a few concerns. If one scalar field is sufficient to explain all of the available data, then the motivation for multifield models will remain no more concrete than what is mentioned in this thesis: multiple fields are *possible*; they *generalize* the simplest cases; and they are often *naturally* predicted from high energy theory. However, they are not *necessary*. Consequently, their study would continue to focus on reconciling general principles from high energy theory that favor large dimensionality with observations that are completely consistent with simpler models.

This thesis makes progress toward these types of "post-modern" goals. Since our theoretical uncertainty will remain approximately constant in the absence of experimental pressure, the methods used here should become more relevant for studies that attempt to propagate fundamental unknowns about a model into a corresponding uncertainty in the prediction. However, since the analysis of multifield models is more complicated than single-field models, this is not

the methodology that is often chosen. Instead, people are usually content with understanding the complicated relationship that exists between the primordial spectra and a model's masses and couplings, which is indeed a hard problem. However, we would contend that this type of analysis is incomplete. In order to assess a model's observational status one must also carefully consider the role of *a priori* information on the structure of both static and dynamical parameters, such as masses and initial conditions, respectively. Even with a complete lack of information one can still define sensible prior probabilities and map these to predictions through the Bayesian technique of marginalization. This allows us to calculate the complete predictions of a model and perhaps begin to understand how an effectively single-field universe can be reconciled with high energy theory.

Appendix A

Bayesian Methods

Throughout this thesis we make frequent use of Bayesian statistical techniques. While methods such as Markov Chain Monte Carlo (MCMC) are commonplace in cosmological data analysis and data-based inference, they are rarely used in theoretical modelling. In this appendix we will outline what techniques we have used and how they apply to theoretical inflation models and the initial conditions dependence of multifield inflation.

A.1 Bayes theorem

For random variables A and B, Bayes theorem relates conditional probabilities in the following fashion:

$$P(A\,|\,B) = \frac{P(A)P(B\,|\,A)}{P(B)}, \tag{A.1}$$

where $P(A)$ is the *prior probability distribution* for variable A, $P(A\,|\,B)$ is the *posterior probability distribution* for variable A given B, $P(B\,|\,A)$ is the *likelihood* of getting B given A, and $P(B)$ is the *Bayesian evidence* or *marginalized likelihood* for B. The prior probability encodes the *a priori* knowledge that one has about variable A and allows you to invert the conditional probability $P(A\,|\,B) \to P(B\,|\,A)$ up to the value of the evidence. The Bayesian evidence is a normalization factor that is unimportant for our studies here, although it arises when comparing models' ability to explain data.

A.2 Application to theoretical modeling

In our work we have used the Bayesian technique of marginalization. This is the process of integrating out nuisance parameters from a model, with the parameters weighted by their prior probability. This obtains a simplified probability distribution function (PDF) that is independent of the nuisance parameters but incorporates our uncertainty in those parameters that have been marginalized.

If we wish to find the marginalized PDF for parameter A conditioned on the value of parameter B, then we integrate out all extraneous parameters in the model θ_i by

$$P(A\,|\,B) = \int d\theta_i P(A\,|\,\theta_i, B) P(\theta_i\,|\,B). \tag{A.2}$$

If the PDF for the nuisance parameters is independent of B, then $P(\theta_i\,|\,B) \to P(\theta_i)$, which is that nuisance parameter's prior probability.

For a multifield inflation model we have observables $\mathcal{O}$ that we wish to calculate, such as the tensor-to-scalar ratio r or the spectral index n_s that are valid near the pivot scale $k_{\rm piv}$. We also may have pseudo-observables, such as the total number of e-folds N_e between the initial and final state for a given solution of the model, which we treat as if they were actually observable, but are in fact only partially inferable from the data in the context of the chosen model.

Any of these observables depend on a series of parameters in the Lagrangian, such as couplings g_j and masses m_i, as well as dynamical parameters, like a particular realization's initial conditions. In this thesis we will at various times treat these parameters as both important and nuisance parameters, sometimes marginalizing over them and sometimes not. For instance, in Chapter 5 we compare a set of PDFs for observables $P_\mu(\mathcal{O})$ that depend on different

prior probabilities for the background solution's initial conditions $P_\mu(\mathrm{IC})$, with the fields' masses $\vec{m} \equiv \{m_i\}$ fixed.

This can be expressed as

$$P_\mu(\mathcal{O}\,|\,\vec{m}) = \int d(\mathrm{IC}) P(\mathcal{O}|\mathrm{IC},\vec{m}) P_\mu(\mathrm{IC},\vec{m}). \tag{A.3}$$

We can perform integrals like Eq. (A.3) numerically by generating a sample of initial conditions IC_j from the prior probability $P_\mu(\mathrm{IC},\vec{m})$ and using

$$P(\mathcal{O}\,|\,\vec{m}) \approx \frac{1}{N_{\mathrm{samp}}} \sum_j P(\mathcal{O}\,|\,\mathrm{IC}_j,\vec{m}) \tag{A.4}$$

for $\mathrm{IC}_j \sim P_\mu(\mathrm{IC},\vec{m})$, where N_{samp} is the number of elements in the sample. If $P(\mathcal{O}\,|\,\mathrm{IC}_j,\vec{m})$ is probabilistic, then we simply evaluate it for every initial condition in the sample.

However, for inflation models we can uniquely determine a value for an observable like n_s given all of the parameters in the first-order equations of motion, so that $P(\mathcal{O}\,|\,\mathrm{IC}_j,\vec{m})$ is a deterministic relationship with

$$P(\mathcal{O}'\,|\,\mathrm{IC}_j,\vec{m}) = \begin{cases} 1 & \text{if} \quad \mathcal{O}(\mathrm{IC}_j,\vec{m}) = \mathcal{O}' \\ 0 & \text{otherwise} \end{cases}. \tag{A.5}$$

In this case, we estimate $P(\mathcal{O}\,|\,m)$ from a histogram of the population statistics. In other words, we draw a sample of parameters from the prior probability and for every element in that sample we calculate the observable via the methods presented in Chapter 2. We then bin the sample of observables we get from this process and estimate the actual PDF from the sample histogram or kernel density estimation.

Bibliography

[1] A. A. Starobinsky, *A New Type of Isotropic Cosmological Models Without Singularity*, *Phys.Lett.* **B91** (1980) 99–102.

[2] A. H. Guth, *The Inflationary Universe: A Possible Solution to the Horizon and Flatness Problems*, *Phys.Rev.* **D23** (1981) 347–356.

[3] A. D. Linde, *A New Inflationary Universe Scenario: A Possible Solution of the Horizon, Flatness, Homogeneity, Isotropy and Primordial Monopole Problems*, *Phys.Lett.* **B108** (1982) 389–393.

[4] A. Albrecht and P. J. Steinhardt, *Cosmology for Grand Unified Theories with Radiatively Induced Symmetry Breaking*, *Phys.Rev.Lett.* **48** (1982) 1220–1223.

[5] **WMAP** Collaboration, G. Hinshaw et al., *Nine-Year Wilkinson Microwave Anisotropy Probe (WMAP) Observations: Cosmological Parameter Results*, *Astrophys.J.Suppl.* **208** (2013) 19, [arXiv:1212.5226].

[6] T. Vachaspati and M. Trodden, *Causality and cosmic inflation*, *Phys.Rev.* **D61** (1999) 023502, [gr-qc/9811037].

[7] M. Trodden and T. Vachaspati, *What is the homogeneity of our universe telling us?*, *Mod.Phys.Lett.* **A14** (1999) 1661–1666, [gr-qc/9905091].

[8] J. Stewart, *Perturbations of Friedmann-Robertson-Walker cosmological models*, *Class.Quant.Grav.* **7** (1990) 1169–1180.

[9] S. M. Carroll, *Spacetime and geometry. An introduction to general relativity*, vol. 1. Addison-Wesley, 2004.

[10] D. H. Lyth and A. R. Liddle, *The primordial density perturbation: Cosmology, inflation and the origin of structure*. Cambridge University Press, 2009.

[11] D. Wands, K. A. Malik, D. H. Lyth, and A. R. Liddle, *A new approach to the evolution of cosmological perturbations on large scales*, *Phys.Rev.* **D62** (2000) 043527, [astro-ph/0003278].

[12] S. Weinberg, *Adiabatic modes in cosmology*, *Phys.Rev.* **D67** (2003) 123504, [astro-ph/0302326].

[13] C. Kiefer and D. Polarski, *Why do cosmological perturbations look classical to us?*, *Adv.Sci.Lett.* **2** (2009) 164–173, [arXiv:0810.0087].

[14] E. J. Copeland, E. W. Kolb, A. R. Liddle, and J. E. Lidsey, *Observing the inflaton potential*, *Phys.Rev.Lett.* **71** (1993) 219–222, [hep-ph/9304228].

[15] A. R. Liddle and D. H. Lyth, *The Cold dark matter density perturbation*, *Phys. Rept.* **231** (1993) 1–105, [astro-ph/9303019].

[16] L. C. Price, J. Frazer, J. Xu, H. V. Peiris, and R. Easther, *MultiModeCode: An efficient numerical solver for multifield inflation*, *JCAP* **1503** (2015), no. 03 005, [arXiv:1410.0685].

[17] **Planck** Collaboration, P. Ade et al., *Planck 2013 results. I. Overview of products and scientific results*, *Astron.Astrophys.* **571** (2014) A1, [arXiv:1303.5062].

[18] **Planck** Collaboration, P. Ade et al., *Planck 2013 results. XVI. Cosmological parameters*, *Astron.Astrophys.* **571** (2014) A16, [arXiv:1303.5076].

[19] **Planck** Collaboration, P. Ade et al., *Planck 2013 results. XXII. Constraints on inflation*, *Astron.Astrophys.* **571** (2014) A22, [arXiv:1303.5082].

[20] D. Baumann and L. McAllister, *Inflation and String Theory*, arXiv:1404.2601.

[21] R. Easther and K.-i. Maeda, *Chaotic dynamics and two field inflation*, *Class.Quant.Grav.* **16** (1999) 1637–1652, [gr-qc/9711035].

[22] S. Clesse, C. Ringeval, and J. Rocher, *Fractal initial conditions and natural parameter values in hybrid inflation*, *Phys.Rev.* **D80** (2009) 123534, [arXiv:0909.0402].

[23] J. A. Adams, B. Cresswell, and R. Easther, *Inflationary perturbations from a potential with a step*, *Phys.Rev.* **D64** (2001) 123514, [astro-ph/0102236].

[24] **WMAP** Collaboration, H. Peiris et al., *First year Wilkinson Microwave Anisotropy Probe (WMAP) observations: Implications for inflation*, *Astrophys.J.Suppl.* **148** (2003) 213, [astro-ph/0302225].

[25] J. Martin and C. Ringeval, *Inflation after WMAP3: Confronting the Slow-Roll and Exact Power Spectra to CMB Data*, *JCAP* **0608** (2006) 009, [astro-ph/0605367].

[26] L. M. Hall and H. V. Peiris, *Cosmological Constraints on Dissipative Models of Inflation*, *JCAP* **0801** (2008) 027, [arXiv:0709.2912].

[27] R. Bean, X. Chen, H. Peiris, and J. Xu, *Comparing Infrared Dirac-Born-Infeld Brane Inflation to Observations*, *Phys.Rev.* **D77** (2008) 023527, [arXiv:0710.1812].

[28] L. Lorenz, J. Martin, and C. Ringeval, *Brane inflation and the WMAP data: A Bayesian analysis*, *JCAP* **0804** (2008) 001, [arXiv:0709.3758].

[29] J. Martin and C. Ringeval, *First CMB Constraints on the Inflationary Reheating Temperature*, *Phys.Rev.* **D82** (2010) 023511, [arXiv:1004.5525].

[30] J. Martin, C. Ringeval, and R. Trotta, *Hunting Down the Best Model of Inflation with Bayesian Evidence*, *Phys.Rev.* **D83** (2011) 063524, [arXiv:1009.4157].

[31] J. Martin, C. Ringeval, R. Trotta, and V. Vennin, *The Best Inflationary Models After Planck*, *JCAP* **1403** (2014) 039, [arXiv:1312.3529].

[32] M. J. Mortonson, H. V. Peiris, and R. Easther, *Bayesian Analysis of Inflation: Parameter Estimation for Single Field Models*, *Phys.Rev.* **D83** (2011) 043505, [arXiv:1007.4205].

[33] R. Easther and H. V. Peiris, *Bayesian Analysis of Inflation II: Model Selection and Constraints on Reheating*, *Phys.Rev.* **D85** (2012) 103533, [arXiv:1112.0326].

[34] J. Norena, C. Wagner, L. Verde, H. V. Peiris, and R. Easther, *Bayesian Analysis of Inflation III: Slow Roll Reconstruction Using Model Selection*, *Phys.Rev.* **D86** (2012) 023505, [arXiv:1202.0304].

[35] A. Lewis, A. Challinor, and A. Lasenby, *Efficient computation of CMB anisotropies in closed FRW models*, *Astrophys.J.* **538** (2000) 473–476, [astro-ph/9911177].

[36] A. Lewis and S. Bridle, *Cosmological parameters from CMB and other data: A Monte Carlo approach*, *Phys.Rev.* **D66** (2002) 103511, [astro-ph/0205436].

[37] F. Feroz, M. Hobson, and M. Bridges, *MultiNest: an efficient and robust Bayesian inference tool for cosmology and particle physics*, *MNRAS* **398** (2009) 1601–1614.

[38] I. Huston and K. A. Malik, *Numerical calculation of second order perturbations*, *JCAP* **0909** (2009) 019, [arXiv:0907.2917].

[39] I. Huston and A. J. Christopherson, *Calculating Non-adiabatic Pressure Perturbations during Multi-field Inflation*, *Phys.Rev.* **D85** (2012) 063507, [arXiv:1111.6919].

[40] I. Huston and K. A. Malik, *Second Order Perturbations During Inflation Beyond Slow-roll*, *JCAP* **1110** (2011) 029, [arXiv:1103.0912].

[41] I. Huston and A. J. Christopherson, *Isocurvature Perturbations and Reheating in Multi-Field Inflation*, arXiv:1302.4298.

[42] J. Frazer, *Predictions in multifield models of inflation*, *Journal of Cosmology and Astroparticle Physics* **2014** (2013), no. 01 028, [arXiv:1303.3611].

[43] J. A. Adams, G. G. Ross, and S. Sarkar, *Multiple inflation*, *Nucl.Phys.* **B503** (1997) 405–425, [hep-ph/9704286].

[44] P. Adshead, C. Dvorkin, W. Hu, and E. A. Lim, *Non-Gaussianity from Step Features in the Inflationary Potential*, *Phys.Rev.* **D85** (2012) 023531, [arXiv:1110.3050].

[45] R. Easther, J. Frazer, H. V. Peiris, and L. C. Price, *Simple predictions from multifield inflationary models*, *Phys.Rev.Lett.* **112** (2014) 161302, [arXiv:1312.4035].

[46] D. Seery, D. J. Mulryne, J. Frazer, and R. H. Ribeiro, *Inflationary perturbation theory is geometrical optics in phase space*, *JCAP* **1209** (2012) 010, [arXiv:1203.2635].

[47] D. H. Lyth and A. Riotto, *Particle physics models of inflation and the cosmological density perturbation*, *Phys.Rept.* **314** (1999) 1–146, [hep-ph/9807278].

[48] D. Langlois and S. Renaux-Petel, *Perturbations in generalized multi-field inflation*, *JCAP* **0804** (2008) 017, [arXiv:0801.1085].

[49] D. Salopek, J. Bond, and J. M. Bardeen, *Designing Density Fluctuation Spectra in Inflation*, *Phys.Rev.* **D40** (1989) 1753.

[50] B. A. Bassett, S. Tsujikawa, and D. Wands, *Inflation dynamics and reheating*, *Rev.Mod.Phys.* **78** (2006) 537–589, [astro-ph/0507632].

[51] D. J. Mulryne, D. Seery, and D. Wesley, *Moment transport equations for non-Gaussianity*, *JCAP* **1001** (2010) 024, [arXiv:0909.2256].

[52] D. J. Mulryne, D. Seery, and D. Wesley, *Moment transport equations for the primordial curvature perturbation*, *JCAP* **1104** (2011) 030, [arXiv:1008.3159].

[53] D. J. Mulryne, *Transporting non-Gaussianity from sub to super-horizon scales*, *JCAP* **1309** (2013) 010, [arXiv:1302.3842].

[54] T. Bunch and P. Davies, *Quantum Field Theory in de Sitter Space: Renormalization by Point Splitting*, *Proc.Roy.Soc.Lond.* **A360** (1978) 117–134.

[55] J. M. Bardeen, *Gauge Invariant Cosmological Perturbations*, *Phys.Rev.* **D22** (1980) 1882–1905.

[56] J. M. Bardeen, P. J. Steinhardt, and M. S. Turner, *Spontaneous creation of almost scale-free density perturbations in an inflationary universe*, *Phys. Rev. D* **28** (Aug, 1983) 679–693.

[57] S. Groot Nibbelink and B. van Tent, *Density perturbations arising from multiple field slow roll inflation*, hep-ph/0011325.

[58] C. Gordon, D. Wands, B. A. Bassett, and R. Maartens, *Adiabatic and entropy perturbations from inflation*, *Phys.Rev.* **D63** (2001) 023506, [astro-ph/0009131].

[59] S. Groot Nibbelink and B. van Tent, *Scalar perturbations during multiple field slow-roll inflation*, *Class.Quant.Grav.* **19** (2002) 613–640, [hep-ph/0107272].

[60] C. T. Byrnes and D. Wands, *Curvature and isocurvature perturbations from two-field inflation in a slow-roll expansion*, *Phys.Rev.* **D74** (2006) 043529, [astro-ph/0605679].

[61] N. Bartolo, S. Matarrese, and A. Riotto, *Adiabatic and isocurvature perturbations from inflation: Power spectra and consistency relations*, *Phys.Rev.* **D64** (2001) 123504, [astro-ph/0107502].

[62] D. Wands, N. Bartolo, S. Matarrese, and A. Riotto, *An Observational test of two-field inflation*, *Phys.Rev.* **D66** (2002) 043520, [astro-ph/0205253].

[63] J. García-Bellido and D. Wands, *Metric perturbations in two field inflation*, *Phys.Rev.* **D53** (1996) 5437–5445, [astro-ph/9511029].

[64] K. A. Malik, D. Wands, and C. Ungarelli, *Large scale curvature and entropy perturbations for multiple interacting fluids*, *Phys.Rev.* **D67** (2003) 063516, [astro-ph/0211602].

[65] K. A. Malik, *Cosmological perturbations in an inflationary universe*, astro-ph/0101563.

[66] K. A. Malik and D. Wands, *Adiabatic and entropy perturbations with interacting fluids and fields*, *JCAP* **0502** (2005) 007, [astro-ph/0411703].

[67] A. A. Starobinsky, *Multicomponent de Sitter (Inflationary) Stages and the Generation of Perturbations*, *JETP Lett.* **42** (1985) 152–155.

[68] D. Lyth, *Large Scale Energy Density Perturbations and Inflation*, *Phys.Rev.* **D31** (1985) 1792–1798.

[69] M. Sasaki and E. D. Stewart, *A General analytic formula for the spectral index of the density perturbations produced during inflation*, *Prog.Theor.Phys.* **95** (1996) 71–78, [astro-ph/9507001].

[70] D. Salopek and J. Bond, *Nonlinear evolution of long wavelength metric fluctuations in inflationary models*, *Phys.Rev.* **D42** (1990) 3936–3962.

[71] M. Sasaki and T. Tanaka, *Superhorizon scale dynamics of multiscalar inflation*, *Prog.Theor.Phys.* **99** (1998) 763–782, [gr-qc/9801017].

[72] D. H. Lyth and Y. Rodriguez, *The Inflationary prediction for primordial non-Gaussianity*, *Phys.Rev.Lett.* **95** (2005) 121302, [astro-ph/0504045].

[73] F. Vernizzi and D. Wands, *Non-gaussianities in two-field inflation*, *JCAP* **0605** (2006) 019, [astro-ph/0603799].

[74] T. Battefeld and R. Easther, *Non-Gaussianities in Multi-field Inflation*, *JCAP* **0703** (2007) 020, [astro-ph/0610296].

[75] K. A. Malik and D. Wands, *Cosmological perturbations*, *Phys.Rept.* **475** (2009) 1–51, [arXiv:0809.4944].

[76] M. Dias, J. Frazer, and A. R. Liddle, *Multifield consequences for D-brane inflation*, *JCAP* **1206** (2012) 020, [arXiv:1203.3792].

[77] D. Seery and J. E. Lidsey, *Primordial non-Gaussianities from multiple-field inflation*, *JCAP* **0509** (2005) 011, [astro-ph/0506056].

[78] J. M. Maldacena, *Non-Gaussian features of primordial fluctuations in single field inflationary models*, *JHEP* **0305** (2003) 013, [astro-ph/0210603].

[79] L. Alabidi and D. H. Lyth, *Inflation models and observation*, *JCAP* **0605** (2006) 016, [astro-ph/0510441].

[80] C. T. Byrnes, M. Sasaki, and D. Wands, *The primordial trispectrum from inflation*, *Phys.Rev.* **D74** (2006) 123519, [astro-ph/0611075].

[81] A. D. Linde, *Hybrid inflation*, *Phys.Rev.* **D49** (1994) 748–754, [astro-ph/9307002].

[82] E. J. Copeland, A. R. Liddle, D. H. Lyth, E. D. Stewart, and D. Wands, *False vacuum inflation with Einstein gravity*, *Phys.Rev.* **D49** (1994) 6410–6433, [astro-ph/9401011].

[83] Z. Lalak, D. Langlois, S. Pokorski, and K. Turzynski, *Curvature and isocurvature perturbations in two-field inflation*, *JCAP* **0707** (2007) 014, [arXiv:0704.0212].

[84] A. Avgoustidis, S. Cremonini, A.-C. Davis, R. H. Ribeiro, K. Turzynski, et al., *The Importance of Slow-roll Corrections During Multi-field Inflation*, *JCAP* **1202** (2012) 038, [arXiv:1110.4081].

[85] A. R. Liddle, A. Mazumdar, and F. E. Schunck, *Assisted inflation*, *Phys.Rev.* **D58** (1998) 061301, [astro-ph/9804177].

[86] P. Kanti and K. A. Olive, *On the realization of assisted inflation*, *Phys.Rev.* **D60** (1999) 043502, [hep-ph/9903524].

[87] P. Kanti and K. A. Olive, *Assisted chaotic inflation in higher dimensional theories*, *Phys.Lett.* **B464** (1999) 192–198, [hep-ph/9906331].

[88] N. Kaloper and A. R. Liddle, *Dynamics and perturbations in assisted chaotic inflation*, *Phys.Rev.* **D61** (2000) 123513, [hep-ph/9910499].

[89] R. Easther and L. McAllister, *Random matrices and the spectrum of N-flation*, *JCAP* **0605** (2006) 018, [hep-th/0512102].

[90] S. Dimopoulos, S. Kachru, J. McGreevy, and J. G. Wacker, *N-flation*, *JCAP* **0808** (2008) 003, [hep-th/0507205].

[91] S. A. Kim and A. R. Liddle, *Nflation: multi-field inflationary dynamics and perturbations*, *Phys.Rev.* **D74** (2006) 023513, [astro-ph/0605604].

[92] S. A. Kim and A. R. Liddle, *Nflation: Non-Gaussianity in the horizon-crossing approximation*, *Phys.Rev.* **D74** (2006) 063522, [astro-ph/0608186].

[93] S. A. Kim and A. R. Liddle, *Nflation: observable predictions from the random matrix mass spectrum*, *Phys.Rev.* **D76** (2007) 063515, [arXiv:0707.1982].

[94] D. Wenren, *Tilt and Tensor-to-Scalar Ratio in Multifield Monodromy Inflation*, arXiv:1405.1411.

[95] X. Chen, R. Easther, and E. A. Lim, *Large Non-Gaussianities in Single Field Inflation*, *JCAP* **0706** (2007) 023, [astro-ph/0611645].

[96] X. Chen, R. Easther, and E. A. Lim, *Generation and Characterization of Large Non-Gaussianities in Single Field Inflation*, *JCAP* **0804** (2008) 010, [arXiv:0801.3295].

[97] R. Easther and R. Flauger, *Planck Constraints on Monodromy Inflation*, *JCAP* **1402** (2014) 037, [arXiv:1308.3736].

[98] P. D. Meerburg, D. N. Spergel, and B. D. Wandelt, *Searching for Oscillations in the Primordial Power Spectrum: Perturbative Approach (Paper I)*, *Phys.Rev.* **D89** (2014) 063536, [arXiv:1308.3704].

[99] P. D. Meerburg and D. N. Spergel, *Searching for Oscillations in the Primordial Power Spectrum: Constraints from Planck (Paper II)*, *Phys.Rev.* **D89** (2014) 063537, [arXiv:1308.3705].

[100] E. J. Copeland, A. Mazumdar, and N. Nunes, *Generalized assisted inflation*, *Phys.Rev.* **D60** (1999) 083506, [astro-ph/9904309].

[101] D. Battefeld and S. Kawai, *Preheating after N-flation*, *Phys.Rev.* **D77** (2008) 123507, [arXiv:0803.0321].

[102] T. C. Bachlechner, M. Dias, J. Frazer, and L. McAllister, *Chaotic inflation with kinetic alignment of axion fields*, *Phys.Rev.* **D91** (2015), no. 2 023520, [arXiv:1404.7496].

[103] C. Ringeval, P. Brax, C. van de Bruck, and A.-C. Davis, *Boundary inflation and the wmap data*, *Phys.Rev.* **D73** (2006) 064035, [astro-ph/0509727].

[104] M. Dias, J. Frazer, and D. Seery, *Computing observables in curved multifield models of inflation - A guide (with code) to the transport method*, arXiv:1502.03125.

[105] R. Easther and L. C. Price, *Initial conditions and sampling for multifield inflation*, *JCAP* **1307** (2013) 027, [arXiv:1304.4244].

[106] A. D. Linde, *Chaotic Inflation*, *Phys.Lett.* **B129** (1983) 177–181.

[107] R. O. Ramos, *Fine tuning solution for hybrid inflation in dissipative chaotic dynamics*, *Phys.Rev.* **D64** (2001) 123510, [astro-ph/0104379].

[108] G. Lazarides, C. Panagiotakopoulos, and N. Vlachos, *Initial conditions for smooth hybrid inflation*, *Phys.Rev.* **D54** (1996) 1369–1373, [hep-ph/9606297].

[109] G. Lazarides and N. Vlachos, *Initial conditions for supersymmetric inflation*, *Phys.Rev.* **D56** (1997) 4562–4567, [hep-ph/9707296].

[110] N. Tetradis, *Fine tuning of the initial conditions for hybrid inflation*, *Phys.Rev.* **D57** (1998) 5997–6002, [astro-ph/9707214].

[111] L. E. Mendes and A. R. Liddle, *Initial conditions for hybrid inflation*, *Phys.Rev.* **D62** (2000) 103511, [astro-ph/0006020].

[112] S. Clesse and J. Rocher, *Avoiding the blue spectrum and the fine-tuning of initial conditions in hybrid inflation*, *Phys.Rev.* **D79** (2009) 103507, [arXiv:0809.4355].

[113] N. Agarwal, R. Bean, L. McAllister, and G. Xu, *Universality in D-brane inflation*, *Journal of Cosmology and Astroparticle Physics* **2011** (2011), no. 09 002, [arXiv:1103.2775].

[114] G. Gibbons, S. W. Hawking, and J. Stewart, *A natural measure on the set of all universes*, *Nuclear Physics B* **281** (1987), no. 3 736–751.

[115] S. Hawking and D. N. Page, *How probable is inflation?*, *Nucl.Phys.* **B298** (1988) 789–809.

[116] G. Gibbons and N. Turok, *The Measure Problem in Cosmology*, *Phys.Rev.* **D77** (2008) 063516, [hep-th/0609095].

[117] B. Freivogel, *Making predictions in the multiverse*, *Class.Quant.Grav.* **28** (2011) 204007, [arXiv:1105.0244].

[118] J. S. Schiffrin and R. M. Wald, *Measure and Probability in Cosmology*, *Phys.Rev.* **D86** (2012) 023521, [arXiv:1202.1818].

[119] L. Kofman and A. D. Linde, *Generation of Density Perturbations in the Inflationary Cosmology*, *Nucl.Phys.* **B282** (1987) 555.

[120] S. Clesse, *Hybrid inflation along waterfall trajectories*, *Phys.Rev.* **D83** (2011) 063518, [arXiv:1006.4522].

[121] H. Kodama, K. Kohri, and K. Nakayama, *On the waterfall behavior in hybrid inflation*, *Prog.Theor.Phys.* **126** (2011) 331–350, [arXiv:1102.5612].

[122] K. Story, C. Reichardt, Z. Hou, R. Keisler, K. Aird, et al., *A Measurement of the Cosmic Microwave Background Damping Tail from the 2500-square-degree SPT-SZ survey*, *Astrophys.J.* **779** (2013) 86, [arXiv:1210.7231].

[123] **WMAP** Collaboration, G. Hinshaw et al., *Nine-Year Wilkinson Microwave Anisotropy Probe (WMAP) Observations: Cosmological Parameter Results*, *Astrophys.J.Suppl.* **208** (2013) 19, [arXiv:1212.5226].

[124] **WMAP** Collaboration, C. Bennett et al., *Nine-Year Wilkinson Microwave Anisotropy Probe (WMAP) Observations: Final Maps and Results*, *Astrophys.J.Suppl.* **208** (2013) 20, [arXiv:1212.5225].

[125] **Atacama Cosmology Telescope** Collaboration, J. L. Sievers et al., *The Atacama Cosmology Telescope: Cosmological parameters from three seasons of data*, *JCAP* **1310** (2013) 060, [arXiv:1301.0824].

[126] J. Martin and V. Vennin, *Stochastic Effects in Hybrid Inflation*, *Phys.Rev.* **D85** (2012) 043525, [arXiv:1110.2070].

[127] G. N. Felder, L. Kofman, and A. D. Linde, *Inflation and preheating in NO models*, *Phys.Rev.* **D60** (1999) 103505, [hep-ph/9903350].

[128] A. C. Hindmarsh, P. N. Brown, K. E. Grant, S. L. Lee, R. Serban, D. E. Shumaker, and C. S. Woodward, *Sundials: Suite of nonlinear and differential/algebraic equation solvers*, *ACM Trans. Math. Softw.* **31** (Sept., 2005) 363396.

[129] F. Finelli, G. Marozzi, A. Starobinsky, G. Vacca, and G. Venturi, *Stochastic growth of quantum fluctuations during slow-roll inflation*, *Phys.Rev.* **D82** (2010) 064020, [arXiv:1003.1327].

[130] F. Finelli, G. Marozzi, A. Starobinsky, G. Vacca, and G. Venturi, *Generation of fluctuations during inflation: Comparison of stochastic and field-theoretic approaches*, *Phys.Rev.* **D79** (2009) 044007, [arXiv:0808.1786].

[131] J. Theiler, *Estimating fractal dimension*, *J. Opt. Soc. Am. A* **7** (1990) 1055–1073.

[132] S. Downes, B. Dutta, and K. Sinha, *Attractors, Universality and Inflation*, *Phys.Rev.* **D86** (2012) 103509, [arXiv:1203.6892].

[133] A. Aazami and R. Easther, *Cosmology from random multifield potentials*, *JCAP* **0603** (2006) 013, [hep-th/0512050].

[134] S.-H. H. Tye, J. Xu, and Y. Zhang, *Multi-field Inflation with a Random Potential*, *JCAP* **0904** (2009) 018, [arXiv:0812.1944].

[135] J. Frazer and A. R. Liddle, *Multi-field inflation with random potentials: field dimension, feature scale and non-Gaussianity*, *JCAP* **1202** (2012) 039, [arXiv:1111.6646].

[136] D. Marsh, L. McAllister, and T. Wrase, *The Wasteland of Random Supergravities*, *JHEP* **1203** (2012) 102, [arXiv:1112.3034].

[137] D. Battefeld, T. Battefeld, and S. Schulz, *On the Unlikeliness of Multi-Field Inflation: Bounded Random Potentials and our Vacuum*, *JCAP* **1206** (2012) 034, [arXiv:1203.3941].

[138] L. McAllister, S. Renaux-Petel, and G. Xu, *A Statistical Approach to Multifield Inflation: Many-field Perturbations Beyond Slow Roll*, *JCAP* **1210** (2012) 046, [arXiv:1207.0317].

[139] N. Itzhaki and E. D. Kovetz, *Inflection Point Inflation and Time Dependent Potentials in String Theory*, *JHEP* **0710** (2007) 054, [arXiv:0708.2798].

[140] R. Allahverdi, B. Dutta, and A. Mazumdar, *Attraction towards an inflection point inflation*, *Phys.Rev.* **D78** (2008) 063507, [arXiv:0806.4557].

[141] N. Itzhaki and E. D. Kovetz, *A Phase Transition between Small and Large Field Models of Inflation*, *Class.Quant.Grav.* **26** (2009) 135007, [arXiv:0810.4299].

[142] M. Spalinski, *Initial conditions for small field inflation*, *Phys.Rev.* **D80** (2009) 063529, [arXiv:0903.4999].

[143] D. S. Goldwirth and T. Piran, *Inhomogeneity and the onset of inflation*, *Phys.Rev.Lett.* **64** (1990) 2852–2855.

[144] D. S. Goldwirth, *On inhomogeneous initial conditions for inflation*, *Phys.Rev.* **D43** (1991) 3204–3213.

[145] D. S. Goldwirth and T. Piran, *Initial conditions for inflation*, *Phys.Rept.* **214** (1992) 223–291.

[146] R. Easther, L. C. Price, and J. Rasero, *Inflating an Inhomogeneous Universe*, *JCAP* **1408** (2014) 041, [arXiv:1406.2869].

[147] **2dFGRS** Collaboration, S. Cole et al., *The 2dF Galaxy Redshift Survey: Power-spectrum analysis of the final dataset and cosmological*

implications, *Mon.Not.Roy.Astron.Soc.* **362** (2005) 505–534, [astro-ph/0501174].

[148] **SDSS** Collaboration, D. J. Eisenstein et al., *SDSS-III: Massive Spectroscopic Surveys of the Distant Universe, the Milky Way Galaxy, and Extra-Solar Planetary Systems*, *Astron.J.* **142** (2011) 72, [arXiv:1101.1529].

[149] T. Giannantonio, A. J. Ross, W. J. Percival, R. Crittenden, D. Bacher, et al., *Improved Primordial Non-Gaussianity Constraints from Measurements of Galaxy Clustering and the Integrated Sachs-Wolfe Effect*, *Phys.Rev.* **D89** (2014) 023511, [arXiv:1303.1349].

[150] B. Leistedt, H. V. Peiris, and N. Roth, *Constraints on Primordial Non-Gaussianity from Eight Hundred Thousand Photometric Quasars*, *Phys.Rev.Lett.* **113** (2014), no. 22 221301, [arXiv:1405.4315].

[151] Z. Hou, C. Reichardt, K. Story, B. Follin, R. Keisler, et al., *Constraints on Cosmology from the Cosmic Microwave Background Power Spectrum of the 2500 deg^2 SPT-SZ Survey*, *Astrophys.J.* **782** (2014), no. 2 74, [arXiv:1212.6267].

[152] **Planck** Collaboration, P. Ade et al., *Planck 2013 results. XXII. Constraints on inflation*, *Astron.Astrophys.* **571** (2014) A22, [arXiv:1303.5082].

[153] A. Ijjas, P. J. Steinhardt, and A. Loeb, *Inflationary paradigm in trouble after Planck2013*, *Phys.Lett.* **B723** (2013) 261–266, [arXiv:1304.2785].

[154] A. H. Guth, D. I. Kaiser, and Y. Nomura, *Inflationary paradigm after Planck 2013*, *Phys.Lett.* **B733** (2014) 112–119, [arXiv:1312.7619].

[155] A. Linde, *Inflationary Cosmology after Planck 2013*, in *100e Ecole d'Ete de Physique: Post-Planck Cosmology Les Houches, France, July 8-August 2, 2013*, 2014. arXiv:1402.0526.

[156] A. Ijjas, P. J. Steinhardt, and A. Loeb, *Inflationary schism after Planck2013*, *Phys.Lett.* **B736** (2014) 142–146, [arXiv:1402.6980].

[157] S. R. Coleman and E. J. Weinberg, *Radiative Corrections as the Origin of Spontaneous Symmetry Breaking*, *Phys.Rev.* **D7** (1973) 1888–1910.

[158] A. Albrecht, R. H. Brandenberger, and R. Matzner, *Numerical Analysis of Inflation*, *Phys.Rev.* **D32** (1985) 1280.

[159] J. Kung and R. H. Brandenberger, *The Initial Condition Dependence of Inflationary Universe Models*, *Phys.Rev.* **D40** (1989) 2532.

[160] R. H. Brandenberger and J. Kung, *Chaotic Inflation as an Attractor in Initial Condition Space*, *Phys.Rev.* **D42** (1990) 1008–1015.

[161] H. A. Feldman and R. H. Brandenberger, *Chaotic Inflation With Metric and Matter Perturbations*, *Phys.Lett.* **B227** (1989) 359.

[162] M. Grana, *Flux compactifications in string theory: A Comprehensive review*, *Phys.Rept.* **423** (2006) 91–158, [hep-th/0509003].

[163] M. R. Douglas and S. Kachru, *Flux compactification*, *Rev.Mod.Phys.* **79** (2007) 733–796, [hep-th/0610102].

[164] F. Denef, M. R. Douglas, and S. Kachru, *Physics of String Flux Compactifications*, *Ann.Rev.Nucl.Part.Sci.* **57** (2007) 119–144, [hep-th/0701050].

[165] F. Denef, *Les Houches Lectures on Constructing String Vacua*, arXiv:0803.1194.

[166] G. N. Felder and I. Tkachev, *LATTICEEASY: A Program for lattice simulations of scalar fields in an expanding universe*, *Comput.Phys.Commun.* **178** (2008) 929–932, [hep-ph/0011159].

[167] A. V. Frolov, *DEFROST: A New Code for Simulating Preheating after Inflation*, *JCAP* **0811** (2008) 009, [arXiv:0809.4904].

[168] R. Easther, H. Finkel, and N. Roth, *PSpectRe: A Pseudo-Spectral Code for (P)reheating*, *JCAP* **1010** (2010) 025, [arXiv:1005.1921].

[169] H. Kurki-Suonio, P. Laguna, and R. A. Matzner, *Inhomogeneous inflation: Numerical evolution*, *Phys.Rev.* **D48** (1993) 3611–3624, [astro-ph/9306009].

[170] C. L. Wainwright, M. C. Johnson, H. V. Peiris, A. Aguirre, L. Lehner, et al., *Simulating the universe(s): from cosmic bubble collisions to cosmological observables with numerical relativity*, *JCAP* **1403** (2014) 030, [arXiv:1312.1357].

[171] C. L. Wainwright, M. C. Johnson, A. Aguirre, and H. V. Peiris, *Simulating the universe(s) II: phenomenology of cosmic bubble collisions in full General Relativity*, *JCAP* **1410** (2014), no. 10 024, [arXiv:1407.2950].

[172] G. Dvali, Q. Shafi, and R. K. Schaefer, *Large scale structure and supersymmetric inflation without fine tuning*, *Phys.Rev.Lett.* **73** (1994) 1886–1889, [hep-ph/9406319].

[173] W. Buchmüller, V. Domcke, K. Kamada, and K. Schmitz, *Hybrid Inflation in the Complex Plane*, *JCAP* **1407** (2014) 054, [arXiv:1404.1832].

[174] S. Clesse, B. Garbrecht, and Y. Zhu, *Non-Gaussianities and Curvature Perturbations from Hybrid Inflation*, *Phys.Rev.* **D89** (2014) 063519, [arXiv:1304.7042].

[175] S. R. Green and R. M. Wald, *A new framework for analyzing the effects of small scale inhomogeneities in cosmology*, *Phys.Rev.* **D83** (2011) 084020, [arXiv:1011.4920].

[176] A. Corichi and A. Karami, *On the measure problem in slow roll inflation and loop quantum cosmology*, *Phys.Rev.* **D83** (2011) 104006, [arXiv:1011.4249].

[177] A. Corichi and D. Sloan, *Inflationary Attractors and their Measures*, *Class.Quant.Grav.* **31** (2014) 062001, [arXiv:1310.6399].

[178] A. Berera and C. Gordon, *Inflationary initial conditions consistent with causality*, *Phys.Rev.* **D63** (2001) 063505, [hep-ph/0010280].

[179] A. D. Linde, *Creation of a compact topologically nontrivial inflationary universe*, *JCAP* **0410** (2004) 004, [hep-th/0408164].

[180] **Planck** Collaboration, P. Ade et al., *Planck 2013 Results. XXIV. Constraints on primordial non-Gaussianity*, *Astron.Astrophys.* **571** (2014) A24, [arXiv:1303.5084].

[181] D. I. Kaiser and E. I. Sfakianakis, *Multifield Inflation after Planck: The Case for Nonminimal Couplings*, *Phys.Rev.Lett.* **112** (2014) 011302, [arXiv:1304.0363].

[182] R. Kallosh and A. Linde, *Universality Class in Conformal Inflation*, *JCAP* **1307** (2013) 002, [arXiv:1306.5220].

[183] R. Kallosh and A. Linde, *Non-minimal Inflationary Attractors*, *JCAP* **1310** (2013) 033, [arXiv:1307.7938].

[184] R. Kallosh and A. Linde, *Multi-field Conformal Cosmological Attractors*, *JCAP* **1312** (2013) 006, [arXiv:1309.2015].

[185] D. Polarski and A. A. Starobinsky, *Spectra of perturbations produced by double inflation with an intermediate matter dominated stage*, *Nucl.Phys.* **B385** (1992) 623–650.

[186] J. Ellis, M. Fairbairn, and M. Sueiro, *Rescuing Quadratic Inflation*, *JCAP* **1402** (2014) 044, [arXiv:1312.1353].

[187] D. W. Scott, *On optimal and data-based histograms*, *Biometrika* **66** (1979), no. 3 605–610.

[188] C. M. Peterson and M. Tegmark, *Testing Two-Field Inflation*, *Phys.Rev.* **D83** (2011) 023522, [arXiv:1005.4056].

[189] G. E. Crooks, *Measuring thermodynamic length*, *Phys. Rev. Lett.* **99** (Sep, 2007) 100602.

[190] M. K. Transtrum, B. B. Machta, and J. P. Sethna, *Why are nonlinear fits so challenging?*, *Phys.Rev.Lett.* **104** (2010) 060201, [arXiv:0909.3884].

[191] B. B. Machta, R. Chachra, M. K. Transtrum, and J. P. Sethna, *Parameter space compression underlies emergent theories and predictive models*, *Science* **342** (2013), no. 6158 604–607.

[192] P. Adshead and R. Easther, *Constraining Inflation*, *JCAP* **0810** (2008) 047, [arXiv:0802.3898].

[193] J. Elliston, D. J. Mulryne, D. Seery, and R. Tavakol, *Evolution of fNL to the adiabatic limit*, *JCAP* **1111** (2011) 005, [arXiv:1106.2153].

[194] J. Frazer and A. R. Liddle, *Exploring a string-like landscape*, *JCAP* **1102** (2011) 026, [arXiv:1101.1619].

[195] G. Leung, E. R. Tarrant, C. T. Byrnes, and E. J. Copeland, *Reheating, Multifield Inflation and the Fate of the Primordial Observables*, *JCAP* **1209** (2012) 008, [arXiv:1206.5196].

[196] G. Leung, E. R. Tarrant, C. T. Byrnes, and E. J. Copeland, *Influence of Reheating on the Trispectrum and its Scale Dependence*, *JCAP* **1308** (2013) 006, [arXiv:1303.4678].

[197] J. Meyers and E. R. M. Tarrant, *Perturbative Reheating After Multiple-Field Inflation: The Impact on Primordial Observables*, *Phys.Rev.* **D89** (2014), no. 6 063535, [arXiv:1311.3972].

[198] L. C. Price, H. V. Peiris, J. Frazer, and R. Easther, *Gravitational wave consistency relations for multifield inflation*, *Phys.Rev.Lett.* **114** (2015), no. 3 031301, [arXiv:1409.2498].

[199] **BICEP2** Collaboration, P. Ade et al., *Detection of B-Mode Polarization at Degree Angular Scales by BICEP2*, *Phys.Rev.Lett.* **112** (2014), no. 24 241101, [arXiv:1403.3985].

[200] L. Verde, H. Peiris, and R. Jimenez, *Optimizing CMB polarization experiments to constrain inflationary physics*, *JCAP* **0601** (2006) 019, [astro-ph/0506036].

[201] S. Dodelson, *How much can we learn about the physics of inflation?*, *Phys.Rev.Lett.* **112** (2014) 191301, [arXiv:1403.6310].

[202] J. Caligiuri and A. Kosowsky, *Inflationary Tensor Perturbations After BICEP*, *Phys.Rev.Lett.* **112** (2014) 191302, [arXiv:1403.5324].

[203] **CMBPol Study Team** Collaboration, D. Baumann et al., *CMBPol Mission Concept Study: Probing Inflation with CMB Polarization*, *AIP Conf.Proc.* **1141** (2009) 10–120, [arXiv:0811.3919].

[204] **PRISM Collaboration** Collaboration, P. Andre et al., *PRISM (Polarized Radiation Imaging and Spectroscopy Mission): A White Paper on the Ultimate Polarimetric Spectro-Imaging of the Microwave and Far-Infrared Sky*, arXiv:1306.2259.

[205] R. W. Ogburn et al., *BICEP2 and Keck array operational overview and status of observations*, in *Society of Photo-Optical Instrumentation Engineers (SPIE) Conference Series*, vol. 8452, Sept., 2012. arXiv:1208.0638.

[206] Z. Ahmed et al., *Bicep3: a 95 ghz refracting telescope for degree-scale cmb polarization*, *Proc. SPIE* **9153** (2014) 91531N–91531N–12.

[207] T. Matsumura et al., *Polarbear-2 optical and polarimeter designs*, *Proc. SPIE* **8452** (2012) 84523E–84523E–8.

[208] **SPT-3G** Collaboration, B. Benson et al., *SPT-3G: A Next-Generation Cosmic Microwave Background Polarization Experiment on the South Pole Telescope*, *Proc.SPIE Int.Soc.Opt.Eng.* **9153** (2014) 91531P, [arXiv:1407.2973].

[209] P. Oxley, P. Ade, C. Baccigalupi, P. deBernardis, H.-M. Cho, et al., *The EBEX experiment*, *Proc.SPIE Int.Soc.Opt.Eng.* **5543** (2004) 320–331, [astro-ph/0501111].

[210] B. Crill, P. Ade, E. Battistelli, S. Benton, R. Bihary, et al., *SPIDER: A Balloon-borne Large-scale CMB Polarimeter*, *Proc.SPIE Int.Soc.Opt.Eng.* **7010** (2008) 2P, [arXiv:0807.1548].

[211] K. W. Masui and U.-L. Pen, *Primordial gravity wave fossils and their use in testing inflation*, *Phys.Rev.Lett.* **105** (2010) 161302, [arXiv:1006.4181].

[212] L. Book, M. Kamionkowski, and F. Schmidt, *Lensing of 21-cm Fluctuations by Primordial Gravitational Waves*, *Phys.Rev.Lett.* **108** (2012) 211301, [arXiv:1112.0567].

[213] T. L. Smith, H. V. Peiris, and A. Cooray, *Deciphering inflation with gravitational waves: cosmic microwave background polarization vs. direct detection with laser interferometers*, *Phys.Rev.* **D73** (2006) 123503, [astro-ph/0602137].

[214] D. V. Hinkley, *On the ratio of two correlated normal random variables*, *Biometrika* **56** (1969), no. 3 635–639.

[215] J. Martin, C. Ringeval, and R. Trotta, *Hunting down the best model of inflation with Bayesian evidence*, *Phys.Rev.* **D83** (Mar., 2011) [arXiv:1009.4157].

[216] H. Jeffreys, *An invariant form for the prior probability in estimation problems*, in *Proceedings of the Royal Society of London A: Mathematical, Physical and Engineering Sciences*, vol. 186, pp. 453–461, The Royal Society, 1946.

[217] R. Easther and J. T. Giblin, *The Hubble slow roll expansion for multi field inflation*, *Phys.Rev.* **D72** (2005) 103505, [astro-ph/0505033].

[218] Y.-S. Piao, *On perturbation spectra of N-flation*, *Phys.Rev.* **D74** (2006) 047302, [gr-qc/0606034].

[219] D. Sloan, *Minimal Coupling and Attractors*, *Class.Quant.Grav.* **31** (2014) 245015, [arXiv:1407.3977].

[220] M. P. Hertzberg and F. Wilczek, *Inflation Driven by Unification Energy*, arXiv:1407.6010.

[221] P. Townsend, *Black holes: Lecture notes*, gr-qc/9707012.

[222] K. Clough, P. Figueras, H. Finkel, M. Kunesch, E. A. Lim, et al., *GRChombo : Numerical Relativity with Adaptive Mesh Refinement*, arXiv:1503.03436.